

**UCLA**

**UCLA Electronic Theses and Dissertations**

**Title**

Biomimetic synthesis of noble metal nanocrystals

**Permalink**

<https://escholarship.org/uc/item/6wd2v39r>

**Author**

Chiu, Chin-Yi

**Publication Date**

2013

Peer reviewed|Thesis/dissertation

UNIVERSITY OF CALIFORNIA

Los Angeles

Biomimetic Synthesis of Noble Metal Nanocrystals

A dissertation submitted in partial satisfaction of the  
requirements for the degree Doctor of Philosophy  
in Materials Science and Engineering

by

Chin-Yi Chiu

2013

© Copyright by

Chin-Yi Chiu

2013

# ABSTRACT OF THE DISSERTATION

## Biomimetic Synthesis of Noble Metal Nanocrystals

by

Chin-Yi Chiu

Doctor of Philosophy in Materials Science and Engineering

University of California, Los Angeles, 2013

Professor Yu Huang, Chair

At the nanometer scale, the physical and chemical properties of materials heavily depend on their sizes and shapes. This fact has triggered considerable efforts in developing controllable nanomaterial synthesis. The controlled growth of colloidal nanocrystal is a kinetic process, in which high-energy facets grow faster and then vanish, leading to a nanocrystal enclosed by low-energy facets. Identifying a surfactant that can selectively bind to a particular crystal facet and thus lower its surface energy, is critical and challenging in shape controlled synthesis of nanocrystals. Biomolecules exhibiting exquisite molecular recognition properties can be exploited to precisely engineer nanostructured materials. In the first part of my thesis, we employed the phage display technique to select a specific multifunctional peptide sequence

which can bind on Pd surface and mediate Pd crystal nucleation and growth, achieving size controlled synthesis of Pd nanocrystals in aqueous solution. We further demonstrated a rational biomimetic approach to the predictable synthesis of nanocrystals enclosed by a particular facet in the case of Pt. Specifically, Pt {100} and Pt {111} facet-specific peptides were identified and used to synthesize Pt nanocubes and Pt nano-tetrahedrons, respectively. The mechanistic studies of Pt {111} facet-specific peptide had led us to study the facet-selective adsorption of aromatic molecules on noble metal surfaces. The discoveries had achieved the development of design strategies to select facet-selective molecules which can synthesize nanocrystals with expected shapes in both Pt and Pd system. At last, we exploited Pt facet-specific peptides and controlled the molecular interaction to produce one- and three- dimensional nanostructures composed of anisotropic nanoparticles in synthetic conditions without supramolecular pre-organization, demonstrating the full potential of biomolecules in mediating material formation process. My research on biomimetic synthesis of nanocrystals with shape control and nanostructures with control over the anisotropy are unprecedented, representing a step forward in achieving the goal of producing complex nanostructures with required properties. The fundamental studies on the biomolecule-inorganic interfaces have contributed to advancing the synthesis tool of colloidal nanomaterials and enriching understating of organic-inorganic interface, impacting many applications.

The dissertation of Chin-Yi Chiu is approved.

Bruce S. Dunn

Yang Yang

Yunfeng Lu

Yu Huang, Committee Chair

University of California, Los Angeles

2013

## Table of Contents

ACKNOWLEDGEMENTS.....	vii
BIOGRAPHY.....	viii
INTRODUCTION.....	1
Chapter I: PEPTIDE SELECTION PROCESS AND SYNTEHSIS .....	5
Chapter II: SIZE-CONTROLLED SYNTHESIS OF PALLADIUM NANOCRYSTALS USING A MULTIFUNCTIONAL PEPTIDE.....	7
A. Peptide selection and results.....	7
B. Pd nanocrystal synthesis with selected peptides.....	8
C. Results and discussion.....	9
Chapter III: SHAPE-CONTROLLED SYNTHESIS OF PLATINUM NANOCRYSTALS USING FACET-SPECIFIC PEPTIDES.....	17
A. Facet-specific peptide selection and results.....	17
B. Shape control synthesis of Pt nanocrystals with selected peptides.....	19
C. Results and discussion.....	20
Facet-selectivity of T7 and S7 peptide.....	20
Shape evolution of nanocube and nano-tetrahedron.....	23
Peptide-directed shape transformation.....	30
Chapter IV: FACET-SELECTIVE ADSORPTION ON NOBLE METAL CRYSTALS GUIDED BY ELECTROSTATIC POTENTIAL SURFACES OF AROMATIC MOLECULES...33	
A. Experimental methods.....	34
Nanocrystals synthesis by aromatic molecules and characterization.....	34
Computation of molecular electrostatic potential surfaces and DFT calculation.....	35
B. Results and discussion.....	37
Platinum nanocrystals controlled by aromatic molecules.....	37
Binding mechanism of aromatic molecules on metal surfaces.....	49

Derived design strategies and shape control of palladium nanocrystals.....	58
Chapter V: PEPTIDE DIRECTED SYNTHESIS AND ASSEMBLY OF ANISOTROPIC NANOCRYSTALS INTO ONE- AND THREE- DIMENSIONAL NANOSTRUCTURES.....	66
A. Experimental methods.....	67
B. Results and discussion.....	68
S7 peptide induced aggregation of Pt nanoparticles.....	68
Oriented attachment of nanocubes and nano-tetrahedrons.....	74
One- and three- dimensional assembly of anisotropic nanoparticles.....	81
CONCLUSION.....	87
REFERENCES.....	88



## Acknowledgements

First of all, my doctoral committee Professor Bruce Dunn, Professor Yang Yang and Professor Yunfeng Lu gave me valuable advices in my dissertation. I sincerely appreciate for their help. My advisor, Professor Yu Huang, spent lots of time and effort helping me not only about research but also about my professional skills. I am very grateful that she can share her opinions and give me suggestions over many aspects of my graduate studying such as completing a project, doing a poster and presentation and writing a paper. All of these have contributed to the accomplishment of my Ph.D. degree at UCLA. In addition, my groups including a collaborated group in Chemistry, advised by Professor Xiangfeng Duan, are very important for my graduate studying. We shared experimental experiences, exchanged opinions on literatures and collaborated with each other. These help me quickly accumulate knowledge and experience in various fields, which absolutely complete me as a Doctor of Philosophy.

Additionally, I appreciate the collaboration with Professor Christopher Murray in University of Pennsylvania, LC-MS support from Professor Yi Tang, Raman support from Professor Bruce Dunn and theoretical calculation support from Professor Vidvuds Ozolins. Through discussion with them, I can obtain the professional suggestions from their viewpoints which inspire my thinking and bring me more ideas for carrying out my research projects.

## Biography

Chin-Yi Chiu received her B.S. and M.S. degree in materials science and engineering from National Taiwan University, Taipei, Taiwan in 2005 and 2007, respectively. She was a full-time teaching assistance in 2007 at National Taiwan University. She joined Dr. Yu Huang's group in 2008 and conducted the research of biomimetic synthesis of noble metal nanocrystals. She received her Ph.D. degree in Materials Science and Engineering, University of California, Los Angeles in 2013. She was awarded UCLA Dissertation Year Fellowship and UCLA Outstanding Doctor of Philosophy, Materials Science & Engineering in 2012 and 2013, respectively. She has five first-author and nine co-author papers published in peer-review journals. She gave oral presentations in academic conferences, 2007ICMAT-ica- in Singapore, Spring 2011 ACS National Meeting in Anaheim and Spring 2013 ACS National Meeting in New Orleans. Her research interests include biomimetic synthesis of inorganic nanomaterials and organic-inorganic interface.

## INTRODUCTION

Nanocrystals (NCs) defined as crystals with at least one dimension ranging from 1 to 100 nm exhibit different properties from their bulk counterparts, which has received enormous attention.<sup>1-4</sup> In recent years, significant efforts have been made to engineer nanomaterials to exploit their novel properties for optical, electronic, magnetic, catalytic, biomedical and structural application.<sup>5-8</sup> In principle, manipulation of the electron confinement by a NC is an effective means to control its properties. As the physical size of the material is decreased below a specific length scale (usually on the nanometer dimension) which is defined by the spatial confinement of its electrons, its properties become highly sensitive to its size and shape.<sup>2,4</sup> The typical example is the emission wavelength of photoluminescent semiconductor quantum dot such as CdS can be tuned by their radius.<sup>3,9</sup> Moreover, one-dimensional nanostructures such as wire and rod, and faceted, concaved and multi-pods NCs have been successfully produced to achieve a variety of fascinating properties, such as the observation of band gap red-shift with the length of InAs rods.<sup>1,5,8,10-12</sup>

For noble metals such as gold (Au), silver (Ag), platinum (Pt) and palladium (Pd), it is even more evident that their properties heavily depend on the physical parameters such as size, shape, structure and composition.<sup>1,4,8,10,11</sup> By controlling one of these parameters, the properties of noble metal NCs can be finely tailored. For example, it is found the shape of Au or Ag nanocrystal plays an important role in the number, position and intensity of the localized surface plasmon resonance (LSPR) modes, and the polarization dependence for molecular probing by surface-enhanced Raman scattering (SERS).<sup>13</sup> In catalysis, the size reduction resulting in the increase of the surface to volume ration has been known a powerful means to increase the activity of catalytic materials such as Pt and Pd.<sup>1,8,14</sup> Recently, manipulation of the catalytic

selectivity has been a centered topic in advanced catalysis, in which control of the exposed facet of a NC (i.e., the atom arrangement on metal surface) is believed to be important.<sup>14-16</sup> For example, Pt nanocubes enclosed by (100) facets can selectively catalyze cyclohexane production in benzene hydrogenation.<sup>16</sup> Therefore, it is of importance to seek appropriate approaches to produce nanomaterials with precise control over their composition, size and shape, which is always a critical topic in the field of nanoscale science and technology. Although efforts to date have accomplished controllable nanomaterials synthesis,<sup>1,8,17-19</sup> producing nanomaterials with programmable structures, integrated properties and required functions remains challenging for chemists.

Conventional top-down have enabled the fabrication of a variety of nanostructures. For example, two-dimensional nanostructure such as quantum wells can be prepared by molecular beam epitaxy (MBE).<sup>20</sup> One dimensional nanostructure such as nanowires and nanotubes can be produced by advanced nano-techniques such as electron-beam (e-beam) lithographic and focused-ion-beam (FIB) writing.<sup>20</sup> However, the development has been limited by the difficulties in producing diverse nanostructures in terms of size, morphology and chemical composition with these methods. Chemical synthesis (solution based), a bottom-up fabrication, provides an alternative strategy to synthesize various nanostructures with high quality, large quantity and low cost.<sup>1,8,19</sup> In principle, the shape of a crystal is determined by the enclosed facets which give a minimum total surface energy. For colloidal NCs in solution, the crystal growth is believed to be a kinetically controlled process, in which low-energy facets persist while high-energy facets vanish, leading to a particular resultant shape. This is manipulated by the introduction of capping agent (surfactant) to tune the energy of crystallographic facets, controlling their growth rate.<sup>21</sup> Therefore, identifying a surfactant that can specifically bind to a particular crystal facet, lowering

its surface energy, is critical to the shape control synthesis of NCs. A number of compounds have been evaluated as effective surfactant to modify the surface energy and synthesize NCs with well-defined shapes. For example, trioctylphosphine oxide (TOPO) has been suggested to effectively decrease the relative growth rate of (101) facet of cobalt, playing a key role in yielding cobalt nanorods.<sup>22</sup> The combination of TOPO and hexylphosphonic acid (HPA) can exert an anisotropic shape control over CdSe.<sup>23</sup> However, shaping NCs is often achieved by means of a trial-and-error process for selecting appropriate surfactant due to the lack of general approaches to identify facet-specific surfactant and fundamental studies on the associated organic-inorganic interfaces.

Biomolecules such as proteins and polypeptide exhibiting exquisite molecular recognition properties have been utilized in biological systems to produce nanomaterials with control over many aspects from orientation, size and morphology to assembly into complex structures specialized for biological functions.<sup>24-28</sup> They are the result of evolutionary refinement over millions of years. Significantly, most of the synthesis in nature happens in ambient conditions, resulting in a sharp contrast to the common chemical synthesis involved in high temperature and pressure. Moreover, the nanoscale sized features that nature can produce routinely have not been achieved artificially. Thus, by mimicking the nature's ability in producing materials (called biomimetic), it is believed the utilization of biomolecules guided from the natural methods can exert a greater control over nanomorphology and open up a promising avenue to programmable synthesis of nanostructures. Many nanomaterials such as SiO<sub>2</sub>, Fe<sub>3</sub>O<sub>4</sub> and Ag have been created *in vitro* (mostly in benign conditions) as those found in nature.<sup>29-32</sup> However, the obtained nanostructures are relatively simple and limited due to a lack of comprehensive understanding of the mediated biomolecules as well as the crystal formation

mechanism. The development of screening of peptide libraries (biopanning) offering the largest diversity of sequences for identification has overcome many difficulties in the use of biomineral-isolated peptides or proteins.<sup>33</sup> With the readily accessible biomolecules, it is more possible to fully exploit the potential of biomolecules in achieving well-controlled nanostructures synthesis and further investigate the interfaces between biomolecule and inorganic materials

In my PhD thesis, I mainly focus on the identification of material-surface specific peptide sequences using combinatorial phage display technique and the utilization of the selected peptides in mediating the synthesis of noble metal NCs. Specifically, the synthesis of Pd NCs in aqueous solution with controllable size in the sub-10 nm regime is mediated by a multifunctional peptide selected by biopanning. Starting with faceted substrates as targeting materials in peptide selection process, Pt (100) and (111) facet-selective peptides have been identified and exploited to synthesize Pt NCs with shape control. Moreover, the mechanistic studies of Pt (111) facet-selective peptides had motivated my study on the facet-selective adsorption of aromatic molecules on noble metal surfaces. We successfully developed design strategies to select facet-selective molecules and demonstrated their ability in shaping NCs with expected morphologies, indicating a step forward in achieving predictable and programmable nanostructure modulation through better understanding of organic-inorganic interfaces. In the last part of my thesis, the production of one- and three- dimensional nanostructures directed by Pt facet-specific peptides through particle attachment have been demonstrated, indicating the exploit of the full potential of biomolecules to construct complex and organized nanostructures in synthetic conditions.

## Chapter I: PEPTIDE SELECTION PROCESS AND SYNTEHSIS

Peptides libraries are displayed on the surface of biological systems such as bacteriophage (phage display, PD). The display techniques are constructed through engineering the host organism's genome, in which inserted gene code for amino acid sequence of peptides displayed on it. The peptides libraries provide a diverse pool of around  $10^{10}$  random peptides sequences for selecting peptide that shows binding affinity to specific inorganic materials (the selection process is called biopanning).<sup>33-35</sup> Here we describe the biopanning process briefly using phage display peptide libraries (Figure 1.1). At first, a target material is incubated with phage solution and gentle rocking for one hour, in which phage with peptides showing affinity to the materials surface will bind on it. The phage solution includes  $2 \times 10^{11}$  library phages diluted in 1 ml of 0.1 % Tris-Buffered Saline Tween-20 (TBST). The unbound phage will then be removed through washing with 0.1 % TBST for the first round and 0.3 % and 0.5% for the following rounds. The bound phage will be eluted from the materials surface using 0.2 M Glycine-HCl (pH 2.2), which will be subsequently neutralized with 1M Tris-HCl (pH 9.1). The eluted phage were amplified through infecting *Escherichia coli* in 25 ml of lysogeny broth (LB) and allowed to grow for 4.5 hours on an incubating shaker. The amplified phage will be used as the secondary selection pool for starting a new biopanning cycle. After 3-4 cycles, the sequence of the peptides displayed on phage showing relatively strong binding affinity to the target will be obtained through DNA sequencing. The phage elute at the last round of biopanning was plated on LB XGal/IPTG plates. 10 blue plaques were then picked from the plate and DNA sequenced. According to the sequence, these peptides can be synthesized chemically and used in the NCs synthesis. Peptide sequences showing binding affinity to different materials such as noble metals (Au, Ag, Pt and Pd) and semiconductors (Si, GaAs and ZnO) have been identified and shown in

literatures.<sup>33-35</sup> In my thesis, I conducted biopanning against Pd wire and Pt faceted substrates to select Pd materials-selective and Pt facet-selective peptides, respectively. The results of biopanning will be shown in the following chapters.

Fmoc solid-state peptide synthesis (SSPS) with N-terminal acylation and C-terminal amidation with a CS336X synthesizer (C S Bio) was used to synthesize peptides. The synthesized peptides were characterized by liquid chromatography mass spectrometer (LC-MS), Shimadzu 2010 EV. They were then purified by Beckman-Coulter Gold high-performance liquid chromatography (HPLC). The obtained peptides used in NCs syntheses usually have > 95% purity.

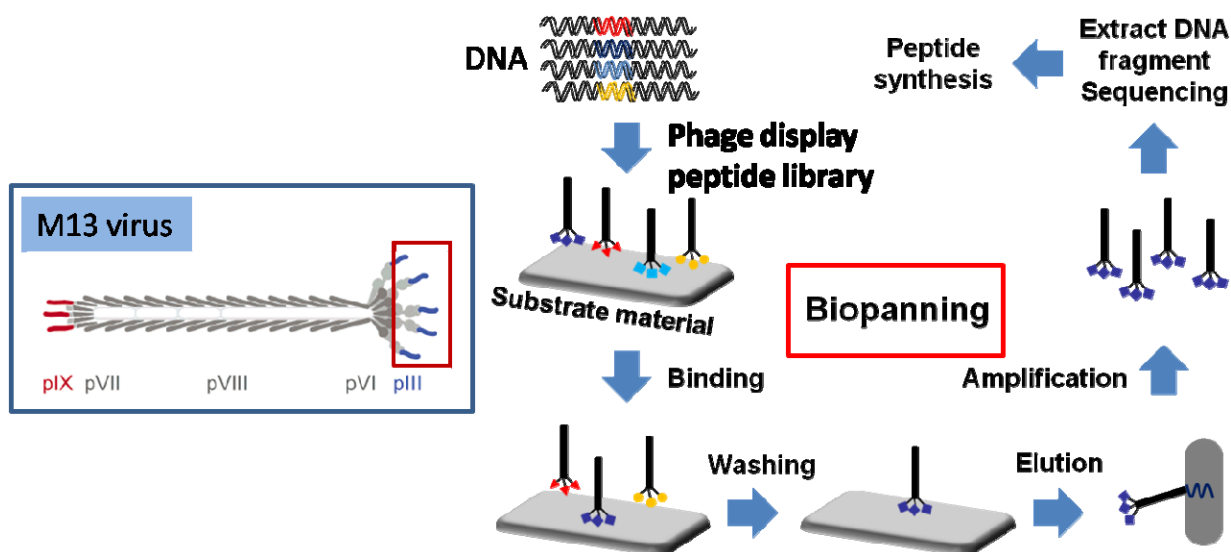


**Figure 1.1** Peptide selection process, biopanning.



## **Chapter II SIZE-CONTROLLED SYNTHESIS OF PALLADIUM NANOCRYSTALS USING A MULTIFUNCTIONAL PEPTIDE**

Pd is important in various applications such as hydrogen storage and catalyzing organic reactions such as Suzuki, Heck and Stille coupling.<sup>36</sup> The catalytic activity of Pd NCs is determined by their size ranging from 1 to 10 nm.<sup>37</sup> Conventional polyol synthesis methods have achieved the production of Pd NCs with a variety of sizes by using different stabilizers and reducing agents.<sup>1,8</sup> However, it is needed to develop an alternative synthesis method using a mild chemical reaction and water-based system, providing an environmental-friendly and safe approach to synthesizing Pd NCs with size control. There are some reports on Pd NCs synthesis in the sub-10 nm regime in aqueous solution but with limited size range and distribution.<sup>38-39</sup> Biomimetic synthesis provides a promising avenue to mediating the Pd crystal growth in solution by using peptides to display specific binding affinity to Pd metal surface. Here, we demonstrated the synthesis of Pd NCs with a size ranging from 2.2 to 6.6 nm through precise control over the crystal nucleation and growth stages by a peptide performing both stabilizing and reducing effect on Pd.<sup>40</sup>

### **A. Peptide selection results**

Peptide selection process was conducted against Pd wire with 1 cm in length and 0.5 mm in diameter (brand new for each round of biopanning) (99% pure, Sigma Aldrich). The wire was sterilized in 99% ethanol for fifteen minutes with gentle rocking followed by washing with sterilized water and TBS buffer solution for biopanning. The biopannings were carried out using Ph.D -7mer peptide library (New England Biolabs). After three round of biopanning, the peptide sequence Gln-Gln-Ser-Trp-Pro-Ile-Ser (QQSWPIS, termed as Q7, MW 885.98) was identified as Pd binding peptide since it appeared most frequently (four times among ten colonies). Q7 was then synthesized, purified and characterized (Figure 2.1). Another peptide sequence Ser-Leu-

Lys-Leu-Ala-Tyr-Pro (SLKLAYP, MW 832.02) appearing once was used as a nonspecific control.

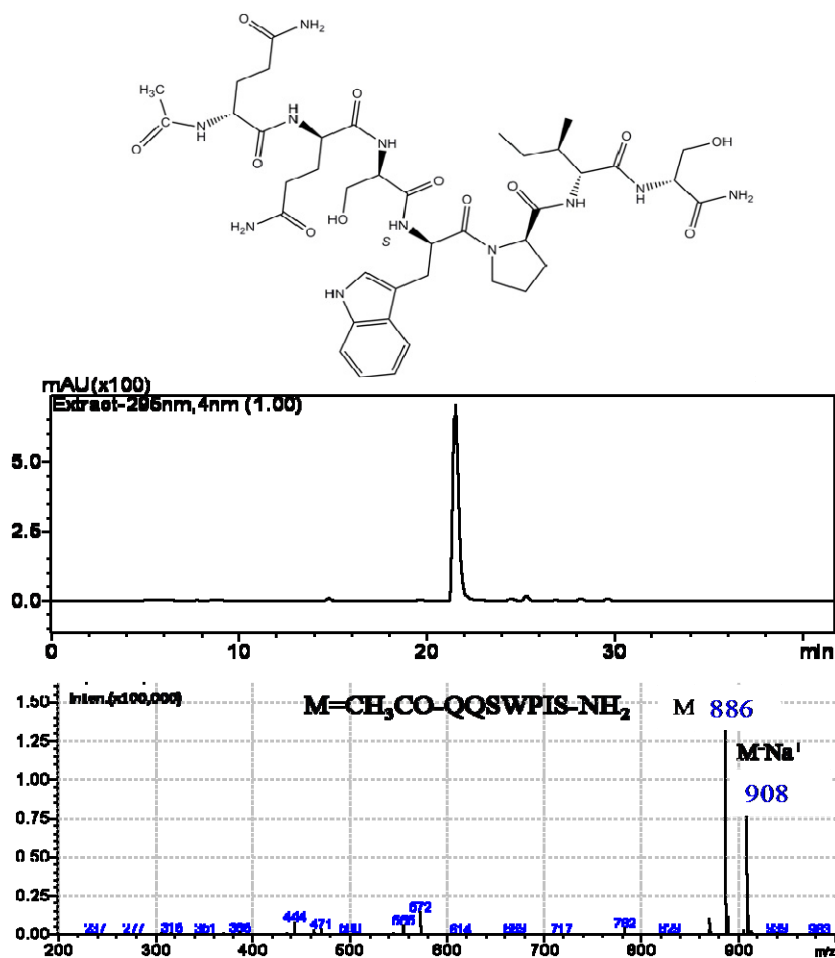


**Figure 2.1** The molecular structure of Q7 peptide and its purity characterization with LC-MS.

### B. Pd NCs synthesis with selected peptides

A set of reactions were carried out to synthesize Pd NCs in the presence of peptides with different amount of reducing agent,  $\text{NaBH}_4$ . Three vials containing 1 ml of 5 mM  $\text{Na}_2\text{PdCl}_4$ , 250  $\mu\text{l}$  of 2 mg  $\text{ml}^{-1}$  peptide solution and different volume of de-ionized water, 3.7 ml, 3.65 ml and 3.6 ml for reacting with  $\text{NaBH}_4$ . 50  $\mu\text{l}$ , 100  $\mu\text{l}$  and 150  $\mu\text{l}$  of 50 mM  $\text{NaBH}_4$  were injected to three pre-prepared solutions to have 0.5 mM, 1 mM and 1.5 mM of  $\text{NaBH}_4$  in reaction solutions. The final peptide concentration was 100  $\mu\text{g ml}^{-1}$  and the final concentration of  $\text{Na}_2\text{PdCl}_4$  was 1 mM.

The color of the solutions changed from yellow to brown as soon as the injection of NaBH<sub>4</sub>, indicating the reduction of Pd ions to Pd metal. The reactions were carried out in aqueous solution at room temperature with a total volume of solution 5 ml. By using these as-synthesized Pd NCs as seeds, seeding growth was performed to synthesize larger-sized Pd NCs. For each different-sized seed solution, 50 μl, 100 μl and 200 μl of growth solution (5 mM of Na<sub>2</sub>PdCl<sub>4</sub>) were added respectively into the seeds solutions and kept vigorous stirring for one hour. TEM samples were prepared with carbon substrates on copper grids. Transmission Electron Microscopy (TEM) and High-Resolution TEM (HRTEM) characterization of the obtained Pd NCs were imaged on Philips CM120 with a 120 kV operation voltage and FEI TITAN with a 300 kV operation voltage, respectively.

### **C. Results and discussion**

As shown in Figure 2.2, the obtained Pd NCs from the blank, negative, and positive control reaction are very different. The Pd NCs from the blank reaction have a size of  $36 \pm 9$  nm, while those found in negative control with nonspecific peptide are aggregates of small nanoparticles. In the positive control reaction with Q7 peptide, monodispersed Pd NCs with a size of  $2.9 \pm 0.4$  nm are obtained. These results suggest that both peptides have effect on crystal grow of Pd nanoparticles due to the size reduction in comparison with blank control, while only Q7 can effectively bind on Pd metal surface and stabilize them in solution.

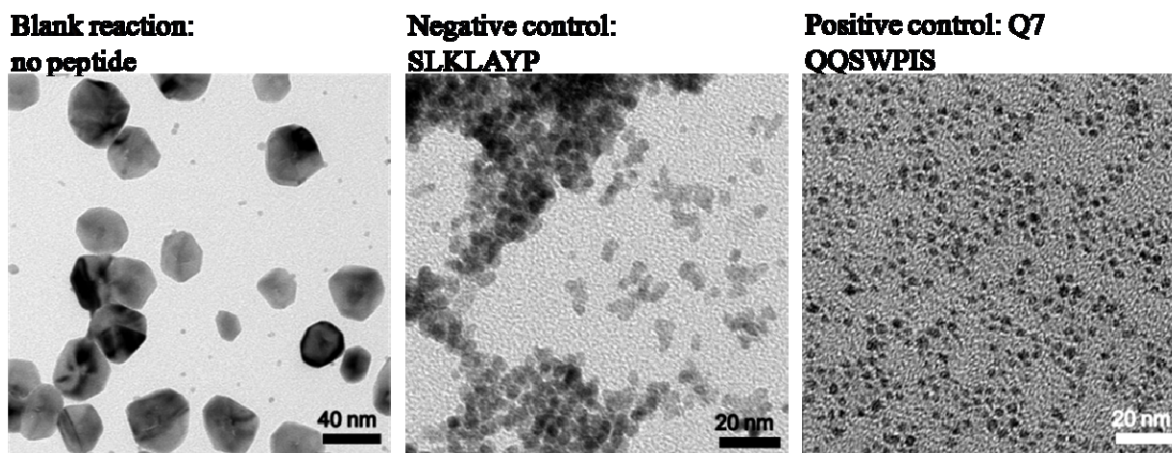


**Figure 2.2** TEM images of Pd NCs obtained from the blank reaction (without peptide) and the reactions in the presence of nonspecific peptide (negative control, SLKLAYP) and Pd specific peptide (positive control, Q7: QOSWPIS) at reaction time 10 minutes.

Q7 peptide shows a hydroxyl- and amide- group rich motif, which is similar to the previously reported Pd binding peptide sequence.<sup>35</sup> These function groups contribute to the strong binding ability of Q7 on Pd crystal surface. In addition, Q7 has a tryptophan (W) which has been reported to be able to reduce silver and gold ions.<sup>41</sup> In our study, we also found Q7 can reduce Pd ion precursor due to the presence of W in Q7. To confirm this, we studied the effects of W, Q7 (QOSWPIS) and Gln-Gln-Ser-Pro-Ile-Ser (QQSPIS, termed as Q6) on the Pd NCs growth, respectively. 500 mg ml<sup>-1</sup> of W, Q7 and Q6 were incubated in 5 mM Na<sub>2</sub>PdCl<sub>4</sub> solutions, respectively. Figure 2.3a shows the color evolution of the three incubations containing W, Q7 and Q6. After 4 h of incubation, it was found that the color of the solutions containing W and Q7 changed from light yellow to brown, indicating both W and Q7 performed the same effect on reducing Pd ions (the formation of Pd metals were observed with TEM), while the color of the solution containing Q6 displayed no change after 4 h, which confirms that it was the W residue that has the reducing power and the rest of the residues (i.e., Q6) only contributed to the binding ability of the Q7 sequence. To elucidate the role of W in binding on Pd, Pd NCs were

synthesized with  $100 \text{ mg ml}^{-1}$  of W, Q7 and Q6, respectively. A TEM image of the obtained Pd NCs from W-contained reaction was taken at 1 min of the reaction as shown in Figure 2.3b, which shows severe aggregation of Pd NCs. The precipitation was found in the solution within 3 min after the introduction of  $\text{NaBH}_4$ , while NCs from Q7- and Q6- stabilized reactions were stable even after a couple of hours (Figure 2.3c and d). In addition, the Q7-stabilized Pd NCs displayed more uniform shape and better size distribution in comparison with Q6-stabilized Pd NCs, which would grow to ca. 10 nm and coalesce. These results suggest that the W residue in Q7 plays an important dual role in Pd NC synthesis in both the reduction of  $\text{Na}_2\text{PdCl}_4$  and the tight binding to Pd surface. We continued to exploit the dual functionality of Q7 to obtain mono-dispersed Pd NCs with controllable sizes in aqueous solution.

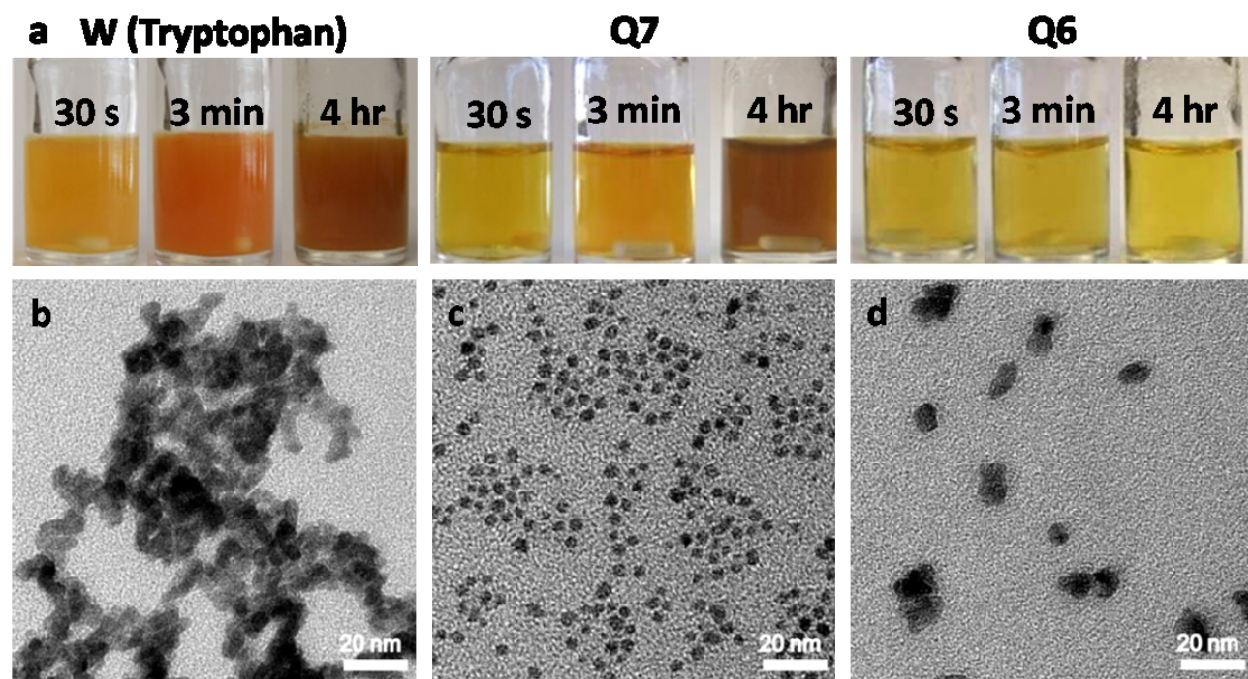


**Figure 2.3** (a) Photo images of color evolution of  $\text{Na}_2\text{PdCl}_4$  precursor incubation with W, Q7 and Q6, respectively. (b-c) TEM images of Pd NCs synthesized by W, Q7 and Q6, respectively, using  $\text{NaBH}_4$  as reducing agent in the reactions.

Combing an external reducing agent ( $\text{NaBH}_4$ ) and the self-reducing power of Q7, precise control over the size of Pd NCs were achieved. Different concentration of  $\text{NaBH}_4$  was used to control the nucleation state of Pd seeds syntheses. Briefly, various amount of 50 mM  $\text{NaBH}_4$  (i.e., 50, 100, and 150  $\mu\text{l}$ ) were injected to the solution containing 1 mM  $\text{Na}_2\text{PdCl}_4$ , 100 mg  $\text{ml}^{-1}$  Q7 peptide, and the final concentration of  $\text{NaBH}_4$  is 0.5, 1, 1.5 mM, respectively. As shown in Figure 2.4, the Pd NCs formed in the early stage of reactions were well-dispersed in solution. With decreasing the concentration of  $\text{NaBH}_4$  from 1.5, 1 to 0.5 mM, the average size of Pd NCs increased from 2.2, 2.7 to 3.0 nm, respectively. The introduction of the strong reducing agent led to the rapid reduction of Pd ions and generated a burst of Pd atoms which resulted in Pd crystal growth. The resulting small Pd nuclei or clusters were instantly covered and stabilized by Q7 peptides, preventing the coalescence of the small nuclei or clusters. With decreasing concentration of  $\text{NaBH}_4$ , fewer Pd atoms were generated, resulting the decreased nuclei numbers and increased Pd NC sizes. Interestingly, the Pd NCs continued to grow slowly for a long period of time after the introduction of  $\text{NaBH}_4$ . As shown in Figure 2.5, after 1 hour of reaction time, Pd NCs grow from 2.2, 2.7 and 3.0 nm to 2.6, 3.4 and 4.3 nm, respectively. The successive crystal growth was a result of the Q7 peptides which also perform reducing effect on Pd ions in addition to stabilization effect on Pd NCs.

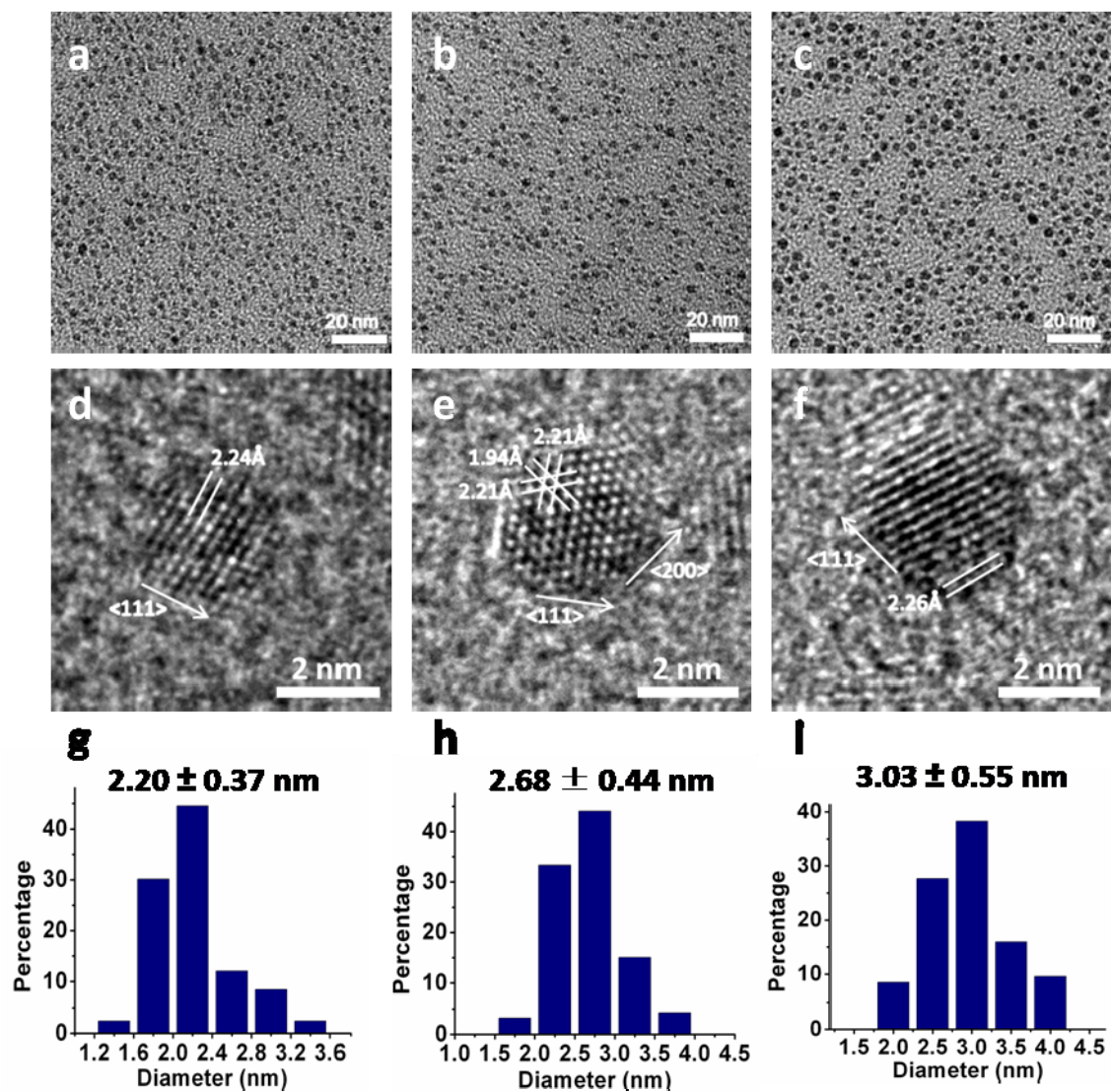


**Figure 2.4** (a-c) TEM images of Pd NCs obtained from the 20 seconds' reactions with different concentration of NaBH<sub>4</sub>: 1.5 mM (a), 1 mM (b) and 0.5 mM (c). (d-e) are HRTEM images of the representative NC in (a-c), respectively. (g-h) the corresponding size distribution of NCs in (a-c).

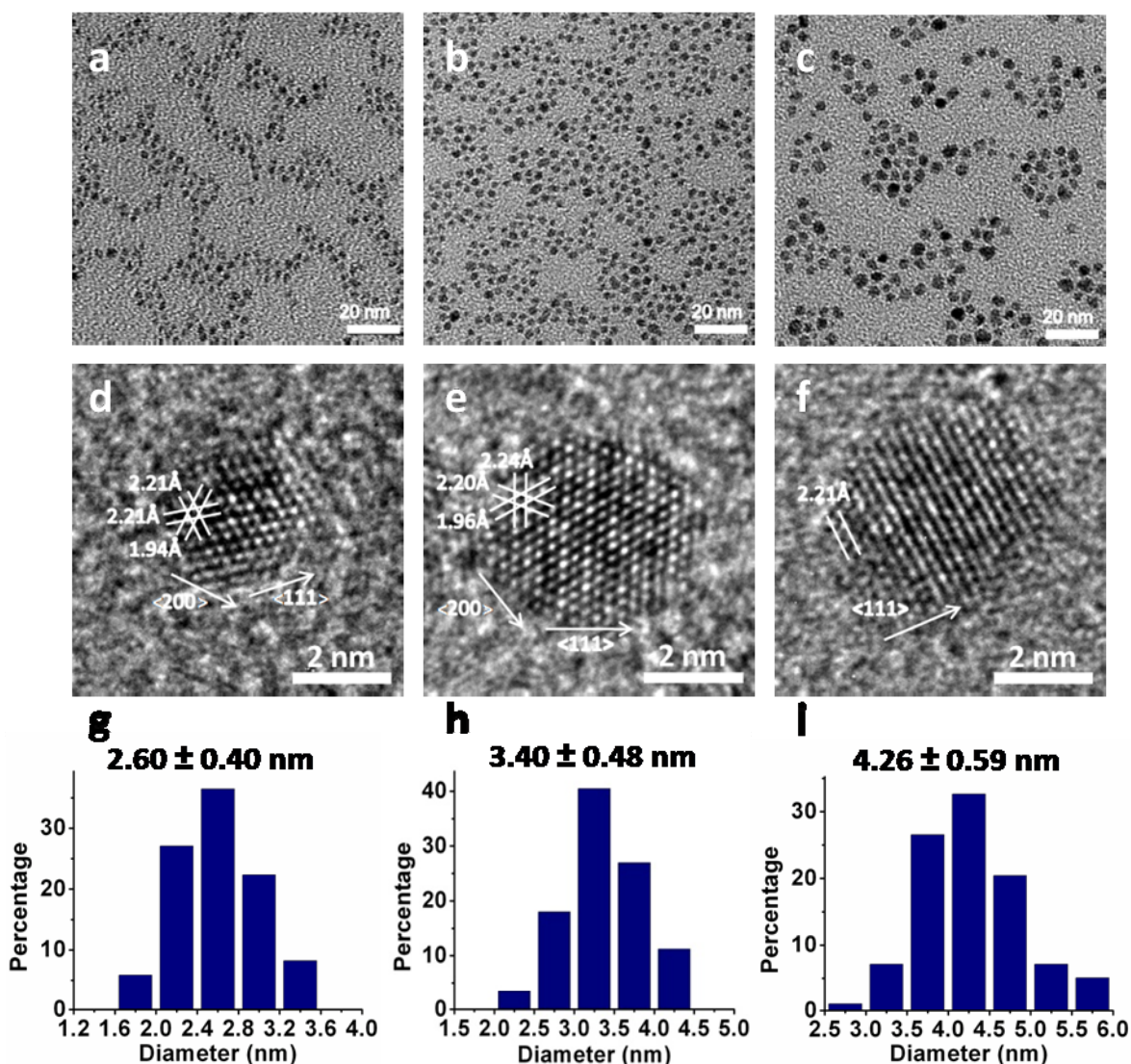


**Figure 2.5** (a-c) TEM images of Pd NCs obtained from the 1 hour's reactions with different concentration of NaBH<sub>4</sub>: 1.5 mM (a), 1 mM (b) and 0.5 mM (c). (d-e) are HRTEM images of the representative NC in (a-c), respectively. (g-h) the corresponding size distribution of NCs in (a-c).

It is worth to note that the growth in size is most significant for larger nuclei which were produced with a lower concentration of NaBH<sub>4</sub>. This is attributed from the difference of the unreacted precursor after diminish of NaBH<sub>4</sub>. For example, after the nucleation event, the reaction with 0.5 mM NaBH<sub>4</sub> had most left-over Pd ions precursor in the solution which led to a faster reduction rate via Q7, which led to the observation of Pd NCs grew from 3.0 to 4.3 nm from 20 s



to 1 h of reaction time. While in the reaction solution with 1.5 mM NaBH<sub>4</sub>, a small increase from 2.2 to 2.6 nm was observed due to the fewer amount of available precursor. These results suggest that at growth stage it is Q7 peptide not NaBH<sub>4</sub> dominated Pd ions reduction since higher concentration of NaBH<sub>4</sub> did not lead to larger-sized Pd NCs. These observations indicate that the size of Pd NCs is controlled by the concentration of the reducing agent as well as the amount of the precursor in solution. A set of experiments were then carried out to fine tune the size of Pd NCs over the range of 2 to 7 nm by exerting controls over both the nucleation and crystal growth of Pd NCs. Three seed solutions were prepared with different concentrations of NaBH<sub>4</sub> as described above, in which the Pd NCs have a size of 2.6 nm, 3.4 nm and 4.3 nm, respectively (Figure 2.6 a, e, and i). Different amount of 5 mM of Na<sub>2</sub>PdCl<sub>4</sub> (i.e., 50, 100 and 200 μl) was introduced as the growth solution and no external reducing agent was needed in crystal growth stage. As shown in Figure 2.6, the obtained Pd NCs have a size ranging from 2.6 to 6.6 nm from the seeding growth reactions, respectively.

To put together, a facial approach to synthesize mono-dispersed sub-10 nm Pd NCs with fine-controllable size rang has been demonstrated. A multifunctional peptide, Q7 was identified to perform binding effect on Pd metal, stabilizing different-sized Pd nuclei. In addition, its reducing power to reduce Pd ions facilitates the continued crystal growth on the initial nuclei, leading to a size control synthesis of Pd NCs. It is found the amino acid, W, plays an important role in this recuing effect. Exploiting the discovered features of Q7 peptide, Pd NCs with tunable sizes ranging from 2.6 to 6.6 nm have been produced.

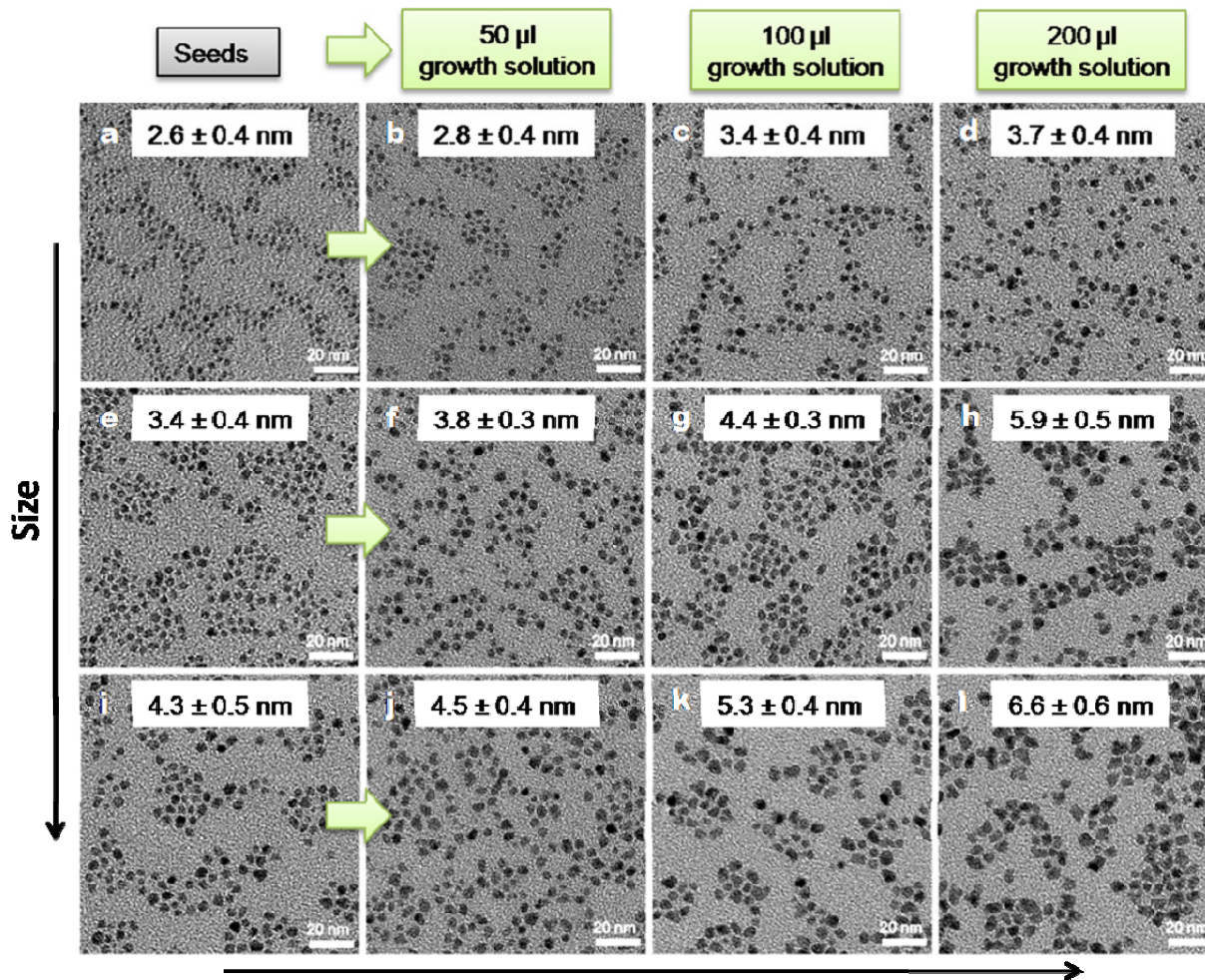


**Figure 2.6** TEM images of the Pd NCs obtained from the seeding growth controlled reactions with different amount of growth solution. (a, e and i) are the initial seeds with three different sizes. (b-d) show the size evolution of Pd NCs from (a) with different volume of growth solution from 50  $\mu$ l, 100  $\mu$ l to 200  $\mu$ l, respectively. Similarly, (f), (g) and (h) and (j), (k) and (l) evolve from (e) and (i), respectively by seeding growth to control the size of Pd NCs. Reaction time was 1 hour for all reactions.

### **Chapter III: SHAPE-CONTROLLED SYNTHESIS OF PLATINUM NANOCRYSTALS USING FACET-SPECIFIC PEPTIDES**

The precedent studies including some of our group's in biomimetic synthesis have shown that the selected peptides through biopanning can mediate the syntheses of nanomaterials with a well-controlled size and morphology.<sup>40,42-43</sup> Nevertheless, a rational approach to select peptide showing binding specificity to certain material or a particular crystallographic is not achieved yet, limiting the advancement of the understanding of the interfacial interaction of peptides and the full potential of the peptides in engineering nanostructures. It is of importance to continue our studies to develop an approach to synthesizing NCs with predictable shapes through the selection of facet-specific peptides. Here, we demonstrated a rational biomimetic approach to the predictable synthesis of NCs enclosed by particular facet in the case of Pt.<sup>44</sup> Pt is an excellent catalytic material for various important reactions such as hydrogenation and the catalytic activity and selectivity are highly sensitive to different crystallographic planes.<sup>14-17</sup> Therefore, controlling the exposed facet on a Pt NCs is very important to advance Pt catalysis by increasing the selectivity and efficiency of Pt nanocatalyst.

#### **A. Facet-specific peptide selection and results**

Similar to the previous description, Ph.D -7mer peptide library was used to selected Pt {100} and Pt {111} facet-specific peptides. The target materials are Pt faceted substrates which were prepared by drop-casting Pt nanocubes (enclosed by six {100} facets) and Pt nano-octahedrons (enclosed by six {111} facets) on Si substrates, respectively, as shown in Figure 3.1. These Pt cubes and Pt octahedrons were synthesized based on the variant of previously reported recipes.<sup>45-46</sup> After washing, the surfactants on Pt cubes and Pt octahedrons were removed by ozone and oxygen plasma, respectively. We conducted the peptide selection cycles for these two substrates, individually. For each round of biopanning, we used a brand new target substrate.

Before each round of biopanning, the substrates were sterilized in 99% ethanol for 30 minutes with gentle rocking, followed by washing with 5 times of sterilized water and TBS. The biopanning process is similar to the previously described, but for each round after elution we conducted a negative selection to exclude phage bound on the surface of Si substrate by incubating the eluted phage with bare Si substrate and rocking for 1 hour. After several selection cycles, two peptide sequences T7 and S7 were identified as Pt {100} and Pt {111} facet-specific peptide, respectively. T7 is Ac-Thr-Leu-Thr-Thr-Leu-Thr-Asn-CONH<sub>2</sub> (TLTTLTN, MW: 803.92) and S7 is Ac-Ser-Ser-Phe-Pro-Gln-Pro-Asn-CONH<sub>2</sub> (SSFPQPN, MW: 816.88). The purified peptides were characterized with LC-MS and shown in Figure 3.2, confirming they are pure peptide products as required for Pt NCs synthesis.

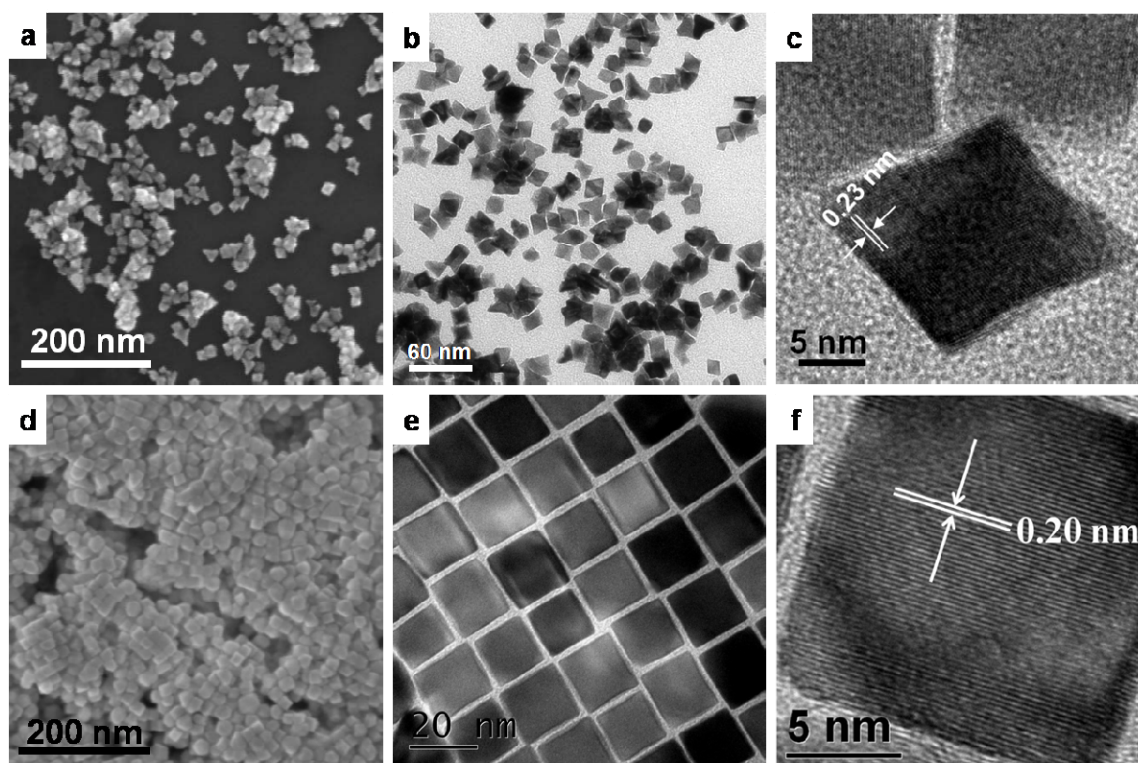


**Figure 3.1** Starting substrates for peptide selection. SEM images of Pt octahedrons (a) and Pt cubes (d) on Si substrates, respectively. (b-c) show TEM and HRTEM images of as-synthesized

Pt octahedrons, respectively. (e-f) show TEM and HRTEM images of as-synthesized Pt cubes, respectively.

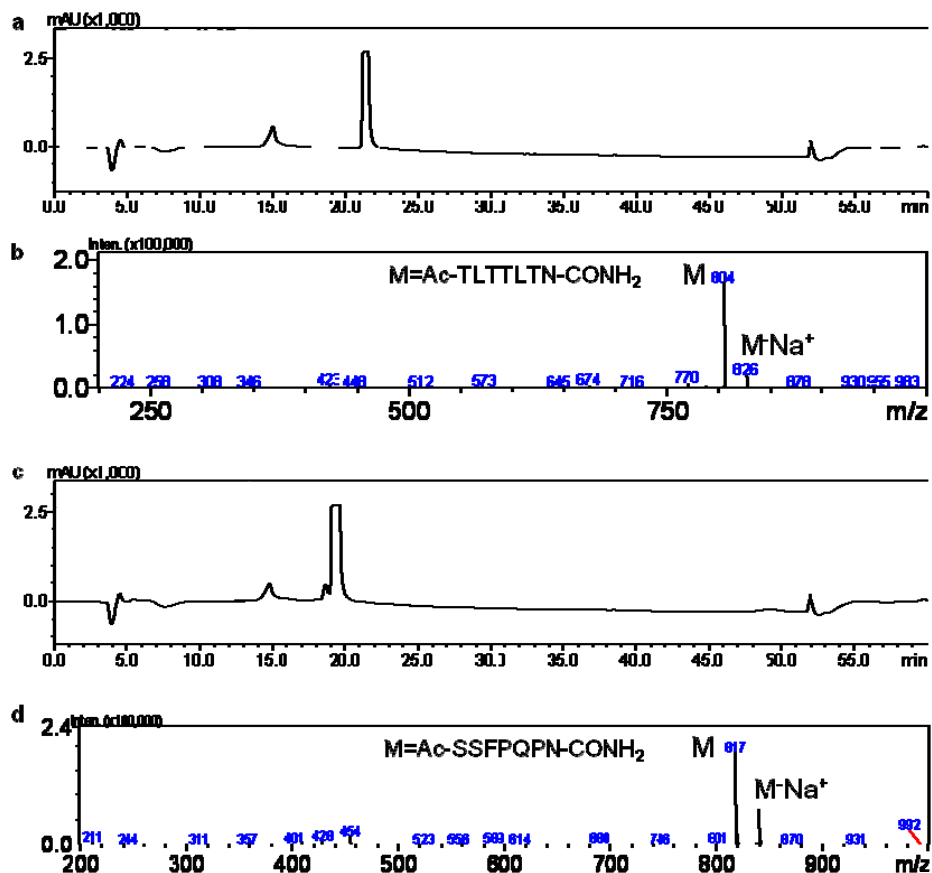


**Figure 3.2** Liquid chromatography (LC) of the T7 peptide (a) and its corresponding mass spectrum of the samples eluted at about 21.5 min (b). Liquid chromatography (LC) of the S7 peptide (c) and its corresponding mass spectrum of the samples eluted at about 19.5 min (d).

### B. Shape control synthesis of Pt NCs with selected peptides

Chloroplatinic acid hydrate ( $\text{H}_2\text{Pt(IV)Cl}_6 \cdot x \text{H}_2\text{O}$ , 99.9+% trace metals basis, Aldrich) was used as precursor. Sodium borohydride ( $\text{NaBH}_4$ , Aldrich) and ascorbic acid (Aldrich) were used as reducing agents. All reagents are dissolved in water before use. For all reactions, a pre-prepared vial containing precursor and peptide in aqueous solution was mixed with ascorbic acid right before the injection of fresh  $\text{NaBH}_4$ . TEM samples were prepared at different reaction times.

In the series of control reactions to compare the peptide effects on NC shapes, 1 mM of  $\text{H}_2\text{PtCl}_6$ , 30  $\mu\text{g/ml}$  of peptides (T7, S7 or BP7A: Thr-Leu-His-Val-Ser-Ser-Tyr previously selected against bulk Pt polycrystalline surface)<sup>ref</sup> and 2 mM of ascorbic acid were pre-mixed in a vial and injected one shot of  $\text{NaBH}_4$  with a final concentration 0.8 mM. To observe the shape evolution of Pt cubes, we prepared a solution with 1 mM of  $\text{H}_2\text{PtCl}_6$ , 10  $\mu\text{g/ml}$  of T7 peptide and 5 mM of ascorbic acid in a vial and injected one shot of  $\text{NaBH}_4$  with a final concentration 0.8 mM. For the tetrahedron synthesis, 1 mM of  $\text{H}_2\text{PtCl}_6$ , 30  $\mu\text{g/ml}$  of S7 peptide and 2 mM of ascorbic acid were pre-prepared in a vial and injected one shot of  $\text{NaBH}_4$  with a final concentration 0.8 mM. All concentrations given here are final concentrations. The final volume of all reaction solutions is 5 ml. All TEM samples were prepared by pipetting the NCs solution onto the carbon coated copper grids. The TEM samples were dried in atmosphere before taking images. TEM images were taken on FEI CM 120 microscope operated at 120 kV. High resolution TEM images were captured on FEI TITAN microscope operated at 300 kV.

## **C. Results and discussion**

### **Facet-selectivity of T7 and S7 peptide**

In my studies, we used a quick single-shot injection of  $\text{NaBH}_4$  to reduce Pt ion precursor and produce a burst of nucleation. Ascorbic acid can then gradually reduce residual Pt ion precursor to produce Pt atoms that are preferentially added onto the higher energy facets on which the peptide shows no selective binding. As shown in Figure 3.3a and b, a rational approach to select Pt facet-specific peptides and use them in shaping Pt NCs is described. Importantly, these identified peptides (i.e., T7 and S7) can be exploited to control the growth of Pt NCs with distinguishable shapes with similar synthetic methods at room temperature in aqueous solution, indicating their ability in selectively stabilizing a particular colloidal metal

surface. The molecule structure of T7 and S7 are shown in Figure 3.4. T7 can produce cubes enclosed by six  $\{100\}$  facets (Figure 3.3c) and S7 produce tetrahedrons enclosed by four  $\{111\}$  facets (Figure 3.3d), as expected. The facet specificities of the Pt- $\{100\}$  binding peptide sequence T7 and Pt- $\{100\}$  binding peptide sequence S7 are further confirmed by a blank control (reaction without peptides present) and a negative control (BP7A) experiments, both showing obviously different shapes from cubes and tetrahedrons (Figure 3.3e and f). In addition, under different synthetic conditions with different platinum precursors, we have observed similar phenomena (Figure 3.5), further confirming the role of facet-specific peptides in leading shape-controlled synthesis.

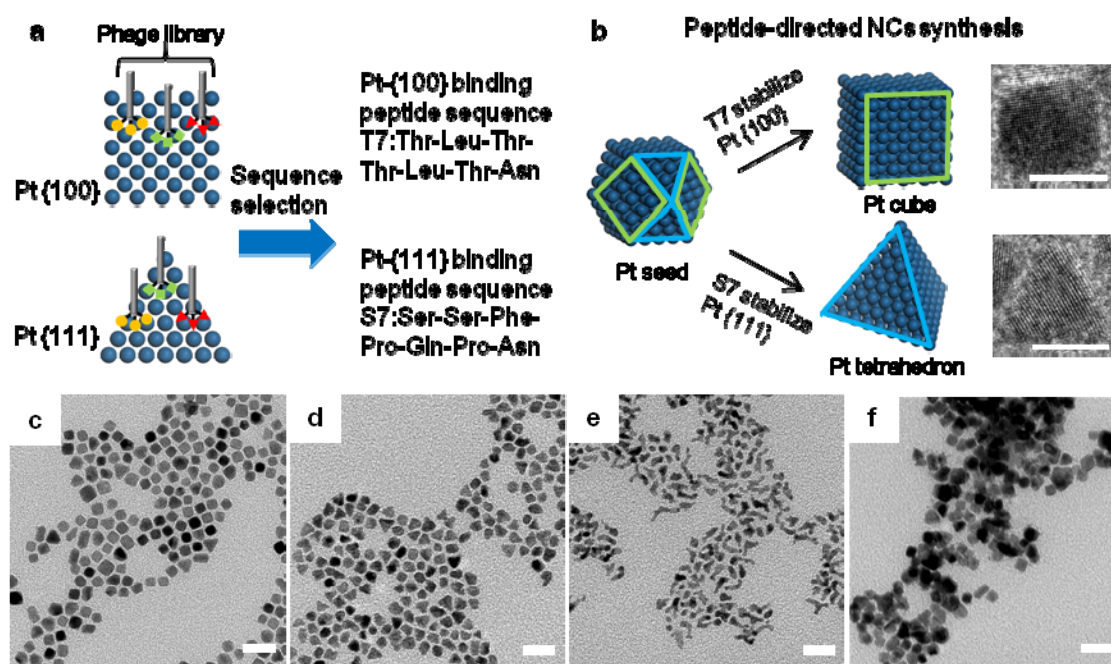


**Figure 3.3** Biomimetic synthesis of shaped Pt NCs by selected peptides. (a-b) Schematic illustrations of facet-specific peptide sequence selection and shape control of cube and tetrahedron. (a) Pt- $\{100\}$  binding peptide sequence T7 and Pt- $\{111\}$  binding peptide sequence S7 are selected against  $\{100\}$  faceted and  $\{111\}$  faceted substrates. (b) Facet-specific peptides are then used to direct the synthesis of Pt NCs with shape control. Insets: HRTEM images of Pt

nanocube controlled by T7 and Pt nano-tetrahedron by S7, respectively, scale bars are 5 nm. (c-f) TEM images of Pt NCs obtained from different peptide-regulated reactions: T7 (c), S7 (d), BP7A (e), and blank reaction (f). All samples were conducted under the same synthesis conditions and collected after reacting for 10 minutes; scale bars: 20 nm.

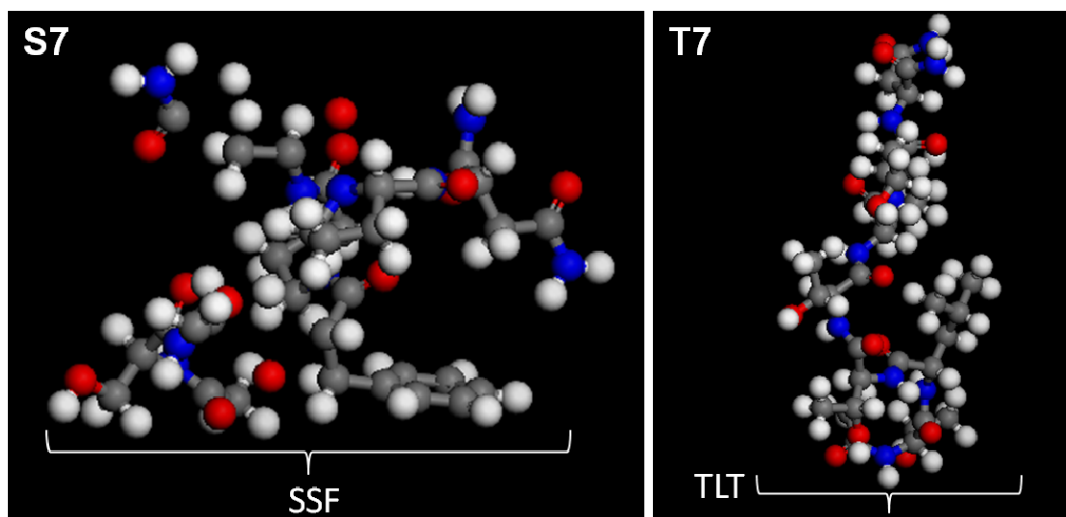


**Figure 3.4** Molecules structure of S7 and T7 peptides.

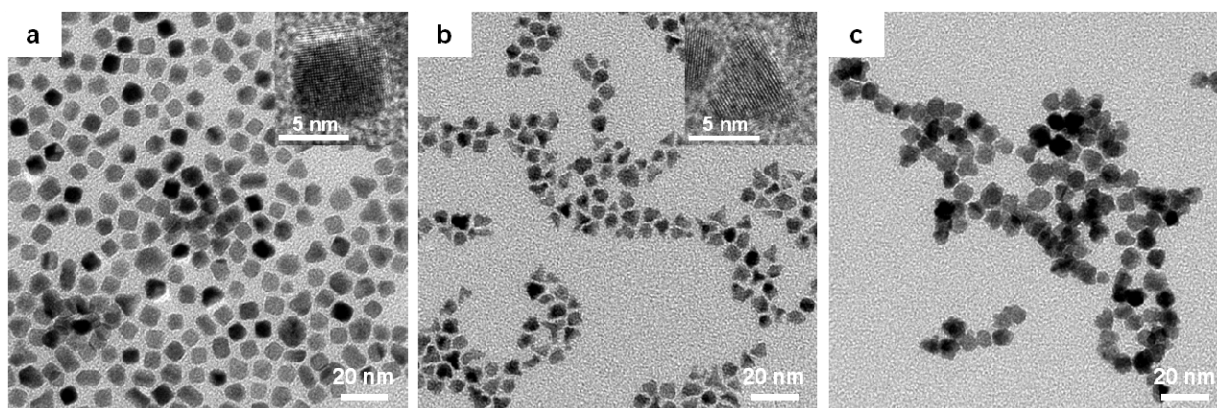


**Figure 3.5** Shape control synthesis of Pt NCs using  $K_2PtCl_4$  as precursor. (a) TEM image of the obtained NCs from T7- control reaction (1 mM of  $K_2PtCl_4$ , 10  $\mu\text{g/ml}$  of T7; 1 mM of ascorbic acid; 0.8 mM of  $NaBH_4$ ). (b) TEM image of the obtained NCs from S7- control reaction (1 mM of  $K_2PtCl_4$ , 30  $\mu\text{g/ml}$  of S7; 0.5 mM of ascorbic acid; 0.8 mM of  $NaBH_4$ ). (c) Blank controlled



reaction (1 mM of  $K_2PtCl_4$ , 0.5 mM of ascorbic acid; 0.8 mM of  $NaBH_4$ ). The concentrations addressed here are final concentration with a final solution volume, 5 ml.

### **Shape evolution of nanocube and nano-tetrahedron**

To show the effect of the facet-specific binding peptides on the crystal growth of NC enclosed by particular facets, we observed the shape evolution of both T7- and S7-regulated Pt NC synthesis over time. T7 with the selective binding affinity to Pt {100} faces should be able to lower surface energy of Pt-{100} and inhibit the growth rate along  $\langle 100 \rangle$  directions, thus leading to a gradual increase of Pt {100} facets displayed on NCs. Similarly, the gradual increase of Pt-{111} facets over reaction time is expected in S7-regulated Pt NC synthesis. These are consistent with our observations in the experiments, as shown in Figure 3.6 and Figure 3.7.

In Figure 3.6, the Pt NCs synthesis was carried out with T7 peptide as the capping agent, with a single shot of  $NaBH_4$  to create a quick burst of nuclei and 5 mM of ascorbic acid to control the subsequent NC growth on to the nuclei. Overall, the Pt NCs grow larger and their shape became more distinguishable with increasing reaction time. After the injection of  $NaBH_4$  ( $<10$  s), the NCs obtained due to the fast nucleation are mostly spherical with a size of  $4.9 \pm 1.3$  nm (Figure 3.6 a and j). The corresponding HRTEM image shows typical hexagonal-shaped NC that was identified as truncated octahedron bound by six {100} and eight {111} facets, supported by its Fourier transform (FT) pattern along [110] zone axis (Figure 3.6b). Some NCs are found to have cube-like shape as shown by FT pattern along [001] zone axis (Figure 3.6c), suggesting they are cube-like NCs formed at very early growth stage. As the reaction time reached 1 minute, the Pt cubic NCs was more developed (Figure 3.6d and k), showing 53% of cubes with an average size of  $6.7 \pm 0.9$  nm. Their corresponding HRTEM images in Figure 3.6e confirm that the truncated octahedron with much more growth in  $\langle 111 \rangle$  than in  $\langle 100 \rangle$  directions, resulting in

an increase in {100} and a reduction in {111} facets. Furthermore, the truncated cube observed in 1 minute's reaction time has smaller truncated facets, showing more perfect cubic shape (Figure 3.6f). After 30 minutes of reaction time, the NCs evolved to be larger and have 70% of cubes and 13% of truncated cubes (Figure 3.6g and l), showing an average size of  $7.6 \pm 1.0$  nm. Figure 3.6h and i show the HRTEM images of the final evolved shape of NCs from the reaction controlled by T7, demonstrating the formation of single crystalline Pt cubes enclosed by {100} facets. In addition, the other shaped NCs found in the final products were identified as incomplete truncated cubes with different facets in a variable extent but predominantly enclosed by {100} facets as shown in Figure 3.7. To put together, we have observed the NC shapes evolve from {111} and {100} enclosed truncated octahedron to {100} only enclosed cubes. The observation of anisotropic growth was attributed to the effect of Pt {100}-binding peptide sequence, T7, which can stabilize {100} faces and slow down atom addition on them. This has resulted in the relative faster crystal growth along  $\langle 111 \rangle$  directions, eventually eliminating {111} facets displayed in the final cubic NCs.

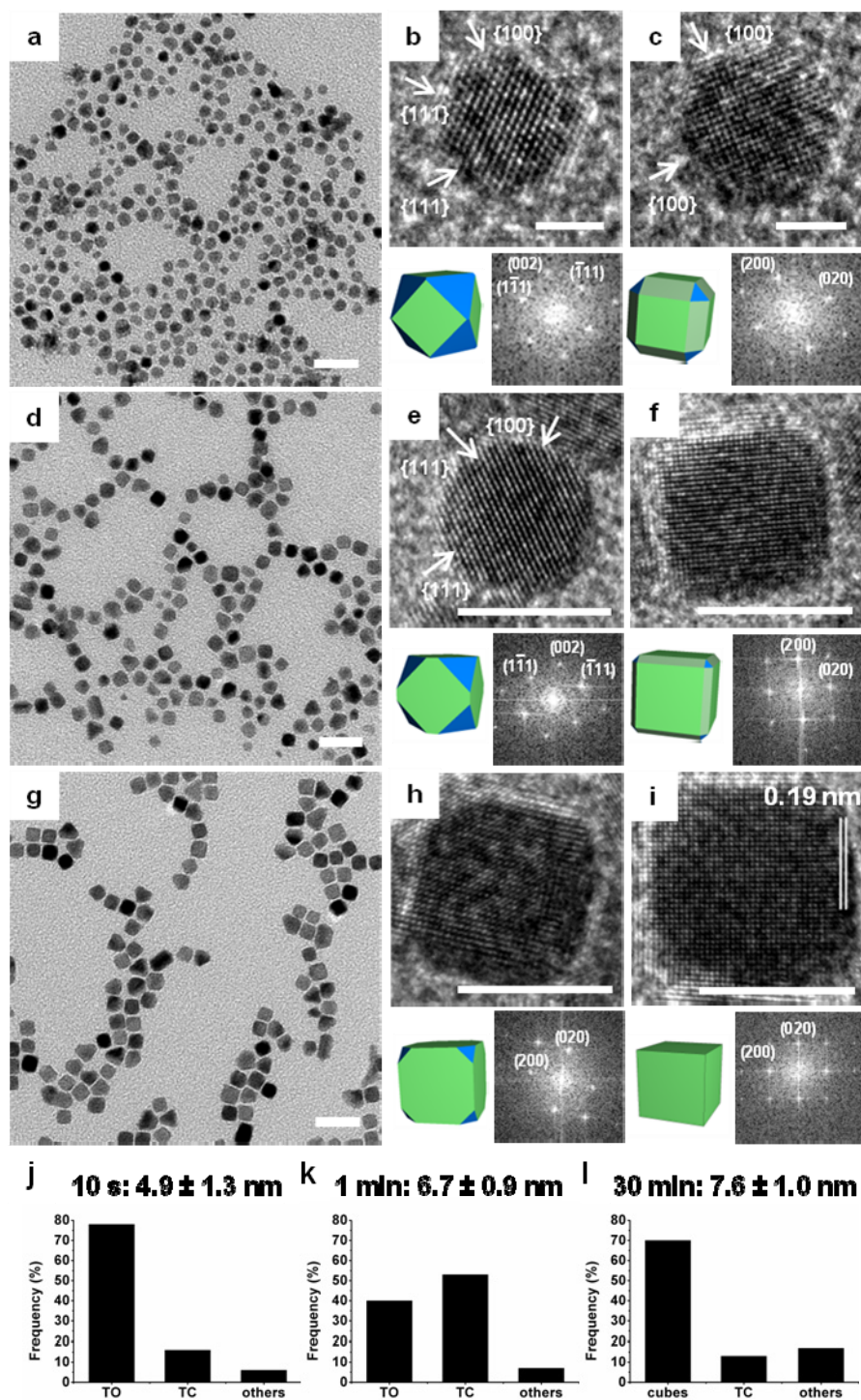


**Figure 3.6** Shape evolution of Pt cubes controlled by T7. TEM and HRTEM images of the NCs obtained from the reaction at different time: (a-c) 10 s, (d-f) 1 min, (g-i) 30 min. (j-l) The corresponding shape and size distributions of the NCs in a, d and g, respectively. The schematics

show the corresponding geometrical model of the obtained NCs. The green, blue and grey colors denote the  $\{100\}$ ,  $\{111\}$  and  $\{110\}$  facets, respectively. The scale bars are 20 nm in a, d and g; 2 nm in b and c; 5 nm for e, f, h and i. TO: truncated octahedrons; TC: truncated cubes.

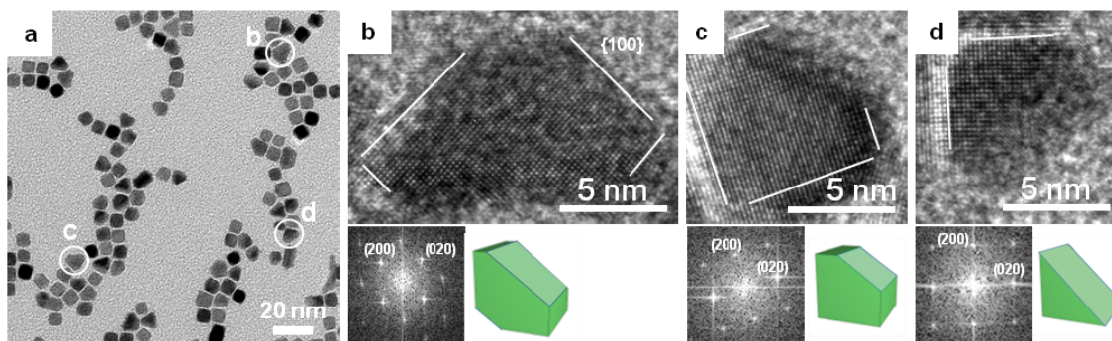


**Figure 3.7** HRTEM images of incomplete cubes obtained from the T7 controlled reaction. (a) TEM image of the Pt cubes controlled by T7. (b-d) HRTEM images of truncated cubes and their corresponding FT patterns and schematic models, indicating the non-cubic like NCs are incomplete cubes predominated enclosed by  $\{100\}$ .

In similar reaction conditions, while changing the capping agent to S7 peptide we showed the synthesis of Pt tetrahedrons in aqueous solution at room temperature. Similar trend has been observed in the S7 controlled reaction, in which S7 can selectively bind on  $\{111\}$  facets, increase the crystal growth on other facets than  $\{111\}$  and eventually facilitate the formation of Pt tetrahedrons enclosed by  $\{111\}$  facets only. Figure 3.8 shows the shape evolution of tetrahedrons controlled by S7. Initially, mono-dispersed Pt NCs with ca. 3-4 nm in size formed instantly (<10 s) after the introduction of  $\text{NaBH}_4$  into the reaction (Figure 3.8 a and j). Their corresponding HRTEM images and FT patterns (Figure 3.8b and c) confirm that the representative NCs are truncated octahedrons enclosed by  $\{100\}$  and  $\{111\}$  facets, or truncated tetrahedrons predominately enclosed with  $\{111\}$  facet. With the reaction proceeded with time, it was found that Pt NCs grew larger in size ( to  $6.0 \pm 0.9$  nm after 1 hour) with more developed tetrahedron

shapes (Figure 3.8 d-i, k-l), indicating S7 can decelerate growth rate along  $\langle 111 \rangle$  directions through stabilizing  $\{111\}$  surface. HRTEM images of Pt tetrahedron recorded along the  $[112]$  and  $[110]$  zone axes, respectively, confirm that the diamond-like and triangular shape of NCs observed in Figure 3.8g belong to different projections of Pt tetrahedrons (Figure 3.8h and i). Additionally, different Pt nano-tetrahedron projections corresponding to a set of different shaped NCs which were observed in Figure 3g are included in Figure 3.9. These observations proved that the introduction of S7 in Pt NCs synthesis can selectively stabilize Pt  $\{111\}$  facets, resulting in the formation of Pt tetrahedron NCs.

We also observed that the yield or the development of shape of NCs depend on the peptide concentration. For example, for both T7 and S7 there is an optimal peptide concentration that led to a high yield of complete cubes and tetrahedrons, respectively (Figure 3.10). The optimal concentrations were found to be 10  $\mu\text{g/ml}$  for T7 and 30  $\mu\text{g/ml}$  for S7. We think that below the optimal concentration there is not enough peptide to cover all specific facets on the NC surface, leading to less developed shapes. However, if the peptide concentration is higher than optimal, the excessive peptide molecules may start to bind to non-specific facets other than  $\{111\}$  or  $\{100\}$ , leading to less distinguished tetrahedrons or cubes. Importantly, we observed that although tuning peptide concentrations may lead to the degree with which the shape is controlled, it does not lead to the formation of the opposite shaped NCs, i.e., T7 cannot lead to the formation of tetrahedron dominated NCs, neither can S7 form cubes. This observation is in huge contrast with a previously reported chemical method, wherein varying surfactant concentrations would result either cubes or tetrahedrons.<sup>47</sup> These results further confirm the specificity of the selected facet-binding peptide sequences.

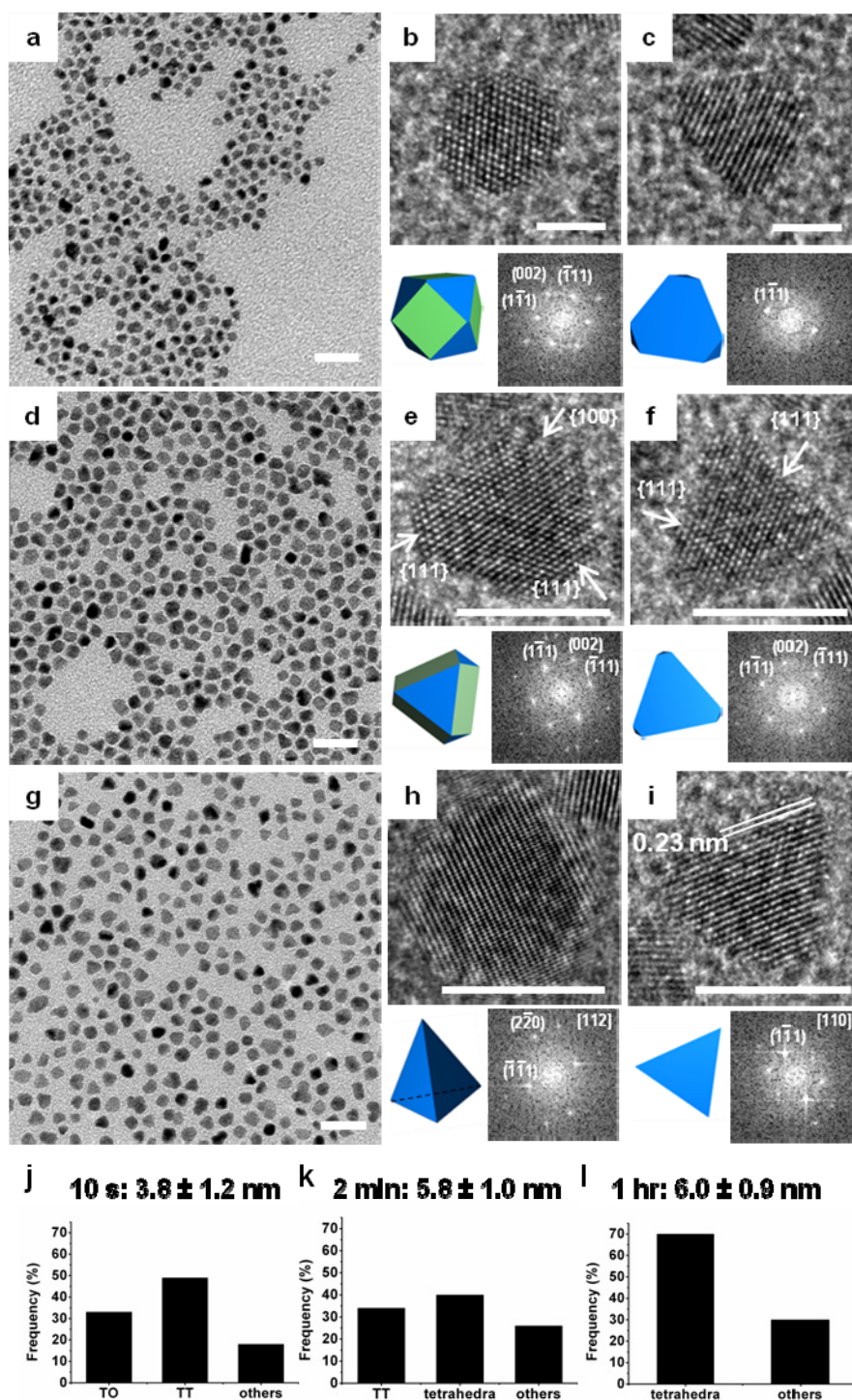


**Figure 3.8** Shape evolution of Pt tetrahedrons controlled by S7. TEM and HRTEM images of the NCs obtained from the reaction at different time: (a-c) 10 s, (d-f) 2 min and (g-i) 1 hr. (j-l) The corresponding shape and size distributions of the NCs in a, d and g, respectively. h and i

demonstrate tetrahedrons projected along  $[112]$  and  $[110]$  zone axis, respectively. In the corresponding geometrical models, the green and blue colors denote the  $\{100\}$  and  $\{111\}$  facets, respectively. The scale bars are 20 nm in a, d and g; 2 nm in b and c; 5 nm in e, f, h and i. TO: truncated octahedrons; TT: truncated tetrahedrons.

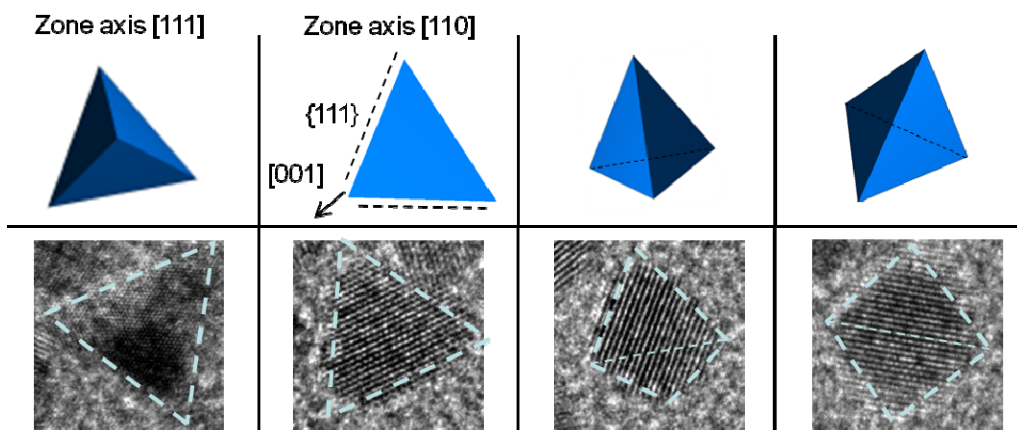


**Figure 3.9** Schematic models of tetrahedron projected along different directions and their corresponding HRTEM images, confirming the various shapes of the NCs observed in TEM image are tetrahedral projections.

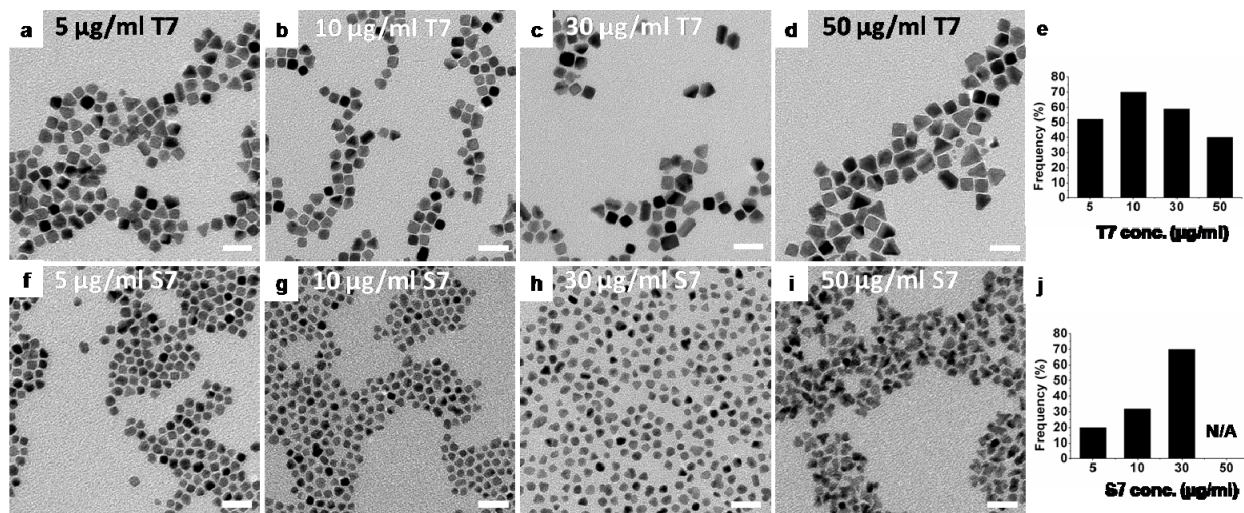


**Figure 3.10** TEM images of NCs as a function of T7 and S7 peptide concentration, respectively: 5 µl/ml of T7 (a); 10 µl/ml of T7 (b); 30 µl/ml of T7 (c); 50 µl/ml of T7 (d); 5 µl/ml of S7 (f); 10

$\mu\text{l/ml}$  of S7 (g); 30  $\mu\text{l/ml}$  of S7 (h); 50  $\mu\text{l/ml}$  of S7 (i). (e and j) are populations of Pt cubes and Pt tetrahedrons as a function of T7 and S7, respectively. Except for peptide concentration, the synthetic condition for the same peptide sequence is the same. Scale bars: 20 nm.

### **Peptide-directed shape transformation**

To demonstrate the exclusive binding selectivity of facet-specific peptides in shape control colloidal NCs synthesis, we performed a T7-S7 peptide switch reaction that can induce a shape transformation from cubes to tetrahedrons (Figure 3.11a). We prepared a reaction by injecting 0.8 mM of  $\text{NaBH}_4$  into a mixed solution containing 10  $\mu\text{g/ml}$  of T7, 1 mM ascorbic acid and 1 mM of  $\text{H}_2\text{PtCl}_6$ . The NCs obtained immediately after  $\text{NaBH}_4$  injection show near spherical truncated octahedron shape (Figure 3.11b), which can evolve into cubic NCs using T7 as the capping agent (Figure 3.11c, e-f), as expected from our discussion above. At 1 min of reaction time, 500  $\mu\text{l}$  of 1 mg/ml of S7 peptides were introduced into the T7-regulated reaction solution. Interestingly, after a few hours of reaction in the presence of a larger number of S7, we found that the shape of the NCs had transformed from predominantly cubes (69%) to tetrahedrons (57%) (Figure 3.11d, f-g). These results suggest that a larger number of S7 peptide can replace T7 and dominate the shape transformation from cubes to tetrahedrons. Since no obvious size increase is observed during the shape evolution process, we believe that the formation of the tetrahedron was attributed to the atom rearrangement on the NC surface induced by the interaction between the binding peptides and the surface atoms which eventually lead to the formation of NC shapes with lower surface energy facets, i.e., Pt (111).<sup>48-49</sup> In addition, we observed that the Pt tetrahedrons become richer to 57% in NC population, and that the remaining NCs are spherical like truncated octahedrons with both  $\{100\}$  and  $\{111\}$  facets, while few Pt cubes are left (Figure 3.11d and g). These results confirm the facet specificities of T7 and S7, and



their ability to modulate NC surface energies and guide the shape formation and transformation processes.

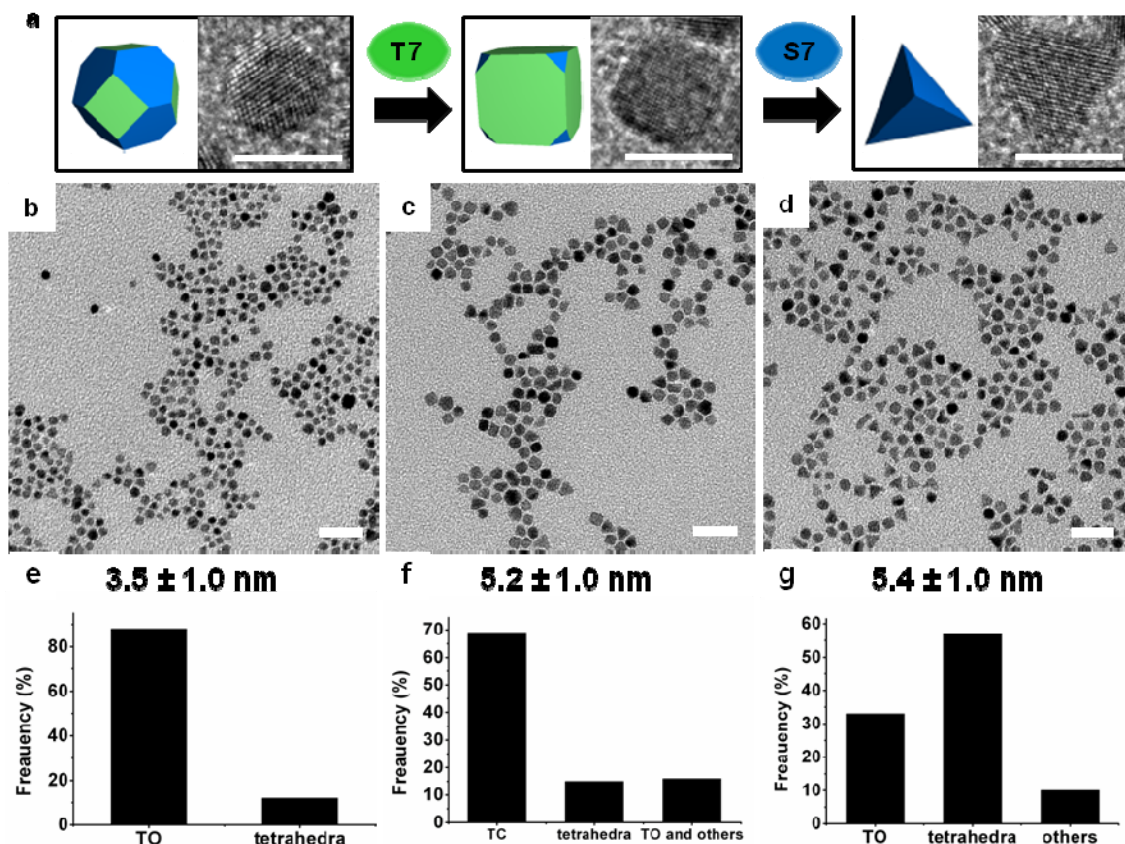


**Figure 3.11** NC shape transformation by predominantly replacing T7 with S7 in reaction. (a) Schematic illustration of the peptide switch leading to the shape change of NCs. Scale bars are 5 nm. (b) TEM image of the NCs obtained at 30 s from the reaction in the presence of T7. (c) TEM image of the NCs obtained at 1 min from T7 controlled reaction, showing cubic NCs. (d) TEM images showing the transformation from cube to tetrahedron after introducing S7 into the originally T7-regulated reaction. S7 was introduced at 1 min's reaction time and the images were taken at 5 hrs' reaction after introduction of S7. (e-g) The corresponding shape and size distributions of the NCs in b-d. The scale bars in b-d are 20 nm. TO: truncated octahedrons; TC: truncated cubes.

In summary, a rational approach to predictable control of NC structures using biomolecular specificities was demonstrated. Peptide sequences that recognize Pt- $\{100\}$  and Pt- $\{111\}$  planes have been rationally identified and used in directing the shape formation of Pt NCs in a colloidal NC synthetic conditions. The Pt- $\{100\}$  binding peptide (T7) and the Pt- $\{111\}$  binding peptide (S7) can effectively limit the growth rates along  $\langle 100 \rangle$  and  $\langle 111 \rangle$  and direct the synthesis of  $\{100\}$  and  $\{111\}$  facet enclosed NCs, respectively. More importantly, the shape-transformation of NCs from cube to tetrahedron is achieved by simply switching the binding peptide sequence from T7 to S7 in aqueous solution at room temperature, suggesting the possibility of post-growth dynamic control of material structures through biomolecules. This work is important in biomimetic synthesis and has inspired the mechanistic studies on the specific interfacial interactions between biomolecules and inorganic materials.

## **Chapter IV: FACET-SELECTIVE ADSORPTION ON NOBLE METAL CRYSTALS GUIDED BY ELECTROSTATIC POTENTIAL SURFACES OF AROMATIC MOLECULES**

Due to the discovery of the definitive binding pair of S7 peptide on Pt {111} facets, my group has continued the mechanistic study on the biomolecular recognition mechanism toward Pt {111} by experimental and computational studies.<sup>50</sup> We concluded that the presence of aromatic amino acid, phenylalanine (F), plays the dominant role in the selectivity binding affinity of S7 peptide on Pt {111}, contributing to the synthesis of Pt tetrahedrons. Interestingly, the computational results indicate that the molecular affinity to {111} surface (negative adsorption energy) and the disaffinity to {100} surface (positive adsorption energy) creates the binding contrast between these two surfaces, leading to the biomolecular recognition to (111) surface. The study on the origin of biorecognition towards Pt {111} demonstrate that the phenyl ring is predominant in guiding the binding selectivity to (111) surfaces, suggesting a potential ground to explore the fundamentals contributing to the molecular facet-selective adsorption and design strategies of organic molecules to control the organic-inorganic interface.

The interaction between aromatic molecules and various metal surfaces has been well studied in surface science, albeit in an environment different from practical syntheses, still providing a library of references to understand molecular selective adsorption in colloidal NCs.<sup>51-54</sup> Moreover, the variant substituent effect on aromatic molecules can be used to strategically tune their electronic properties and molecular structures, which are considered important parameters in binding mechanism.<sup>55-56</sup> Therefore, using aromatic molecules and noble metal surfaces as a platform we investigated the molecular facet selectivity and the organic-inorganic interface.<sup>57</sup> Our discoveries have been employed to achieve predictable shape control syntheses of NCs and enrich the knowledge in synthesis tools and related applications.

## A. Experimental methods

### NCs synthesis by aromatic molecules and characterization

Aromatic and other small molecules: phenol (99+%), catechol (99+%), resorcinol (99+), hydroquinone (99+), pyrogallol (99+%), hydroxyquinol (99%), phloroglucinol (99+%), *p*-nitrophenol (99+%), gallic acid (98+%), *p*-aminophenol (98+%), syringol (99%), *p*-quinone (98+%), squaric acid (99%) and terephthalic acid (98%) were purchased from Sigma-Aldrich. All chemicals were used as received without further purification.

Pt NCs synthesis method is described as following. All reagents used here are dissolved in water before use. 1 mM H<sub>2</sub>PtCl<sub>6</sub> and 15 µg/ml of aromatic molecules (60 µg/ml for syringol) were pre-mixed in a vial, and NaBH<sub>4</sub> aqueous solution with a final concentration of 1 mM (0.5 mM for phloroglucinol and gallic acid controlled synthesis) was injected in one shot. TEM samples were prepared after 30 minutes of reaction. The total volume of all reaction solutions is 5 ml. The concentrations indicated are all final concentration. In the reactions to generate Pt nanocubes with ascorbic acid and *p*-nitrophenol, 1 mM of H<sub>2</sub>PtCl<sub>6</sub> mixed with 0.5 mM of ascorbic acid and 12 µg/ml of aromatic molecules were injected with 2 mM NaBH<sub>4</sub>, reacting for 1 hour. In *p*-quinone controlled synthesis of Pt nanocubes, 50 µl of 50 mM NaBH<sub>4</sub> was injected into 1 mM of H<sub>2</sub>PtCl<sub>6</sub>, after 30 seconds, 20 µl of 2 mg/ml of *p*-quinone (final concentration 8 µg/ml) was introduced; the total reaction time is 1 hour. In squaric acid controlled reaction, 1 mM NaBH<sub>4</sub> was injected into 1 mM of H<sub>2</sub>PtCl<sub>6</sub> mixed with 0.5 mM of ascorbic acid and 8 µg/ml of squaric acid, reacting for 1 hour. All above mentioned reactions were conducted in ambient environment with stirring.

Pd NCs synthesis method is described as following. 3.5 ml DMF was first mixed with 0.375 ml water, 500 µl of 50 mM ascorbic acid in aqueous solution, and 3 mg of hydroquinone

(for Pd octahedra) or 12 mg of terephthalic acid (for Pd cubes). The mixed solution was heated at 80°C for 5 minutes and followed by an injection of 625  $\mu$ l of 20 mM Na<sub>2</sub>PdCl<sub>4</sub> aqueous solution. TEM samples of colloidal crystals were collected after one hour of reaction time.

TEM and Raman spectroscopy were used to characterize the obtained NCs and their organic-inorganic interactions. The morphologies of the synthesized NCs were imaged by a FEI CM 120 transmission electron microscopy (TEM) operated at 120 kV and FEI TITAN high resolution transmission electron microscopy (HRTEM), respectively. All TEM samples for imaging were prepared by pipetting the solution onto carbon-coated copper grids. TEM samples were dried in atmosphere before images were taken. The Raman spectra were measured on a Renishaw inVia spectrometer system equipped with an Argon Ion laser, 50 mW at 514 nm, air cooled as excitation source. The laser spot size is around 1  $\mu$ m. The spectral resolution was 4 cm<sup>-1</sup> at the excitation wavelength. In general, aromatic molecules controlled NCs were washed with water for two times by centrifuge (14000 rpm, 30 minutes per cycle) to remove excessive reagents. The collected NCs were incubated in 1 mg/ml of aromatic molecules in aqueous solution for 30 minutes and followed by centrifuge to remove excessive aromatic molecules. The final products of aromatic molecules on Pt NCs were re-dispersed in water and drop-casted on aluminum foil to form a thin film for Raman characterization. Particularly, to characterize the adsorption behavior of *p*-nitrophenol on Pt (111) surface, Pt tetrahedra were synthesized with phloroglucinol and washed five times by centrifuge to remove phloroglucinol. The collected Pt tetrahedra were then incubated with *p*-nitrophenol, centrifuged and re-dispersed in water for drop-casting.

### **Computation of molecular electrostatic potential surfaces and DFT calculation**

Electrostatic potential surfaces of organic molecules were computed by mapping electrostatic potential onto surfaces of molecular electron density (0.002 electrons/au<sup>3</sup>) and color-coding, using Hartree-Fock and 6-31G\* basis set to calculate equilibrium geometry at ground state by the program Spartan '06.<sup>58</sup> For all surfaces shown in this work, the potential energy values range from -80 kJ mol<sup>-1</sup> (red) to 80 kJ mol<sup>-1</sup> (blue). Red color represents a value equal to or greater than the maximum in negative potential, and blue corresponds to a value equal to or greater than the maximum in positive potential.

Density functional theory (DFT) calculations of energy levels of organic molecules and metal surfaces were performed with Vienna Ab initio Simulation Package (VASP) utilizing self-consistent to solve the Kohn-Sham one electron equations.<sup>59</sup> The wave function was expanded with a set of plane wave set whose cutoff energy is 700 eV. The Perdew-Burke Ernzerhof (PBE) flavor of general gradient approximation was employed describing the exchange and correlation of electrons.<sup>60</sup> The Brillouin Zone was sampled with 3×3×1 Monkhorst and Pack mesh.<sup>61</sup> The Pt and Pd surfaces were modeled employing a slab model containing 6 layers of metal atoms and a 4×4 supercell in each layer. An 11.9 Å thick vacuum layer was introduced to render the interaction between two metal layers. The top three layers are fully relaxed to simulate the surface while the bottom 3 layers are kept fixed to simulate the bulk utilizing the calculated equilibrium bulk lattice constant. The lattice constants of Pt and Pd are calculated to be 3.99 Å and 3.97 Å respectively, which are in agreement with the experimental value. As this formed an asymmetric model, the dipole correction was introduced to all the work function calculations. The isolated organic molecules are modeled in the 12Å×12Å×12Å supercell. Their HOMO and LUMO can be obtained from the calculation of their energy eigenvalues by VASP code. The

work function is calculated by subtracting Fermi level from the electrostatic potential within the vacuum layer, which represents the vacuum level.

## **B. Results and discussion**

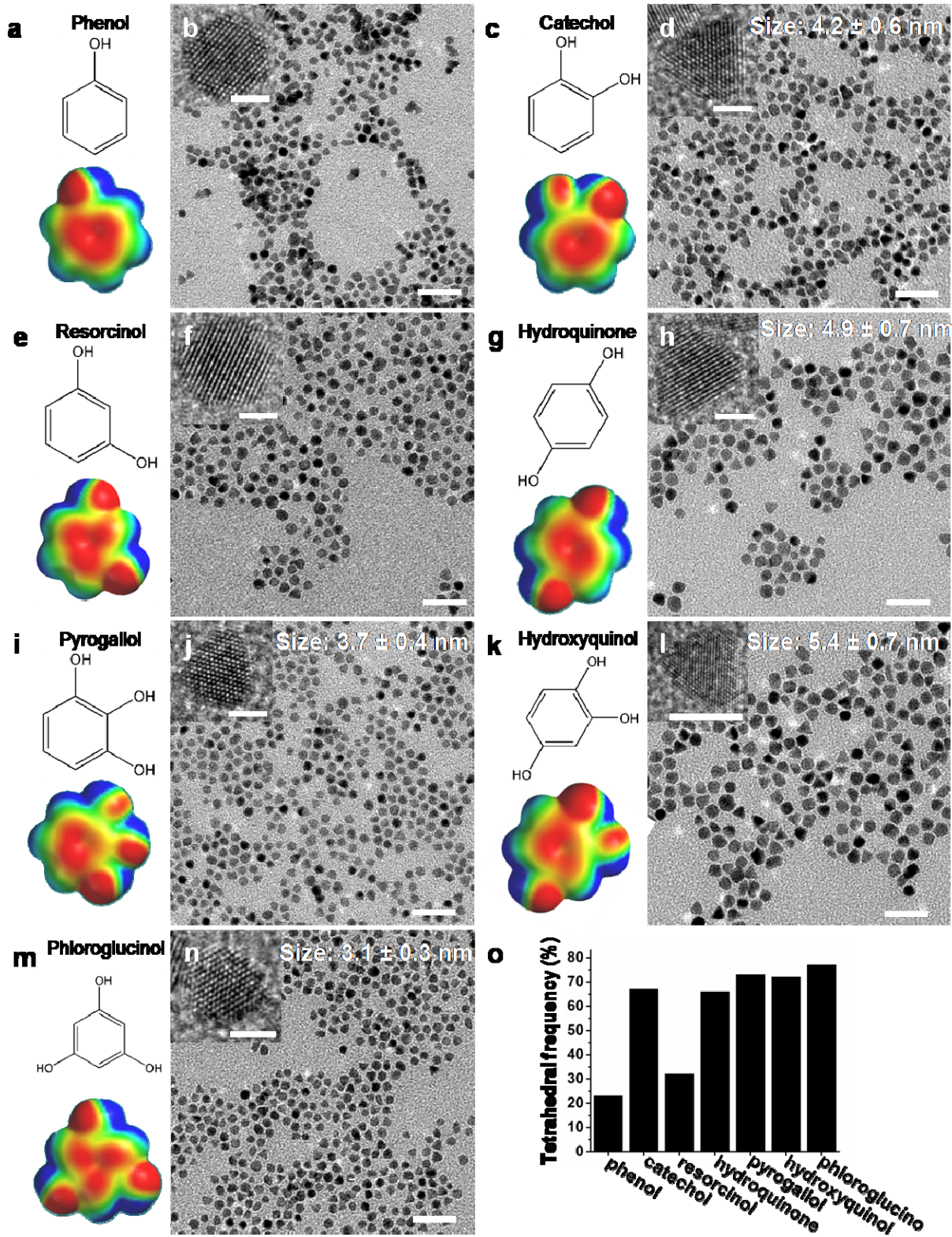
### **Pt NCs controlled by aromatic molecules**

At first, we studied the facet-selective adsorption of water-soluble phenolics which contain a benzene ring with one to three hydroxyl groups at different position. The binding selectivity of the phenolics to Pt {111} facets is reflected by the yield of Pt nano-tetrahedra from the phenolics controlled syntheses.<sup>50</sup> Their molecular structures and electrostatic potential surfaces are depicted in Figure 4.1a, c, e, g, i, k and m. The hydroxyl group with a  $\pi$  electron-donating property contributes to overall negative electrostatic potential on the aromatic ring. Except for phenol and resorcinol, the aromatic molecules discussed in Figure 4.1 can synthesize well-dispersed Pt nano-tetrahedra enclosed by {111} facets with high yield and different sizes as shown in Figure 4.1d, h, j, l, n and o, indicating their binding specificity to Pt {111} facets. The detailed shape distributions of the Pt NCs are listed in Table 4.1. Catechol with two hydroxyl groups at an *ortho* site can synthesize 67 % of Pt tetrahedra with an average size of  $4.2 \pm 0.6$  nm (Figure 4.1c-d and o). Hydroquinone with two hydroxyl groups at a *para* site yields 66 % of Pt tetrahedra with an average size of  $4.9 \pm 0.7$  nm (Figure 4.1g-h and o). Pyrogallol, hydroxyquinol and phloroglucinol with three hydroxyl groups bonded to a benzene ring generate Pt nanocrystals with 73 %, 72% and 77 % of tetrahedra and average sizes of  $3.7 \pm 0.4$  nm,  $5.4 \pm 0.7$  and  $3.1 \pm 0.3$  nm, respectively (Figure 4.1i-o). The insets in Figure 4.1d, h, j, l and n represent the corresponding HRTEM images of different sized Pt nano-tetrahedra, showing a typical triangular projection of a tetrahedron. In principle, we distinguish tetrahedrons from others by differentiating the triangular and diamond-like from spherical shape of the projection of NCs (see

Figure 4.2). With the exception of resorcinol, the yield of Pt nano-tetrahedra increases with the number of hydroxyl groups on the benzene ring, indicating the interaction between the aromatic molecules and Pt {111} surface is enhanced by hydroxyl substitutions (Figure 4.1o). We believe that the position and number of hydroxyl substitution in aromatic ring could affect the binding strength of molecules on Pt {111}, and consequently change the yield of tetrahedral Pt NCs. It is worthy to note that under different synthetic conditions with different Pt precursor, we can synthesize larger Pt NCs and have observed similar phenomena, further confirming the role of these aromatic molecules in shaping NCs as well as their facet binding selectivity (Figure 4.3).

It is believed that benzene adsorbs on Pt (111) at the bridge (30) position, wherein C  $p_z$  orbitals overlapping with the metal  $d_z^2$  and  $d_{yz}$  orbitals lead to the formation of Pt-C bonds.<sup>51-52</sup> This interaction is explained by electron donation from the molecular  $\pi$  orbitals of benzene to the surface d-band of Pt and back-donation from the surface to the molecular  $\pi^*$  orbitals of benzene.<sup>53-54</sup> Their interaction depends on the ability of the metal to act as an acceptor, which in turn depends on the work function of the metal.<sup>62</sup> Aromatic molecules with hydroxyl groups as substituent showing higher highest occupied molecular orbital ( $\epsilon_{\text{HOMO}}$ ) levels than benzene can act as electron donors.<sup>63</sup> Compare the work function of Pt (111) and Pt (100), Pt (111) has a higher work function and therefore is a more effective acceptor, which facilitates better electron donation from the aromatic molecule, leading to a stronger interaction between the surface d states and the delocalized  $\pi$  electrons of phenolics.<sup>64-65</sup> These contribute to the binding selectivity of phenolics to Pt {111} facets, accounting for the production of Pt nano-tetrahedra. Hydroxyl substitution can enhance the  $\pi$  donating tendency of the host aromatic ring and thus enhance the interaction strength between the phenolics and Pt {111} facets, resulting in the increase of tetrahedral yield with number of hydroxyl groups.<sup>66</sup>

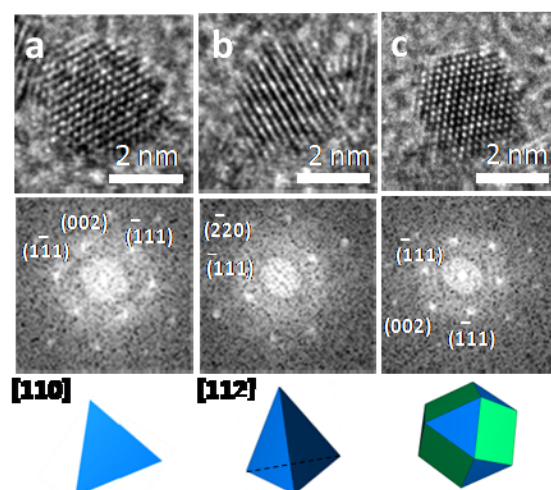




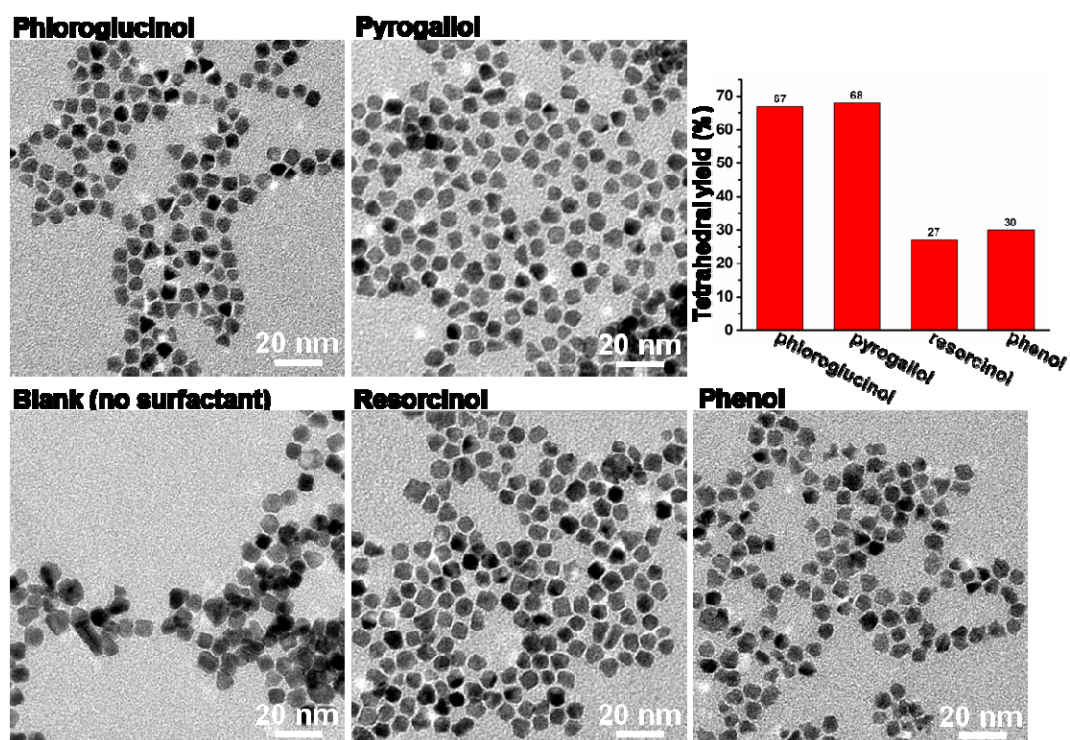
**Figure 4.1** Pt NCs controlled with a variety of phenolics. (a, c, e, g, i, k, m) Molecular structures and electrostatic potential surfaces of (a) phenol, (c) catechol, (e) resorcinol, (g) hydroquinone, (i) pyrogallol, (k) hydroxyquinol and (m) phloroglucinol. (b, d, f, h, j, l, n) Corresponding TEM images of the obtained Pt NCs by phenolics and HRTEM images (in inset) of representative Pt cuboctahedra and tetrahedra in the syntheses. (o) Tetrahedral frequencies of Pt NCs synthesized by different phenolics. Scale bars: 20 nm in b, d, f, h, j, l and n; 2 nm in inset of b, d, f, h, j and n; 5 nm in inset of l. Electrostatic potential: [-80 kJ mol<sup>-1</sup> (red) to +80 kJ mol<sup>-1</sup> (blue)].

**Table 4.1** Shape distributions of the obtained Pt NCs controlled by different aromatic molecules in Figure 4.1 and Figure 4.6.

	Tetrahedral frequency /%	Cuboctahedral frequency /%	Irregular shape frequency /%	pK <sub>a</sub>
<b>Phenol</b>	<b>23</b>	<b>66</b>	<b>11</b>	<b>10<sup>67</sup></b>
<b>Catechol</b>	<b>67</b>	<b>28</b>	<b>5</b>	<b>9.5<sup>67</sup></b>
<b>Resorcinol</b>	<b>35</b>	<b>56</b>	<b>9</b>	<b>9.4<sup>67</sup></b>
<b>Hydroquinone</b>	<b>66</b>	<b>28</b>	<b>6</b>	<b>10<sup>67</sup></b>
<b>Pyrogallol</b>	<b>73</b>	<b>24</b>	<b>3</b>	<b>10<sup>66</sup></b>
<b>Hydroxyquinol</b>	<b>72</b>	<b>22</b>	<b>6</b>	<b>N/A</b>
<b>Phloroglucinol</b>	<b>77</b>	<b>17</b>	<b>6</b>	<b>9<sup>68</sup></b>
<b><i>p</i>-nitrophenol</b>	<b>4</b>	<b>N/A</b>	<b>N/A</b>	<b>7.1 (phenol with <i>para</i> substituted NO<sub>2</sub>)<sup>67</sup></b>
<b>Gallic acid</b>	<b>42</b>	<b>56</b>	<b>2</b>	<b>4.4<sup>69</sup></b>
<b><i>p</i>-aminophenol</b>	<b>28</b>	<b>64</b>	<b>8</b>	<b>10.3 (phenol with <i>para</i> substituted NH<sub>2</sub>) 5.5 (aniline with <i>para</i> substituted OH)<sup>67</sup></b>
<b><i>p</i>-aminophenol in acid (pH 4)</b>	<b>63</b>	<b>27</b>	<b>10</b>	<b>N/A</b>
<b>Syringol</b>	<b>72</b>	<b>19</b>	<b>9</b>	<b>10<sup>70</sup></b>



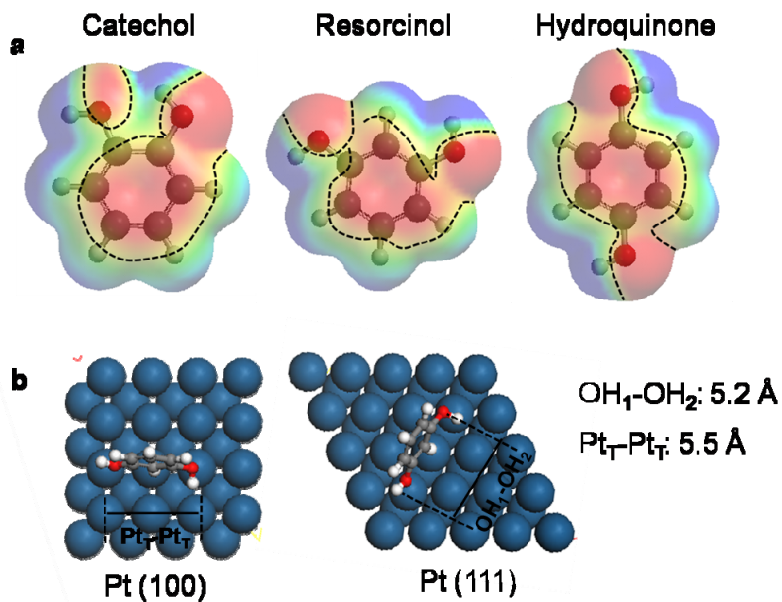
**Figure 4.2** HRTEM images, the corresponding FT patterns and geometrical models of (a) a Pt tetrahedron imaged along [110] showing triangular projection, (b) a Pt tetrahedron imaged along [112] showing diamond-like projection and (c) a Pt cuboctahedron showing spherical projection.



**Figure 4.3** TEM images of Pt NCs controlled with and without aromatic molecules. 1 mM  $K_2PtCl_4$  mixed with 0.5 mM ascorbic acid and 15  $\mu\text{g/ml}$  aromatic molecules were injected with

0.5 mM NaBH<sub>4</sub>, reacting for 2 hour. The total volume of all reaction solutions is 5 ml. The concentrations indicated are all final concentration.

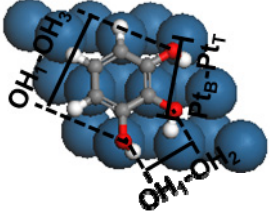
The position of the hydroxyl substituent can change the  $\pi$  electron distribution in the ring region and hence may also play a role in the facet selectivity. Comparing the electrostatic potential surfaces of catechol, resorcinol and hydroquinone (Figure 4.1c, e and g), we see that the red region in the ring of resorcinol is relatively asymmetric, while those of catechol and hydroquinone are symmetric (as depicted in Figure 4.4a). This difference may cease resorcinol binding on metal surfaces through its ring, while the two hydroxyl groups are more likely to contribute to binding. We found that the hydroxyl groups can be well-located on top of Pt atoms on (111) or (100) lattice with little lattice mismatching (Figure 4.4b). These may attribute to the loss of binding selectivity of resorcinol to Pt (111), resulting in the low yield of Pt tetrahedra synthesized by resorcinol. In addition to benzene ring, active functional groups, such as hydroxyl and amine groups, can act as binding sites on metal surfaces, pointing out the importance of the geometric relationship between the positions of hydroxyl groups and lattice of Pt (111).<sup>71-72</sup> By locating the benzene ring on the bridge (30) position (considered as the most stable configuration),<sup>51-52</sup> the hydroxyl groups of hydroquinone, pyrogallol and phloroglucinol were coordinated with atoms on Pt (111) lattice (Table 4.2). Interestingly, the hydroxyl groups can be well located on the preferential binding sites (top or bridge) on the Pt (111) surface with little lattice mismatch. This can account for the observation that the increased number of hydroxyl groups can contribute to increased interaction between phenolics and Pt (111) surface. Therefore, phenolics with negative electrostatic potential on the ring system display binding selectivity to Pt {111} facets, while the position and number of hydroxyl substituents can influence their facet selectivity and binding strength.



**Figure 4.4** (a) Depiction of the shape of the red (negative) region of electrostatic potential surfaces of catechol, resorcinol and hydroquinone. (b) The geometric matching of the hydroxyl groups of resorcinol on Pt (100) and Pt (111) lattice.

**Table 4.2** Geometric matching of phenolics on Pt (111) surface

	Configuration on Pt (111)	Epitaxial relation
<b>Hydroquinone</b> Ring: Bridge(30) 2 OH: Top		$Pt_T-Pt_T(1): 4.8 \text{ \AA}$ $OH_1-OH_4: 6.0 \text{ \AA}$
<b>Phloroglucinol</b> Ring: Bridge(30) 3 OH: Top		$Pt_T-Pt_T(2): 5.5 \text{ \AA}$ $OH_1-OH_3: 5.3 \text{ \AA}$

<p><b>Pyrogallol</b>  Ring: Bridge(30)  2 OH: Top  1 OH: Bridge</p>		<p><b>Pt<sub>T</sub>-Pt<sub>T</sub> (2): 5.5 Å</b>  <b>OH<sub>1</sub>-OH<sub>3</sub>: 5.0 Å</b>  <b>Pt<sub>B</sub>-Pt<sub>T</sub>: 3.1 Å</b>  <b>OH<sub>1</sub>-OH<sub>2</sub>: 2.8 Å</b></p>
---	---	---

It is known that the phenolics with hydroxyl substituent can be used as reducing agents, and their redox potential related to the substituent position decreases in the order of *meta*-, *ortho*- and *para*- substitution.<sup>73</sup> However, we believe most phenolics adsorbing on Pt surfaces are stable and stay in the reduced form due to the reducing environment provided. This is supported by the UV-vis spectra of hydroquinone, *p*-quinone and hydroquinone -Pt nanocrystals solution (Figure 4.5). We showed that hydroquinone did not oxidize to *p*-quinone (appearance of absorption at 244 nm) in the NCs synthesis solution until higher concentration of hydroquinone and long reaction time is performed,<sup>74</sup> suggesting that only the excessive hydroquinone not bound on Pt surface will oxidize. Interestingly, we found the reducing power of phenolics used here increases in the order of phloroglucinol, pyrogallol, catechol, hydroquinone and hydroxyquinone, which agrees with the increase in the size of Pt tetrahedra controlled by them (Figure 4.1d, h, j, l and n). We think that these phenolics might be able to facilitate the Pt ion reduction and the crystal growth, in which they can get oxidized and lost binding affinity but instantly recovered the externally added reducing agent (i.e., NaBH<sub>4</sub>). Phenolics solely cannot reduce Pt(IV) ions to generate Pt NCs without introducing NaBH<sub>4</sub> in syntheses. However, more investigation is needed to elucidate the size variation of the Pt NCs synthesized by different aromatic molecules.

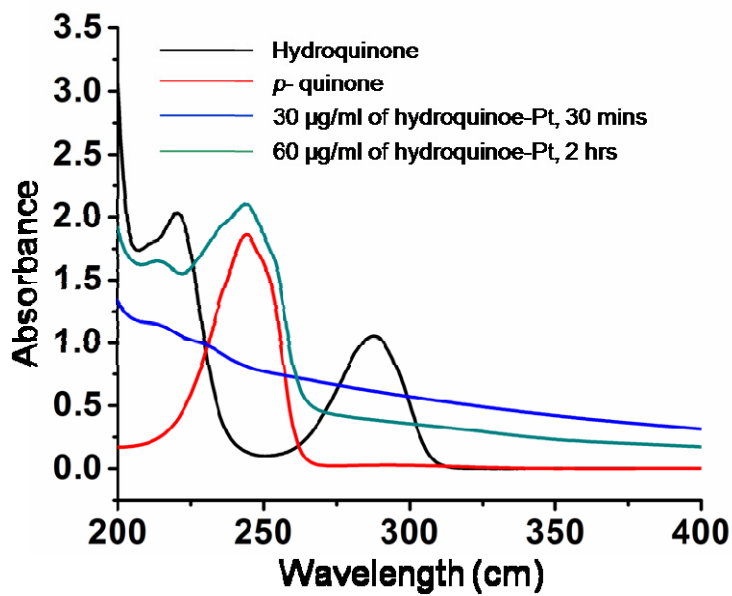


**Figure 4.5** UV-vis adsorption of hydroquinone, *p*-quinone and hydroquinone-Pt NCs solutions (Blue: 30 µg/ml of hydroquinone-synthesized Pt NCs solution reacting for 30 minutes; green: 60 µg/ml of hydroquinone-synthesized Pt NCs solution reacting for more than 2 hours). The spectrum of 30 µg/ml of hydroquinone-Pt, 30 mins (the reaction condition is similar to Pt tetrahedra synthesis) showing no characteristic peak of *p*-quinone indicates that hydroquinone did not oxidized to *p*-quinone in the reaction. However, as shown in the spectrum of 60 µg/ml of hydroquinone –Pt, 2 hrs, hydroquinone oxidized and formed *p*-quinone as higher concentration and long reaction time is performed, indicating that excessive hydroquinone which did not bind on metal surface would oxidize. The UV-vis adsorption was conducted by DU800 UV-vis spectrometer.

Various function groups can change the electronic properties of aromatic molecules in a different manner, e.g., amino group is strong electron donor and nitro group is withdrawer. These groups will alter the electrostatic potential on the benzene ring and contribute to binding effect on Pt surface. As shown in Figure 4.6 a and c, *p*-nitrophenol and gallic acid substituted with  $\pi$

electron-withdrawing nitro and carboxyl group, respectively show less negative to neutral electrostatic potential on the aromatic ring relative to those shown in Figure 4.1. We observed that *p*-nitrophenol showing almost neutral electrostatic potential on the ring (ranging from -10 to 0 kJ mol<sup>-1</sup>) generates aggregated Pt NCs without well-defined shapes (Figure 4.6a and b). However, gallic acid showing negative electrostatic potential on the ring (ranging from -50 to -10 kJ mol<sup>-1</sup>) yields Pt NCs with 42% of tetrahedra and 56% of cuboctahedra (Figure 4.6c-d, k and Table 4.1). Obviously, as the electrostatic potential on the ring changes from neutral (*p*-nitrophenol) to negative (gallic acid), the yield of Pt tetrahedra increases accordingly from 4% to 42%, demonstrating that the molecular electrostatic potential surfaces can be used to guide the molecular binding selectivity to Pt {111} facets (Figure 4.6a, c and k). Nevertheless, in comparison with Figure 4.1, the aromatic molecules substituted with  $\pi$  electron-withdrawing group and showing less negative to neutral electrostatic potential on the ring produce a relative low yield of Pt tetrahedra, indicating weaker Pt {111} facet specificity. Amine and methoxyl groups known as electron donors can induce negative electrostatic potential on the ring of the aromatic molecules substituted with them. According to the above discussion, *p*-aminophenol and syringol shown in Figure 4.6e and g are promising to show binding selectivity to Pt {111} facet and synthesize Pt tetrahedra. However, it is worth noting that the different function groups (amine, methoxyl and hydroxyl) on the benzene ring can alter the molecular adsorption behavior on Pt surface. The amine group in *p*-aminophenol is more active than hydroxyl group when interacting with Pt and tend to stand up the whole molecule, resulting in the loss of binding selectivity to Pt {111} facet and a low yield of Pt tetrahedra (28%) as shown in Figure 4.6f and k.<sup>72,75</sup> However, the amine group can be deactivated in acidic solution. By doing so, we believe it can interact with the metal surface through the aromatic ring as shown in Figure 4.6i.<sup>72</sup> This is



supporting by the experimental result that tuning the pH of reaction solution from 6 to 4, 63% of Pt nano-tetrahedra can be obtained from the reaction in the presence of *p*-aminophenol (pH=4), which is compared to the 28% at pH=6 (Figure 4.6f, j and k). Since the amine group of *p*-aminophenol is less active in acidic solution, its aromatic ring with negative electrostatic potential predominantly contributes to the molecular binding effect and selectivity on Pt (111) surface. In terms of syringol, the methoxyl group consisting of a methyl group bound to oxygen is bulkier than the hydroxyl group, so its steric effect on binding to Pt {111} is expected (Figure 4.6g).<sup>72</sup> While substituted with two methoxyl groups and one hydroxyl group, syringol is like pyrogallol in terms of the electrostatic potential on the ring and the position of the three  $\pi$  electron donors (Figure 4.6g), indicating the two aromatic molecules may share similar facet binding selectivity to Pt (111).<sup>73</sup> Due to the steric effect of methoxyl group, a comparable yield of Pt nano-tetrahedra (72%) can be achieved by introducing a higher concentration of syringol (60  $\mu\text{g/ml}$ ; pyrogallol: 15  $\mu\text{g/ml}$ ) in the NCs synthesis (Figure 4.6h, k and Table 4.1), suggesting syringol has Pt {111} facet binding specificity as guided by its electrostatic potential. To put together, the negative electrostatic potential on the ring acts as the prerequisite to determine the Pt {111} facet specificity of aromatic molecules, although the different substituent-metal surface interaction may alter the molecular binding behavior. The pH of all reactions, 5~6, was lower than the  $\text{pK}_a$  of the aromatic molecules, indicating the molecules used in reactions might not be highly charged and primarily stay in their neutral forms (Table 4.1).

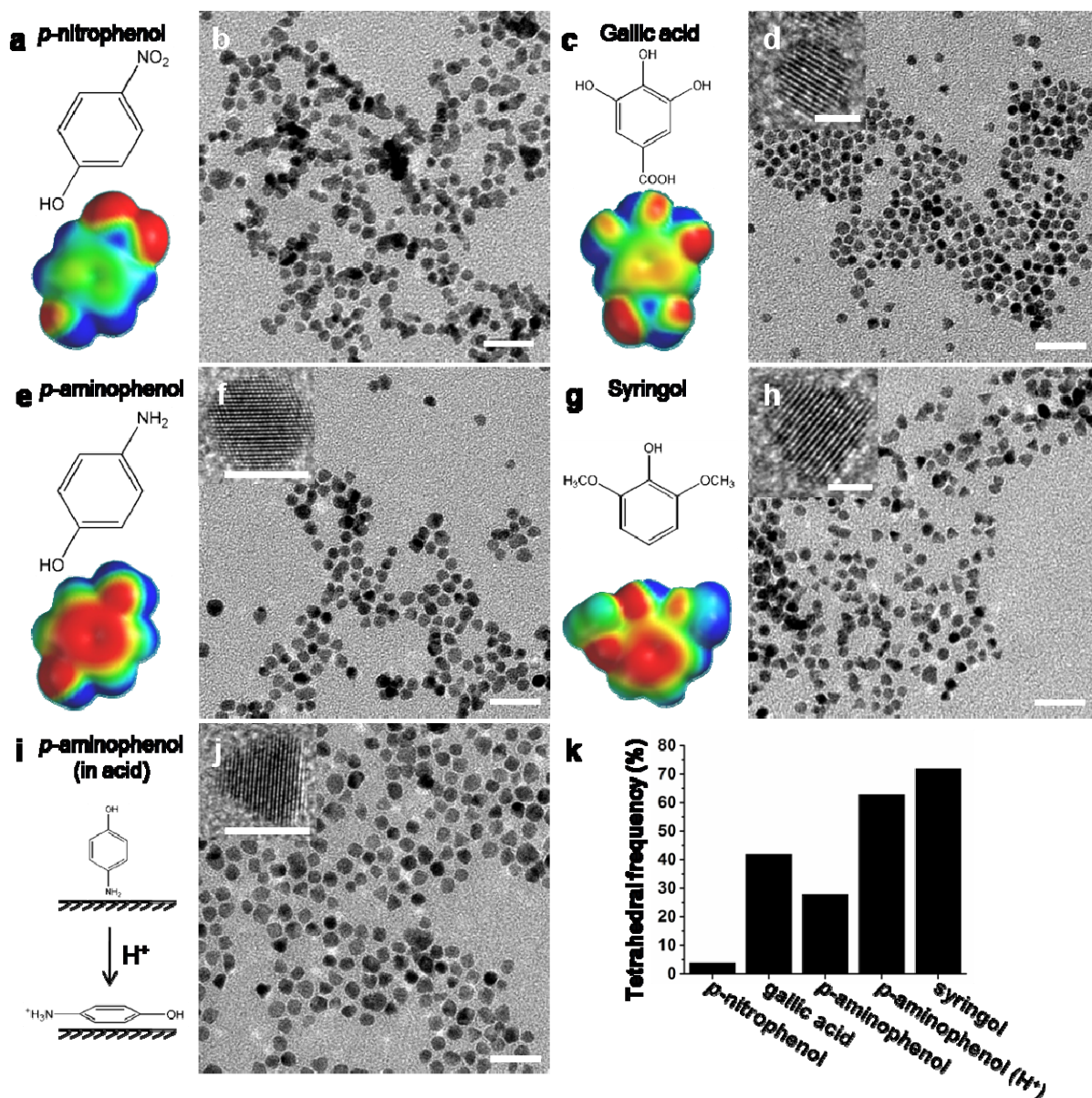


**Figure 4.6** Pt NCs controlled by phenolic molecules substituted with nitro, carboxyl, amine and methoxy group, respectively. (a, c, e, g) Molecular structure and electrostatic potential surface of (a) *p*-nitrophenol, (c) gallic acid, (e) *p*-aminophenol and (g) syringol. (b, d, f, h) are the corresponding TEM images of the obtained Pt NCs controlled with the particular molecule. (i) Schematic illustration of switching the adsorption behavior of *p*-aminophenol by inactivating amine group with acid. (j) TEM image of Pt NCs controlled by *p*-aminophenol in acidic solution

(pH 4). Insets in d, f, h and j are the corresponding HRTEM images of the representative Pt cuboctahedra and tetrahedra. (k) Tetrahedral frequencies of Pt NCs controlled with different aromatic molecules. Scale bars: 20 nm in b, d, f, h and j; 2 nm in insets of d and h; 5 nm in insets of f and j. Electrostatic potential: [-80 kJ mol<sup>-1</sup> (red) to +80 kJ mol<sup>-1</sup> (blue)].

### **Binding mechanism of aromatic molecules on metal surfaces**

Raman spectroscopy was used to characterize the adsorption of aromatic molecules on different Pt surfaces to provide direct evidence of the molecular binding configuration and mechanism, suggesting directions to discover more facet-specific surfactants. As shown in Figure 4.7, the Raman spectra of free hydroquinone molecules and hydroquinone on Pt nanotetrahedra [hydroquinone-Pt (111)] differ noticeably. The assignment of the peaks observed in the Raman spectra to the vibrational modes of hydroquinone is shown in Table 4.3.<sup>76</sup> The C-H stretch mode of hydroquinone at 3070 cm<sup>-1</sup> (with a shoulder at 3026 cm<sup>-1</sup>) shows a red shift of 91-135 cm<sup>-1</sup> after binding to Pt (111) surface. C-C ring stretch modes at 1611 cm<sup>-1</sup> (with a shoulder at 1630 cm<sup>-1</sup>) and 847 cm<sup>-1</sup> also have an obvious red shift of 30-11 cm<sup>-1</sup> and 24 cm<sup>-1</sup>, respectively, upon adsorption. These two significant red shifts are similar to the observations for parallel-chemisorbed benzene on Pt (111) surface, confirming that the hydroquinone interacts with the Pt (111) surface via the  $\pi$  electron of the benzene ring with a flat orientation to the surface.<sup>77-78</sup> It is worth noting that the peak at 1268 cm<sup>-1</sup> attributed to the C-O stretch mode of hydroquinone shifts to 1313 cm<sup>-1</sup> upon adsorption, indicating that the hydroxyl groups also interact with the Pt metal surface.<sup>77</sup> In addition, the disappearance of the O-H in-plane-bending peaks at 1240 and 1227 cm<sup>-1</sup>, as well as the peak found at 545 cm<sup>-1</sup> attributed to the Pt-O bond in the spectrum of hydroquinone-Pt (111), strongly supporting that hydroxyl groups contribute to the binding of hydroquinone on Pt (111).<sup>75</sup> The red shift and intensive enhancement of the C-C

ring stretch might infer a selective enhancement resulting from the charge transfer enhanced effect, surface enhanced Raman scattering (SERS) (Figure 4.7).<sup>77,79</sup> Therefore, the configuration of hydroquinone on Pt (111) as we proposed in the geometric matching models is evident by the Raman characterization, indicating that hydroquinone interacts with Pt (111) with a flat aromatic ring on the surface and bonds via hydroxyl groups.

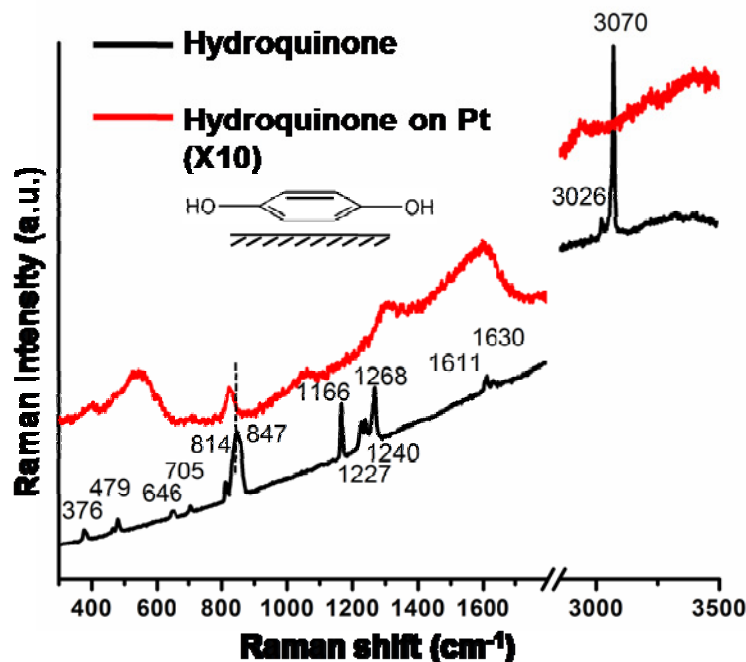


**Figure 4.7** Raman spectra of free hydroquinone (black line) and hydroquinone on Pt tetrahedra [111] faceted] (red line).

**Table 4.3** Assignment of the vibrational modes of Raman peaks for hydroquinone

Free hydroquinone	Hydroquinone on Pt (111)	Assignment
3070	2935	C-H stretch
3026		
1630	1600	C-C ring stretch
1611		
1268	1313	C-O stretch
1240		O-H in plane bend
1227		

1166	1063	C-C-H in plane bend
847	823	C-C ring stretch
814	781	C-H out of plane deformation
705		Ring torsion
646		C-C-C bend
	545	Pt-O/ Pt-C
479	466	C-C-C bend
376	404	C-O out of plane deformation

The configuration of standing-up *p*-aminophenol on Pt surfaces was also demonstrated by the Raman spectra of free *p*-aminophenol molecules and *p*-aminophenol on the as-synthesized Pt NCs (Figure 4.8); the assignment of peaks is given in Table 4.4.<sup>80</sup> An intensive peak at 3071 cm<sup>-1</sup> attributed to C-H stretch mode of *p*-aminophenol shows a slight red shift to 3077 cm<sup>-1</sup> upon adsorption, as well as the C-H in-plane-bending vibration, suggesting the interaction between the aromatic ring and Pt surface is weak. Another significant feature of the Raman spectra is the peak at 843 cm<sup>-1</sup> attributed to the C-C ring stretch mode of *p*-aminophenol, which disappears upon adsorption, suggesting a vertical orientation of the ring to Pt surface.<sup>78</sup> As we discussed above, the active amine group interacts with the Pt surface stronger than the phenyl ring and hydroxyl group, leading to a vertical configuration of *p*-aminophenol binding on the Pt surface via amine group. We confirm this binding configuration due to the observation of the large shift of NH<sub>2</sub> wag mode from 703 cm<sup>-1</sup> to 767 cm<sup>-1</sup>. However, *p*-aminophenol binding on the Pt surface though the aromatic ring still contributes to part of whole binding behavior since relative shifts of the peaks from the C-C ring stretch modes ranging from 1617 to 1317 cm<sup>-1</sup> upon adsorption are observed. Overall, a lack of strong interaction between the aromatic ring and Pt surface results in the loss of binding selectivity of *p*-aminophenol to the Pt (111) surface, consequently contributing to the low yield of Pt tetrahedra controlled by *p*-aminophenol as shown previously.

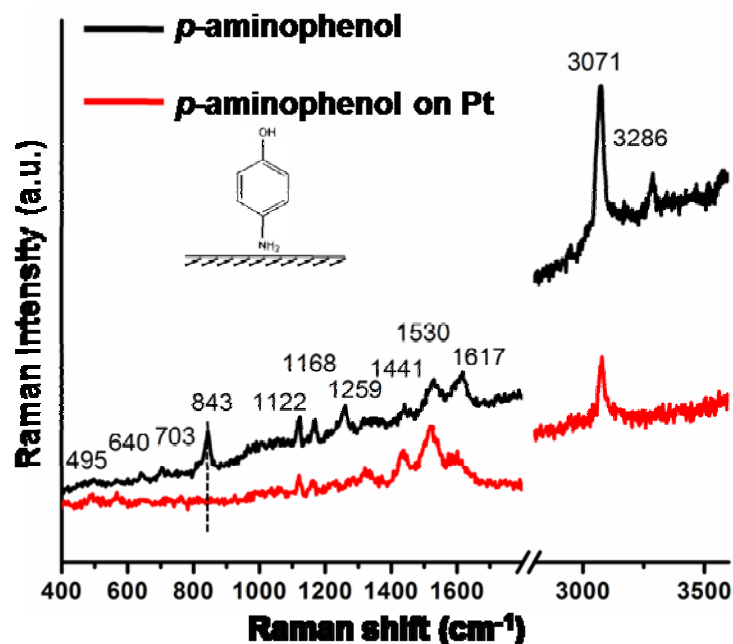


**Figure 4.8** Raman spectra of free *p*-aminophenol (black line) and *p*-aminophenol on Pt nanocrystals (red line).

**Table 4.4** Assignment of the vibrational modes of Raman peaks for *p*-aminophenol

Free <i>p</i> -aminophenol	<i>p</i> -aminophenol on Pt NCs	Assignment
3286		O-H stretch
3071	3077	C-H stretch
1617	1603	C-C ring stretch
1530		
1441		
1259		
1317		
1168	1164	C-H in plane bend
1122		
843		C-C ring stretch
703	761	NH <sub>2</sub> wag
640		C-C out of plane ring deformation
	566	Pt-O/ Pt-N
495	490	C-NH <sub>2</sub> out of plane bend

From the previous observation, we know *p*-nitrophenol failed to show binding affinity to Pt (111) and to synthesize well-dispersed NCs in solution. Surprisingly, through introducing a mild reducing agent ascorbic acid to enhance the crystal growth, Pt NCs controlled with *p*-nitrophenol can grow 66% of cubes enclosed by {100} facets with an average size of  $7.3 \pm 0.9$  nm, suggesting *p*-nitrophenol, to some extent, has binding selectivity to Pt {100} facets (Figure 4.9a-b). Comparing the electrostatic potential of the phenolics in Figure 4.1 and Figure 4.6, *p*-nitrophenol has almost neutral potential on the ring, which could be an important guidance to select Pt {100} facet-specific molecules. To study the facet adsorption behavior of *p*-nitrophenol on Pt surfaces, we used Raman spectroscopy to characterize free *p*-nitrophenol molecules, *p*-nitrophenol on Pt nano-tetrahedra ({111} faceted) and *p*-nitrophenol on Pt nanocubes ({100} faceted), respectively, as shown in Figure 4.9c. The three spectra show similar characteristic peaks while some of them vary obviously in frequency, indicating they display different adsorption behavior on Pt (111) and Pt (100) surface. The assignment of the characteristic peaks of the spectra is listed in Table 4.5. First, the peak at  $1589\text{ cm}^{-1}$  attributing to C-C ring stretch mode has a blue shift to  $1597\text{ cm}^{-1}$  upon adsorption on Pt (111) while nearly no shift for Pt (100).<sup>81</sup> It is reported that tilted chemisorbed benzene interacting with metal surface may show a small blue shift in the ring breath vibration, suggesting *p*-nitrophenol might have a tilted ring orientation to Pt (111).<sup>78</sup> Secondly, the NO<sub>2</sub> relevant vibration modes including symmetric NO<sub>2</sub> stretching at  $1328\text{ cm}^{-1}$  and NO<sub>2</sub> bending at  $866$  and  $814\text{ cm}^{-1}$  show more significant shift upon adsorption on Pt (111) than on Pt (100), indicating nitro group interacts more strongly with Pt (111).<sup>77</sup> Moreover, the significant red shift of C-O stretching mode at  $1291\text{ cm}^{-1}$  and appearance of a shoulder peak at  $1233$  and  $1236\text{ cm}^{-1}$  on Pt (111) and Pt (100) are observed, respectively, indicating the interaction between hydroxyl group and Pt surfaces.<sup>79</sup> These results conclude that

*p*-nitrophenol adopts a tilted configuration on Pt (111) through the end group of either OH or NO<sub>2</sub>. It also confirms the lack of direct interaction between aromatic ring and Pt (111), leading to the loss of the molecular binding selectivity to Pt (111). In the case of *p*-nitrophenol on Pt (100), in addition to C-C ring stretch mode, the other ring associated characteristic peaks (i.e., C-H in plane bending at 1504 and 1109 cm<sup>-1</sup>, and C-C-C bending at 635 cm<sup>-1</sup>) show small or almost no shift, indicating the lack of interaction between the ring and the metal surface. We suggest that both groups (OH and NO<sub>2</sub>) interact with Pt (100) at the same time by observing the relative shift of their vibration modes (e.g., NO<sub>2</sub> stretch, C-O stretch and NO<sub>2</sub> bending). We believe *p*-nitrophenol's interaction with Pt (100) surface is not through the ring since it is  $\pi$  electron deficient relative to those Pt {111} facet-specific molecules, and the corresponding Raman spectrum showed a similar ring vibration frequency as that found in free *p*-nitrophenol molecules. Therefore, the hydroxyl and nitro group of *p*-nitrophenol might predominantly contribute to the Pt (100) binding specificity. By matching its molecular structure to Pt (100) lattice, we can well locate benzene ring at 4-fold hollow site, two oxygens of nitro group on top of Pt atoms and hydroxyl group on hollow site with little lattice mismatch (Table 4.6). This suggests the geometric matching relationship between molecular binding sites and Pt (100) lattice is important in determining (100) facet-specific surfactants.



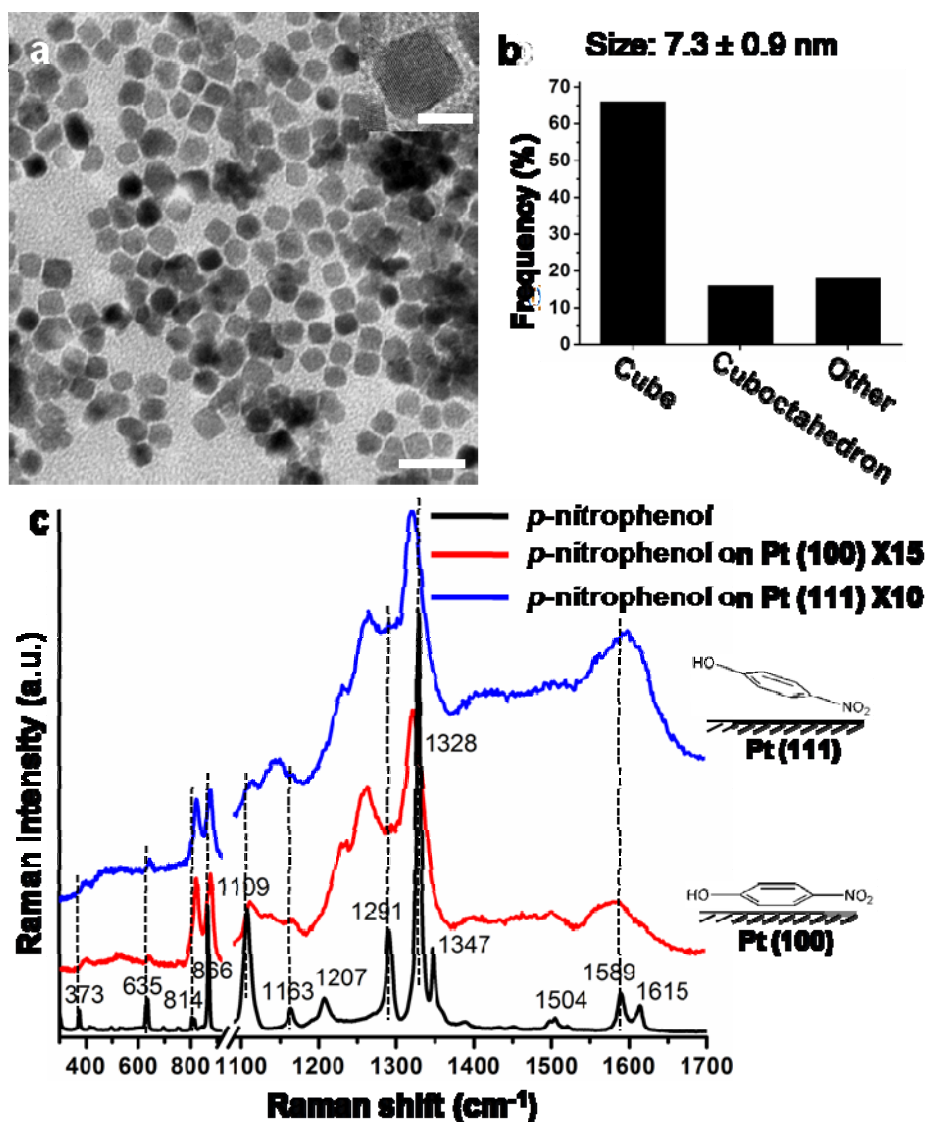


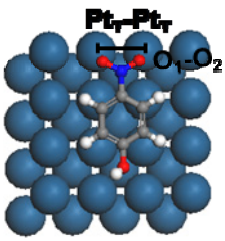
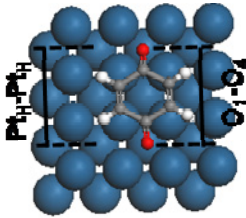
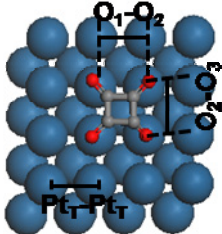
**Figure 4.9** (a) TEM image of *p*-nitrophenol controlled synthesis of Pt nanocubes. (b) The corresponding size and shape distribution. (c) Raman spectra of free *p*-nitrophenol (dark line), and *p*-nitrophenol on Pt nanocubes [(100) faceted] (red line) and Pt nano-tetrahedra [(111) faceted] (blue line), respectively. Scale bars: 20 nm in a; 5 nm in inset.

**Table 4.5** Assignment of the vibrational modes of Raman peaks for *p*-nitrophenol

Free <i>p</i> -nitrophenol	<i>p</i> -nitrophenol on Pt (100)	<i>p</i> -nitrophenol on Pt (111)	Assignment
1615	1588	1597	C-C ring stretch
1589			

1504	1500		C-H in plane bend
1347			C-C ring stretch
1328	1324	1320	Sym NO <sub>2</sub> stretch
1291	1262	1264	O-C stretch
	1236	1233	
1207			C-H in plane bend
1163	1167	1150	C-O-H bend
1109	1112	1115	C-H in plane bend
866	877	878	NO <sub>2</sub> bend
814			
635	636	643	C-C-C bend
	517	532	Pt-O / Pt-N
373	400	401	O-C torsion

**Table 4.6** Geometric matching of organic molecules on Pt (100) surface

	<b>Configuration on Pt (100)</b>	<b>Epitaxial relation</b>
<p><b><i>p</i>-nitrophenol</b>            Ring: 4 fold-hollow            2 O: Top            1 OH: hollow</p>		<p>Pt<sub>T</sub>-Pt<sub>T</sub> : 2.8 Å            O<sub>1</sub>-O<sub>2</sub> : 2.2 Å</p>
<p><b><i>p</i>-quinone</b>            Ring: 4 fold-hollow            2 O: hollow</p>		<p>Pt<sub>H</sub>-Pt<sub>H</sub> : 5.5 Å            O<sub>1</sub>-O<sub>4</sub> : 5.3 Å</p>
<p><b>Squaric acid (dianion)</b>            Ring: hollow            4 O: Top</p>		<p>Pt<sub>T</sub>-Pt<sub>T</sub> : 2.8 Å            O<sub>1</sub>-O<sub>2</sub> : 3.2 Å            O<sub>2</sub>-O<sub>3</sub> : 3.1 Å</p>

Guided by the adsorption behavior of *p*-nitrophenol on Pt surfaces, we conclude the directions to select molecules with Pt {100} facet binding specificity. First, the molecule should have almost neutral electrostatic potential on its ring. Secondly, there is geometric matching relationship between molecular function groups and Pt (100) lattice, which directly contributes to the binding. To further demonstrate the guidelines, we rationally select *p*-quinone and squaric acid as Pt {100} facet-specific surfactants to control Pt nanocubes synthesis. The geometric matching models of these molecules on Pt (100) lattice are also depicted in Table 4.6. As shown in Figure 4.10a and f, both of *p*-quinone and squaric acid (in the form of dianion) have a blue region on their ring corresponding to positive electrostatic potential ( $+80 \text{ kJ mol}^{-1}$ ), indicating a more  $\pi$  electron-deficient ring than that of *p*-nitrophenol. Moreover, their carbonyl groups can well match the hollow site or top of Pt atoms on Pt (100) lattice by locating the rigid ring on the 4-fold hollow position (considered as the most stable configuration) (Table 4.6). As expected, *p*-quinone and squaric acid can regulate 67% of Pt nanocubes with an average size of  $5.8 \pm 0.9$  and 75% of Pt nanocubes with an average size of  $6.9 \pm 0.7 \text{ nm}$ , respectively (Figure 4.10b, e, g and j), suggesting their binding selectivity to Pt {100} facets. The corresponding HRTEM images in Figure 4.10c-d show a 7 nm- and 5 nm- Pt nanocube, respectively, confirming the obtained Pt NCs in Figure 4.10b are shaped as cubes. Squaric acid is known as a strong acid with  $\text{pK}_2 = 2.2$ , so it should appear in the form of dianion (all carbon atoms have  $\text{sp}^2$  hybridization with symmetric C-C and C-O bonds) in the synthetic solution with  $\text{pH} = 4$  (Figure 4.10f).<sup>82</sup> The obtained NCs from the squaric acid controlled synthesis include cubes and some truncated cubes (predominately enclosed by {100} faces) as shown in Figure 4.10 g-i. To conclude, we successfully employ the discoveries to rationally select Pt {100} facet-specific surfactants and

demonstrate their ability to control the syntheses of Pt nanocubes through selectively binding on Pt {100}.

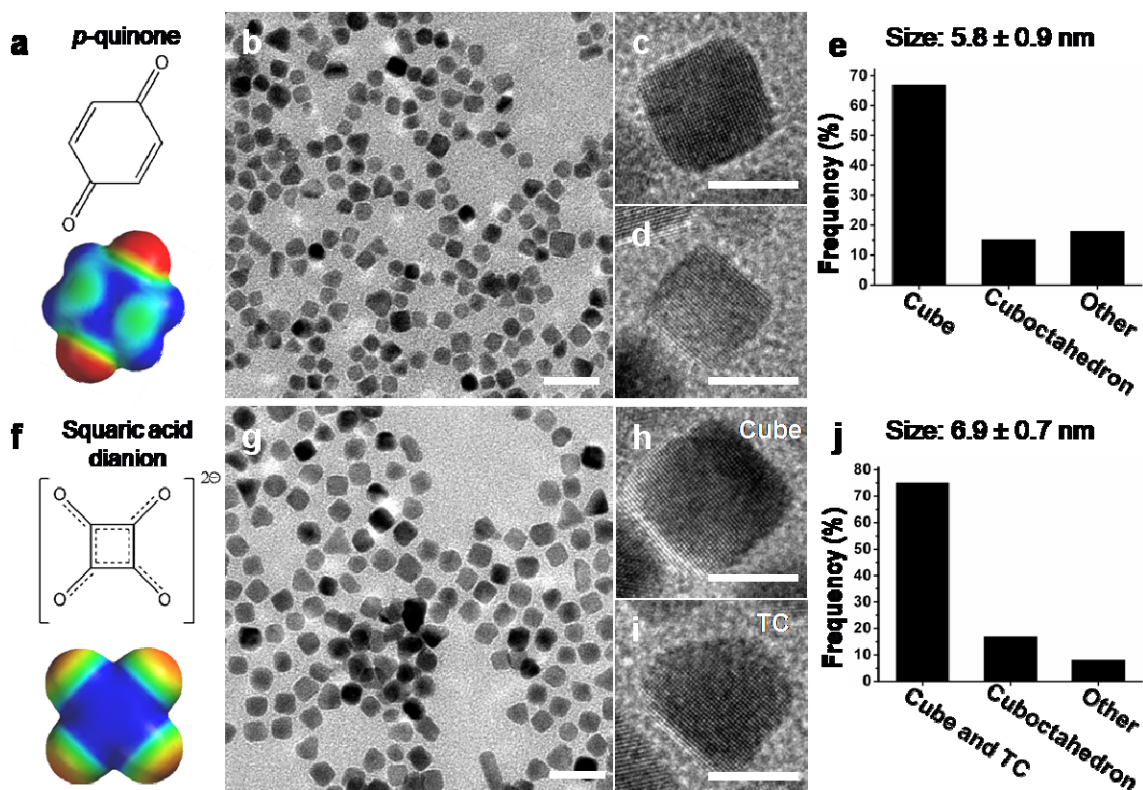


**Figure 4.10** Pt nanocubes controlled by molecules with a positive electrostatic potential surface. (a, f) Molecular structure and electrostatic potential surface of (a) *p*-quinone and (f) dianion of squaric acid. (b, g) TEM images of the obtained Pt NCs. (c-d) and (h-i) are HRTEM images of Pt NCs observed in b and g, respectively. (e) and (j) are the corresponding size and shape distributions of NCs in b and g, respectively. Scale bars: 20 nm in b and g; 5 nm in c-d and h-i. TC: truncated cube. Electrostatic potential: [-80 kJ mol<sup>-1</sup> (red) to +80 kJ mol<sup>-1</sup> (blue)].

### Derived design strategies and shape control of Pd NCs

Our discoveries from Pt system are transferable to another metal system, in particular, palladium (Pd). Since Pd and Pt share the same crystal structure (face-center cubic) and a small lattice mismatch (0.77%), they have been used to synthesize bimetallic core-shell NCs based on

their favorable epitaxial relationship.<sup>83</sup> We can expect that the molecules showing geometric matching on Pt surfaces could perform similarly on Pd surfaces. On the other hand, work function of Pd is lower than Pt, which should decrease the tendency of  $\pi$  electron donation from the ring system to Pd and lead to a weaker Pd-aromatic molecules interaction.<sup>62</sup> To establish a clear panel of these energy levels, we used DFT-PBE calculations to derive  $\epsilon_{\text{HOMO}}$  of the organic molecules studied here and the work functions of Pt and Pd surfaces (Table 4.7). By setting vacuum level as 0 and Fermi level ( $E_{\text{F}}$ ) of metal as  $-\phi$  ( $\phi$ : work function of clean metal surface), the HOMO energy levels of molecules and work functions (or Fermi level) of different metal surfaces can be compared. To achieve charge-transfer interaction,  $\epsilon_{\text{HOMO}}$  of aromatic molecules should be higher than  $E_{\text{F}}$  of the specific metal surface, which is evident for Pt {111} binding specific molecules (Table 4.7). Similarly, aromatic molecules with higher  $\epsilon_{\text{HOMO}}$  than  $E_{\text{F}}$  of Pd (111) will be more likely to bind to it. Based on the calculations, we selected promising organic molecules showing binding affinity to Pd (111). Phloroglucinol is excluded in binding to Pd (111), since its  $\epsilon_{\text{HOMO}}$  is lower than  $E_{\text{F}}$  of Pd (111). Catechol and pyrogallol, with  $\epsilon_{\text{HOMO}}$  close to  $E_{\text{F}}$  of Pd (111) are not effective, either. Syringol and *p*-aminophenol are also excluded because their functional groups might interact with Pd surfaces differently. Therefore, only hydroquinone and hydroxyquinol are potential candidates for selective binding on Pd (111) facets. By this manner, hydroquinone ( $\epsilon_{\text{HOMO}}$ : -5.34) was found to be able to yield 78% of Pd nano-octahedra (enclosed by Pd {111} facets) with average edge length of  $8.0 \pm 0.9$  nm (Figure 4.11a; shape distribution in Figure 4.11d), indicating its Pd {111} face specificity [ $E_{\text{F}}$  of Pd (111): -5.59]. However, hydroxyquinol failed to control the formation of Pd octahedra (Figure 4.12a). We suspect that hydroxyquinol may get oxidized in the reaction (80 °C) and lose binding specificity to Pd (111), since it should be the most active among the discussed phenolics.<sup>84</sup> Blank reaction

and the other controlled with Pt {111} facet-specific molecules such as phloroglucinol and catechol cannot generate well-defined Pd nanocrystals (Figure 4.12b-d), suggesting the exclusive binding selectivity of hydroquinone to Pd {111} facet and the success of our selection approach. In addition, we select terephthalic acid with almost neutral electrostatic potential (ranging from -20 to 10 kJ mol<sup>-1</sup>) on the center and with geometric matching to Pd (100) (Figure 4.11b and Table 4.8) to be a Pd {100} facet-specific surfactant. As expected terephthalic acid can control the synthesis of Pd nanocubes with a yield of 82% and an average size of 8.4 ± 1.0 nm (Figure 4.11c and e), confirming its Pd {100} facet specificity. Interestingly, terephthalic acid can also be used to synthesize Pt nanocubes, showing binding effect on Pt {100} facets (Figure 4.13). However, we observed Pt {100} binding molecules (e.g., *p*-quinone and squaric acid) are ineffective to synthesize Pd nanocubes (Figure 4.12e and f), indicating these molecules might show different binding effect on Pd. It is suspected that the synthetic environment might play a role here since Pt nanocrystals synthesis was conducted in aqueous solution at room temperature, while Pd was produced in DMF and water mixed solution at 80 °C. Further studies are needed to reveal the fundamentals behind the syntheses. Nevertheless, the molecular selection approach based on electrostatic potential and geometric matching has been demonstrated effective in designing and identifying Pd {111} and Pd {100} facet-specific molecules, representing a step forward to generalize the binding mechanism of organic surfactants on inorganic materials.

**Table 4.7** The energies of highest occupied molecular orbital ( $\epsilon_{\text{HOMO}}$ ) of small molecules calculated at density functional B3LYP/ 6-31G\* level (Spartan) and DFT-PBE (VASP), respectively. Work functions of different metal surfaces from references and obtained via DFT-PBE calculations are given below, respectively.

<b>Molecule</b>	<b>HOMO (BLYP3) (eV)</b>	<b>HOMO (DFT-PBE) (eV)</b>
Terephthalic acid	-7.4	-7.15
<i>p</i> -quinone	-7.4	-6.64
<i>p</i> -nitrophenol	-6.9	-6.36
Benzene	-6.7	-6.36
Squaric acid	-6.5	-5.83
Phenol	-6.0	-5.96
Gallic acid	-6.0	-5.83
Resorcinol	-5.8	-5.66
		$E_{\text{F}}$ of Pt (111): -5.77 Set $E_{\text{VAC}}$ as 0
Phloroglucinol	-5.8	-5.64
		$E_{\text{F}}$ of Pd (111):-5.59
Catechol	-5.6	-5.43
Pyrogallol	-5.6	-5.51
Hydroquinone	-5.4	-5.34
Syringol	-5.3	-5.39
Hydroxyquinol	-5.2	-4.86
<i>p</i> -aminophenol	-5.0	-4.71
<b>Metal surface</b>	<b>Work function (ref.)</b>	<b>Work function (<math>\phi</math>) (DFT; PBE)</b>
Pt (111)	6.1 <sup>64</sup> /5.7 <sup>85</sup> /5.93 <sup>65</sup>	5.77
Pt (100)	5.84 <sup>65</sup>	5.71
Pd (111)	5.6 <sup>85</sup> /5.5 <sup>86</sup>	5.59
Pd (100)	5.3 <sup>86</sup>	5.25

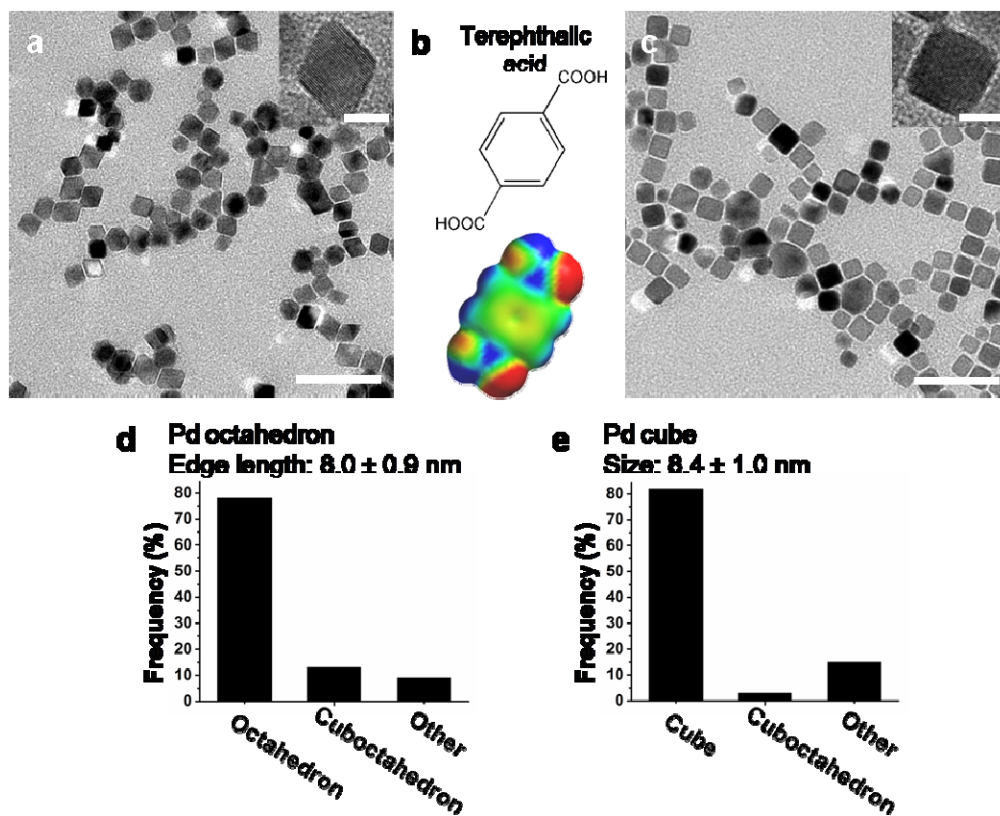


**Figure 4.11** Pd nano-octahedra and nanocubes synthesized by hydroquinone and terephthalic acid, respectively. (a) TEM image of Pd NCs controlled by hydroquinone; inset: HRTEM image of a Pd octahedron. (b) Molecular structure and electrostatic potential surface of terephthalic acid. (c) TEM image of Pd NCs controlled by terephthalic acid; inset: HRTEM image of a Pd cube. (d-e) Shape distributions of hydroquinone (d) and terephthalic acid (e) controlled synthesis of Pd NCs. Scale bars: 40 nm in a and c; 5 nm in insets. Electrostatic potential:  $[-80 \text{ kJ mol}^{-1}$  (red) to  $+80 \text{ kJ mol}^{-1}$  (blue)].



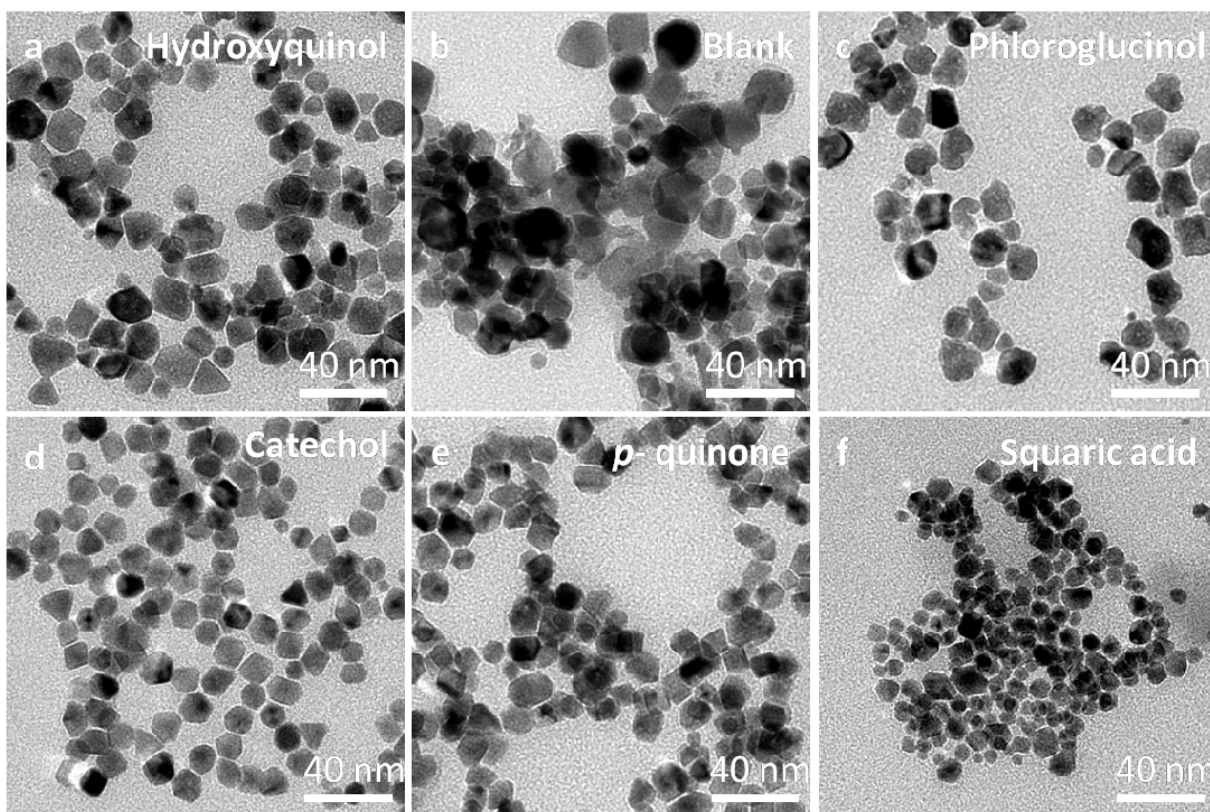


**Figure 4.12** Control experiments of Pd NCs synthesized by other organic molecules than Pd {111} and Pd {100} facet-specific molecules. TEM images of the obtained Pd NCs in the presence of 3 mg of hydroxyquinol (a); no surfactant (b); 3 mg of phloroglucinol (c); 3 mg of catechol (d); 3 mg of *p*-quinone (e); 6 mg of squaric acid (f).

**Table 4.8** Geometric matching of terephthalic acid on Pd (100) surface

	Configuration on Pd (100)	Epitaxial relation
<b>Terephthalic acid<sup>1</sup></b> Ring: 4 fold-hollow 4 O: Top		Pd <sub>T</sub> -Pd <sub>T</sub> (1): 8.3 Å Pd <sub>T</sub> -Pd <sub>T</sub> (2): 2.8 Å O <sub>1</sub> -O <sub>2</sub> : 7.0 Å O <sub>2</sub> -O <sub>3</sub> : 2.2 Å

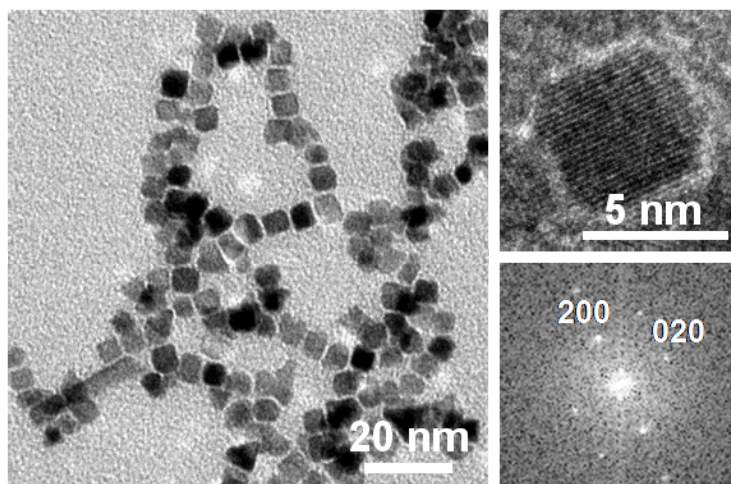


**Figure 4.13** TEM image of Pt cubes with a yield of 73 % controlled by terephthalic acid. Pt NCs were synthesized in the reaction with 15  $\mu\text{g/ml}$  terephthalic acid, 2.4 mM  $\text{K}_2\text{PtCl}_4$ , 2 mM ascorbic acid and 1 mM  $\text{NaBH}_4$  in the solution containing 3.5 ml DMF and 1.5 ml water, reacting in a 60  $^\circ\text{C}$  oil bath for two hours.

In summary, the rational approaches to designing organic molecules with predictable binding selectivity to metal surfaces have been formulated, guided by their molecular electrostatic potential surface, along with soft-epitaxial matching. The negative electrostatic potential on the ring system of aromatic molecules is the prerequisite to determine the binding selectivity to Pt  $\{111\}$  facets. The electrostatic potential can be tuned by the number, position and electron affinity of the substituents on the ring, suggesting a controllable method to modulate the facet selectivity as well as the organic-inorganic interface. The geometrical matching relationship between the structures of aromatic molecules and the Pt (111) surface also contributes to the binding mechanisms. Based on our discoveries, several aromatic molecules showing Pt  $\{111\}$  facet binding specificity are identified and applied to generate Pt nanotetrahedra. Through Raman characterization, we can infer the molecular binding configurations on the metal surfaces. It is evident that hydroquinone with Pt  $\{111\}$  facet binding specificity

adsorbs parallel to Pt (111) surface via aromatic ring and hydroxyl groups. On the other hand, we discovered that organic molecules, such as *p*-nitrophenol, *p*-quinone and squaric acid with almost neutral to positive electrostatic potential on the aromatic ring, can synthesize Pt nanocubes, suggesting their binding selectivity to Pt {100} facets. The geometric matching of the molecular binding sites and the Pt (100) lattice is believed to dominate the binding selectivity. Learning from the Pt system, we effectively designed and identified Pd {111} and Pd {100} facet-specific surfactants and used them to synthesize Pd nano-octahedra and Pd nanocubes, respectively. In this systematic study, the rationality of molecular facet-selective adsorption is successfully demonstrated and employed in advancing synthesis tool of colloidal NCs.

## **Chapter V: PEPTIDE DIRECTED SYNTHESIS AND ASSEMBLY OF ANISOTROPIC NANOCRYSTALS INTO ONE- AND THREE- DIMENSIONAL NANOSTRUCTURES**

Our progress in biomimetics synthesis has demonstrated that the identified biomolecules exhibiting selective binding affinity to different metal surfaces can be exploited to mediate the anisotropic NC formation in synthetic conditions.<sup>43-44,87</sup> The general focus of nanomaterial synthesis is now shifting to the development of larger nanostructures with organization through assembly of individual NCs.<sup>88-89</sup> Complex nanostructures showing the collective properties of the individual building blocks and interfaces bring new possibilities for nanoscience.<sup>89-90</sup> The anisotropic shape of NC and interaction through organic molecules are powerful tools for programmable nanostructure modulations.<sup>91</sup> However, the assembly of anisotropic building blocks into nanostructures with control of organization through oriented attachment remains a challenge due to the difficulty in simultaneously controlling the anisotropy of the building blocks and the resulting nanostructures. Thanks to the recent development in electron microscopy, the real-time imaging of crystal growth through oriented attachment in solution disclosed the alignment process and attachment mechanism.<sup>92-93</sup> The precise manipulation of the crystal growth pathways can be a promising strategy to advance the production of complex nanostructures, yet which is challenging with conventional colloidal methods. It is known the biological systems exploit the recognition properties of biomolecules to control crystal growth pathways, producing sophisticated structures with desirable functions. Therefore, exploiting the full potential of biomolecules in material formation process can provide the opportunity to achieve the controlled synthesis of organized nanostructures, advancing the colloidal synthesis.

Here, we demonstrate an intriguing approach to synthesize hierarchical nanostructures in mild chemical conditions, e.g., in aqueous solution at room temperature, characteristic of biomineralization. Platinum (Pt) facet-specific peptides, i.e., T7 and S7 were exploited to

produce 1-D and 3-D Pt nanostructures composed of cubic or tetrahedral NCs through nanoparticle attachment. We believe that the specific peptide-peptide and peptide-metal surface interactions are the dominant driving force since the dipole mechanism known as a general argument of oriented attachment for semiconductor and magnetic material is not held for metal.

### **A. Experimental methods**

All reagents are dissolved in water before use. In particular, the concentration of T7 aqueous solution is 0.5 mg/ml, S7 1 mg/ml and  $K_2PtCl_4$  10 mM. The total volume of all reaction solution is 5 ml. The concentrations indicated are all final concentration. The reactions are conducted at room temperature with strong stirring and with pH 5-6. In S7 peptide controlled syntheses, 1 mM  $H_2PtCl_6$ , 30-50  $\mu$ g/ml S7 peptides and 2 mM ascorbic acid were pre-mixed with water in a vial, and  $NaBH_4$  aqueous solution with a final concentration of 0.8 mM was injected in one shot. Total reaction time is 30 minutes. For the T7-S7 reaction, 1 mM  $H_2PtCl_6$ , 3  $\mu$ g/ml T7 and 2 mM ascorbic acid were pre-mixed with water in a vial, and  $NaBH_4$  aqueous solution with a final concentration of 0.8 mM was injected in one shot. After 10 seconds, 25  $\mu$ g/ml of S7 (final concentration) was added into the reaction. For the S7-T7 reaction, similar reaction conditions were used, except 19  $\mu$ g/ml S7 was pre-mixed at first and 3  $\mu$ g/ml of S7 was added after 10 seconds of reaction. Total reaction time is 1 hour.

For 3-D nanocube assembly, the synthesis method is similar to the T7-S7 reaction, except after 10 seconds of reaction 250  $\mu$ l of  $K_2PtCl_4$  aqueous solution were added together with 125  $\mu$ l of S7 aqueous solution into the reaction; total reaction time is 1 hour. This method was used for the rest assembly syntheses, except some variations are listed below: for 1-D nanocube assembly, 3  $\mu$ g/ml T7 was in the reaction before 250  $\mu$ l of T7; for 3-D nano-tetrahedron assembly, 10  $\mu$ g/ml T7 was before 100  $\mu$ l of S7; for 1-D nano-tetrahedron assembly, 1 mM ascorbic acid and

10  $\mu\text{g/ml}$  S7 were used at first, and after 30 seconds of reaction 100  $\mu\text{l}$  of T7 was added with  $\text{K}_2\text{PtCl}_4$ .

The synthesized nanocrystals were imaged by a FEI CM 120 transmission electron microscopy (TEM) operated at 120 kV and FEI TITAN high resolution transmission electron microscopy (HRTEM) at 300 kV. All TEM samples for imaging were prepared by pipetting the solution onto carbon-coated copper grids. TEM samples were dried in atmosphere before images were taken.

## **B. Results and discussion**

### **S7 peptide induced aggregation of Pt nanoparticles**

S7 peptide (Ser-Ser-Phe-Pro-Gln-Pro-Asn) which was shown in Chapter III displays exclusively binding selectivity to Pt {111} facets. We systematically study the effect of S7 on the synthesis of Pt NCs as a function of its concentrations. As shown in Figure 5.1a-d, Pt NCs trend to form aggregates as S7 concentration increases. Clearly, at lower concentrations 30 and 35  $\mu\text{g/ml}$ , single nanoparticles are dominant, while at higher concentrations 40 and 50  $\mu\text{g/ml}$ , aggregates of Pt nanoparticles (two, three and more) prevail (Figure 5.1a-d and k). 30  $\mu\text{g/ml}$  S7 in the reaction can synthesize 62 % of tetrahedra (Figure 5.1a and e), which was used as the optimal concentration of S7 to generate monodispersed Pt tetrahedra with similar synthetic conditions (Chapter III). In that case, Pt tetrahedra enclosed with Pt (111) surfaces are assumed to be adsorbed with a monolayer of S7. As the concentration of S7 increases, the excessive peptides may begin to bind on nonspecific facets (other than Pt {111}) or interfere the crystal growth pathways, leading to the formation of Pt NCs with exceptional morphologies. At the medium S7 concentration 35-40  $\mu\text{g/ml}$ , single concaved tetrahedra (Figure 5.1f-g) are observed in addition to aggregates (Figure 5.1h-i), suggesting excessive S7 may bind on Pt {110} facets

(the excavated face of concave tetrahedron). At the high concentration 50  $\mu\text{g/ml}$ , most Pt NCs (84%) are aggregates of nanoparticles (Figure 5.1j and k), indicating extra S7 can regulate crystal growth pathways to benefit nanoparticle aggregation.

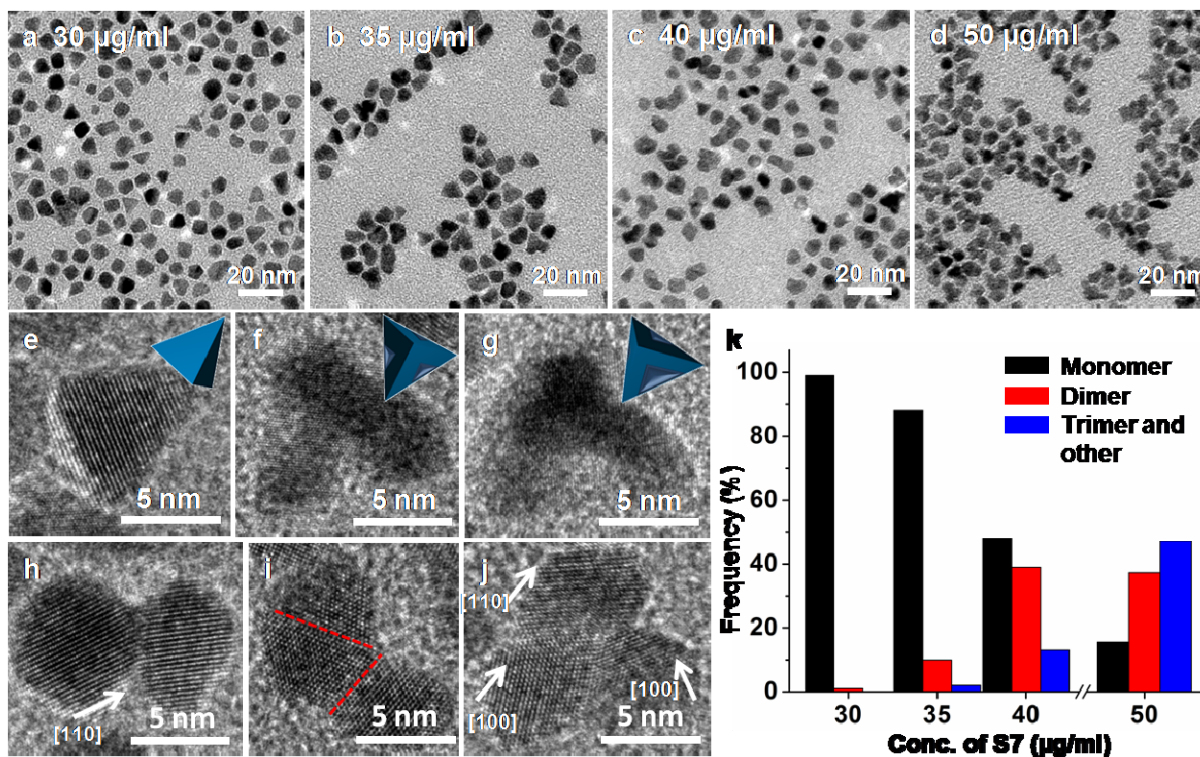


**Figure 5.1** TEM images of Pt NCs synthesized with different concentrations of S7 peptide: (a) 30  $\mu\text{g/ml}$ , (b) 35  $\mu\text{g/ml}$ , (c) 40  $\mu\text{g/ml}$  and (d) 50  $\mu\text{g/ml}$ ; reaction time: 30 minutes. (e) HRTEM image of tetrahedron in a. (f-g) are HRTEM images of concaved tetrahedron found in b-c, respectively. (h) HRTEM images of Pt dimer aggregate in b. (i-j) are HRTEM images of Pt trimer aggregate found in c-d, respectively. Black triangles label the neck and interface of attached nanoparticles. Red dashed lines mark the twinned boundaries. (K) Statistics of number of nanoparticles in an aggregate as a function of concentration of S7. Insets in e-g are schematic models showing tetrahedron and concaved tetrahedron.

We continued to study the S7-directed aggregation process as a function of the reaction time using the nanocrystal synthesis with 50  $\mu\text{g/ml}$  S7 as an example (Figure 5.2). As the reaction proceeds from 10 seconds to 10 minutes, the frequency of single nanocrystals decreases 32 %, while those of dimer and trimer aggregates increase accordingly (Figure 5.2a-d and i), suggesting the nanoparticles coalesce with reaction time. The initial nuclei at 10 seconds of reaction are spherical-like (enclosed with a mix of  $\{111\}$  and  $\{100\}$  facets) and exhibit an average size of  $3.8 \pm 0.4$  nm (Figure 5.2a and e). The representative HRTEM images of dimer aggregates found in Figure 5.2b-d are shown in Figure 5.2f-h. They exhibit a lattice-mismatched or lattice-matched interface between nanoparticles, e.g., twin plane indicated with red line in Figure 5.2g or perfect plane in Figure 5.2h. In all cases, the formation of a neck region indicates the contact point where two nanoparticles attached (Figure 5.2f-h). To observe the crystal growth accompanying aggregation process, we measured the average size of the monomer particles found at different reaction time. They grew ca. 2 nm from 10 seconds to 10 minutes, indicating a significant crystal growth of monodispersed nanoparticles in the early stage (Figure 5.3). After 10 minutes, we observe these single nanoparticles freeze at the specific size (ca. 5.8 nm) which is similar to that of the primary particles of the aggregates found in 30 minutes (ca. 5.3 nm; Figure 5.3, Figure 5.1d and j), indicating that most single nanoparticles predominantly form aggregates after 10 minutes (Figure 5.2i). Therefore, a portion of initial nanoparticles are mono-dispersed in solution until they grow to a critical size, at which nanoparticle coalescence begin to dominate the crystal growth.



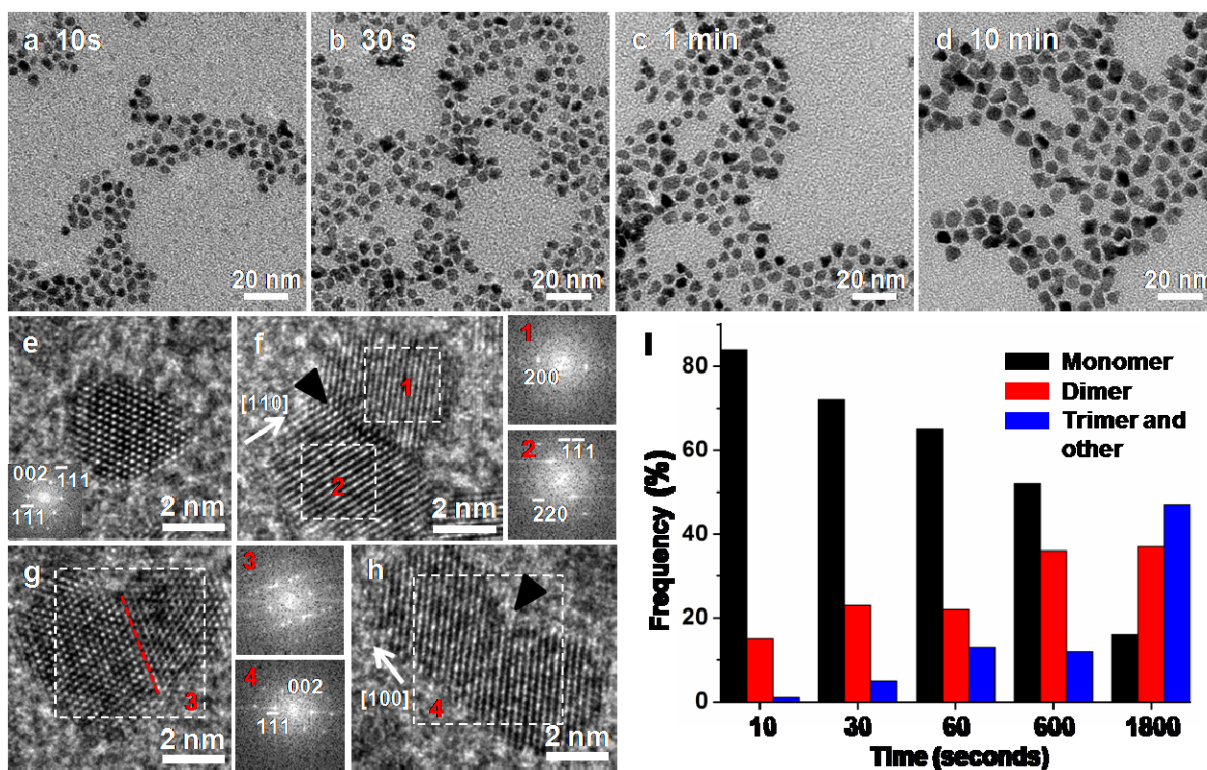


**Figure 5.2** S7 peptide directed nanoparticle coalescence process. (a-d) TEM images of Pt NCs obtained from the reaction with 50  $\mu\text{g/ml}$  of S7 at different time: (a) 10 seconds, (b) 30 seconds, (c) 1 minute and (d) 10 minutes. (e) HRTEM image of single Pt nanoparticle from a. (f-h) HRTEM images of attached nanoparticles (dimer) in b-d respectively. Red dashed line marks the twin boundary. Black triangles label the neck of two attached nanoparticles. (1-4) showing the corresponding FFT (fast Fourier transformed) patterns of the selected area in HRTEM images of f-h, respectively; 3 reveals twinned structure with double domains; 4 shows the single crystalline structure of the dimer aggregate. (i) Statistics of the number of nanoparticles in an aggregate as a function of reaction time.

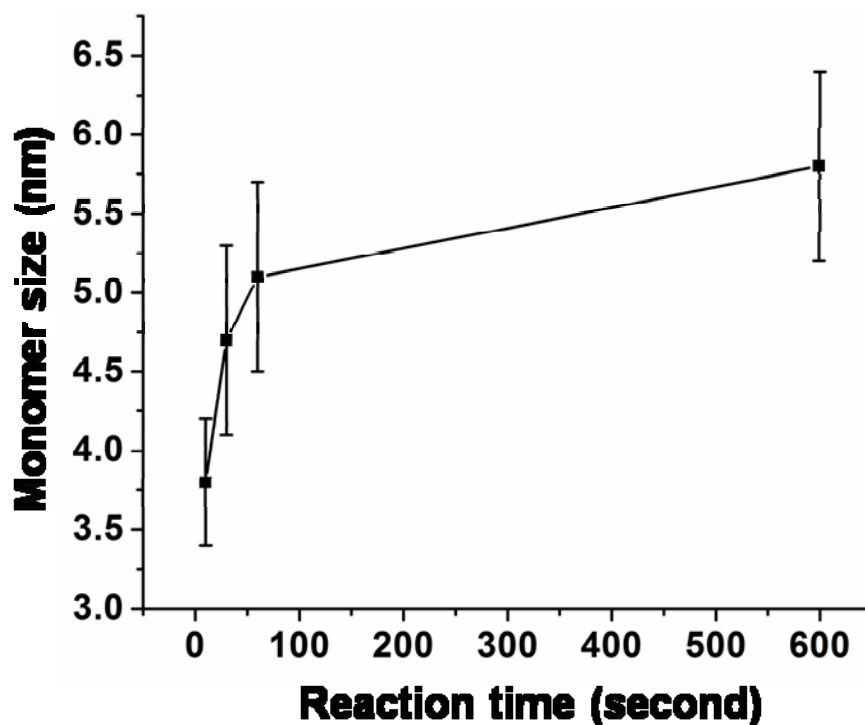


**Figure 5.3** The size of Pt monomers obtained from the synthesis with 50  $\mu\text{g/ml}$  S7 as a function of reaction time. The monomer size increases faster in the first minute of the reaction.

The above observations of crystal growth are similar to those of single Pt NC and  $\text{Pt}_3\text{Fe}$  nanorod via *in situ* TEM, but they exhibit other features resulted from the specific binding effect of S7 on Pt surfaces.<sup>93-94</sup> Generally, it is shown colloidal NCs take the both crystal growth pathways including atom addition and nanoparticle coalescence which is accompanied with a structure relaxation period to generate single crystalline and mono-dispersed nanoparticles in solution.<sup>94</sup> With a lower concentration of S7, the production of mono-dispersed Pt tetrahedra may adopt similar growth pathways while using S7 to kinetically control the shape of NCs, suggesting that the events such as atom deposition on active facets, atom diffusion on metal surfaces and removal of internal defects are allowed.<sup>94</sup> However, a higher concentration of S7 generates smaller nuclei, i.e., a larger number of mobile and high energy nanoparticles, which can increase collision frequency and benefit multiple nanoparticle coalescence.<sup>94-95</sup> In addition,

we believe the fact that S7 shows Pt {111} facet binding specificity alters the usual picture of surfactants, i.e., they can stabilize particle surfaces and build a barrier to coalescence.<sup>1,21</sup> We observed that the nanoparticles are most likely to attach along [110] or [100] directions except the twinned structures (Figure 5.1h-j and Figure 5.2f-h). S7 can selectively stabilize Pt {111} facets which have a lower surface energy in nature, leading to a scenario that the other surfaces such as (110) and (100) (even with adsorption of S7) exhibit higher energy than S7 on Pt (111). High-energy facets such as exposed on the initial nanoparticles can drive a quick response to reduce the total energy of the system either by atom-by-atom addition or by nanoparticle attachment in solution.<sup>1,21,93</sup> The dominant growth mechanism is determined by the availability of reduced Pt atoms from the precursor and the existed small nanoparticles. In the classic LaMer model, after a burst of nucleation spontaneous growth on nuclei is diffusion-limited due to the depletion of precursor around the nuclei.<sup>96</sup> To put together, we propose the mechanism of the S7 induced nanoparticle coalescence. A high concentration of S7 promotes the production of abundant small nanoparticles in the initial reaction, which can drive coalescence. At the same time, a continuous supply of atoms by reducing the remaining precursor can grow a portion of nuclei via atom addition to reduce overall surface energy. Subsequently, the depletion of precursor limits the supply of atoms, and instead nanoparticle coalescence dominates the crystal growth. It is worthy to note that the interface of the attached particles formed initially remain in the final aggregates, indicating the adsorption of S7 on metal surfaces can inhibit structure relaxation and arrests defects in nanostructures (Figure 5.1j and 5.2f-g). This offers an alternative strategy to modulate the properties of nanomaterial through crystalline engineering.<sup>97</sup> These results demonstrate that precise control over S7 concentration can switch the crystal growth

pathways and consequently favor nanoparticle attachment through its binding selectivity, providing a potential ground to achieve controlled synthesis of complex nanostructures.

### **Oriented attachment of nanocubes and nano-tetrahedrons**

Another peptide T7 (Thr-Leu-Thr-Thr-Leu-Thr-Asn), also shown in Chapter III, displaying binding selectivity on Pt {100} facets is introduced into the reactions not only to shape the building blocks but also to confine the directions of coalescence, leading to the synthesis of single crystalline nanostructures through oriented attachment. As shown in Figure 5.4, the sequential introduction of T7 and S7 into the reaction can achieve the synthesis of 3-D nanostructures composed of cubic nanoparticles sharing the same orientation. Specifically, 3  $\mu\text{g/ml}$  of T7 peptide was incubated with precursor, and subsequently one injection of  $\text{NaBH}_4$  initiated the Pt NC synthesis. After 10 seconds of reaction, 25  $\mu\text{g/ml}$  of S7 peptide was introduced to induce oriented attachment. The time indicated in the images of assemblies represents the reaction time after introducing both T7 and S7 (Figure 5.4 and 5.5). After 30 seconds of reaction with T7 and S7, the obtained nanocrystals are monodispersed and shaped as truncated cubes (Figure 5.4a, d and g), suggesting the shaping peptide T7 selectively binds on Pt {100} facets and dominates the initial reaction. After 90 seconds, aggregates composed of two or three truncated cubes were observed, indicating S7 started to influence the crystal growth pathways to prefer oriented attachment (Figure 5.4b, e and h). The individual truncated cubes tend to attach on their edge sides ({110} facets) which are reactive since neither S7 nor T7 shows binding specificity on them. As the reaction proceeds to 1 hour, all individual nanoparticles disappear and consequently self-assemble into the nanostructures with multiple truncated cubes attached along [110] direction, (Figure 5.4c, f and i). The HRTEM images and their

corresponding FFT patterns show the single crystal nature of the obtained nanostructures (Figure 5.4e-f and h-i).

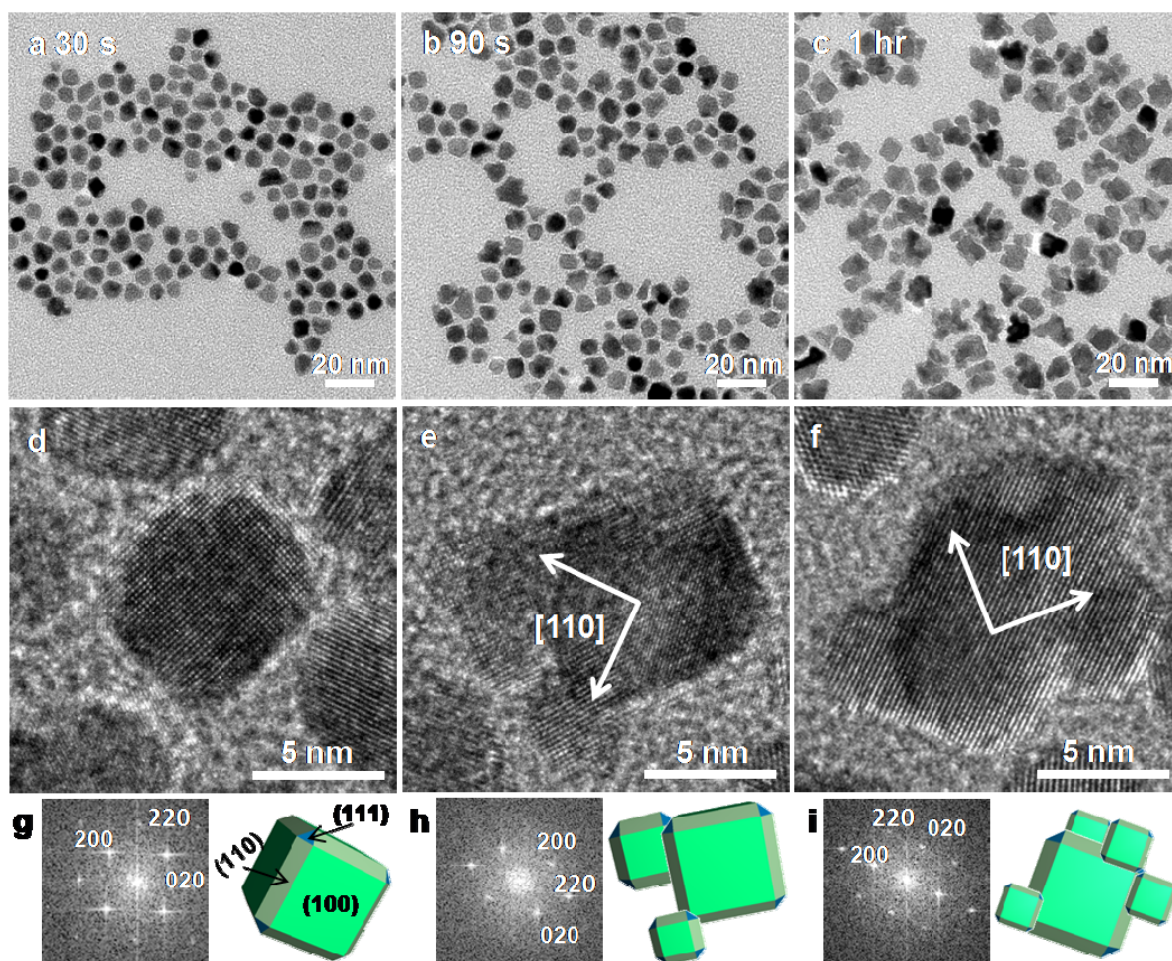


**Figure 5.4** T7-S7 peptide directed oriented attachment of nanocubes. (a-c) TEM images of the obtained nanoparticles at different reaction time after introducing both peptides: (a) 30 seconds, (b) 90 seconds and (c) 1 hour. (d-f) are HRTEM images of the representative nanoparticle in a-c, respectively. (g-i) are the corresponding FFT patterns and schematic models of e-f, showing the attachment of individual cubic nanoparticles which formed earlier is directed along [110].

Simply switching the order of T7 and S7 added into the reaction, 3-D nanostructures with tetrahedra as building blocks attached along [110] directions can be produced (Figure 5.5). The experimental method is the same as the T7-S7 reaction except 19  $\mu\text{g/ml}$  of S7 is added before 3

$\mu\text{g/ml}$  of T7. Individual truncated tetrahedra can be obtained in the early stage of reaction, confirming the shaping effect of the first peptide, S7 (Figure 5.5a, d and g). Subsequently, in the similar fashion they can assemble into multi-tetrahedra nanostructures with single crystal nature through oriented attachment along  $[110]$  directions as a result of the binding specificity of S7 and T7 (Figure 5.5b-c, e-f and h-i). Strategically combining the two types of surfactants (S7 and T7) showing characteristic binding affinity on different surfaces, we have demonstrated, for the first time, the production of 3-D nanostructures composed of cubic or tetrahedral NCs through oriented attachment (Figure 5.4-5.5).

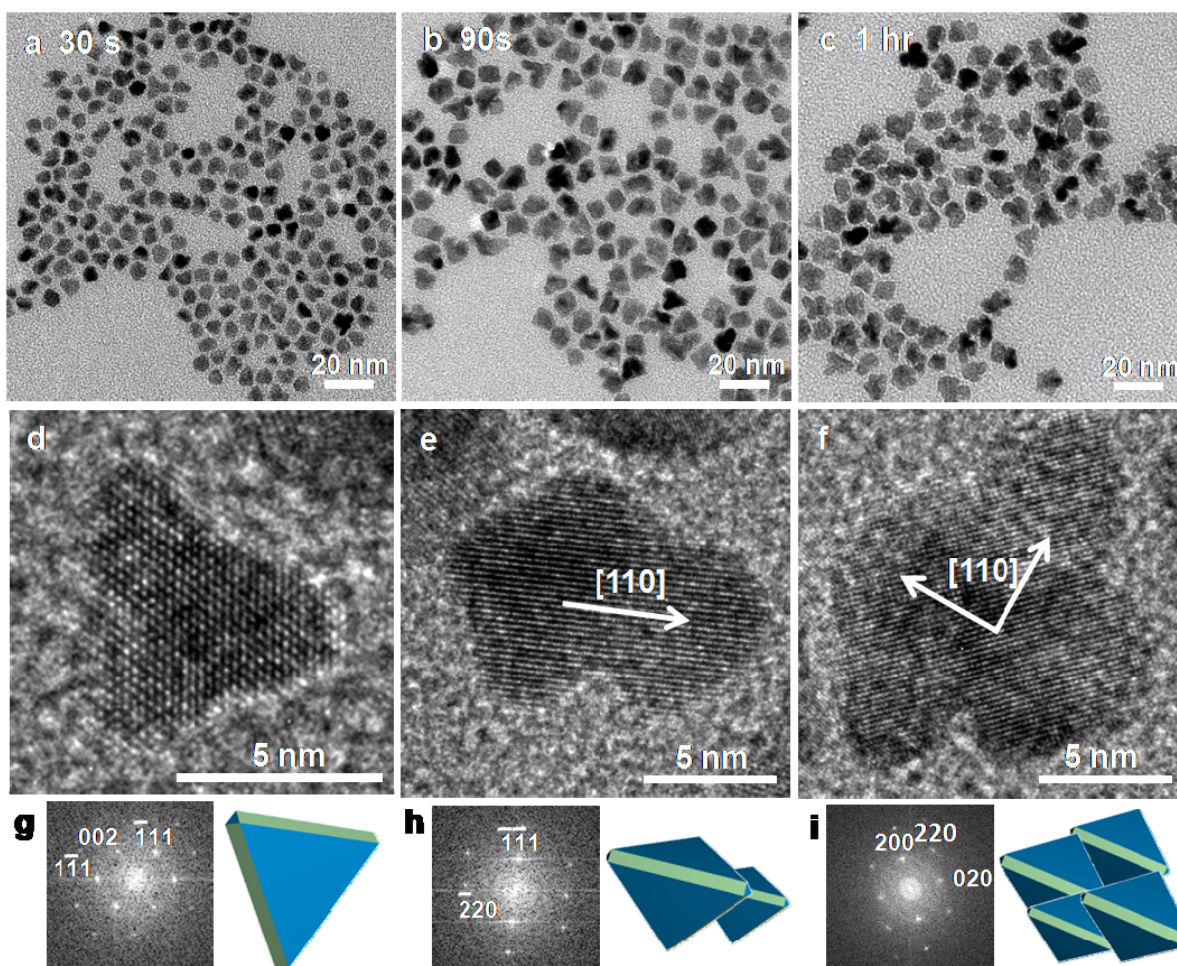


**Figure 5.5** S7-T7 peptide directed oriented attachment of nano-tetrahedra. (a-c) TEM images of the obtained nanoparticles at different reaction time after introducing both peptides: (a) 30

seconds, (b) 90 seconds and (c) 1 hour. (d-f) are HRTEM images of the representative NCs in a-c, respectively. (g-i) are the corresponding FFT patterns and schematic models of d-f, showing the tetrahedral particle attachment is directed along [110].

To further investigate the fundamentals behind the syntheses, it is of importance to study the reaction parameters manipulating the synthesis and the self-assembly of the anisotropic nanoparticles into nanostructures, such as the interval between T7 and S7 and their concentrations. Using the S7-T7 reaction as an example, we systematically tuned the time interval (0, 30 seconds and 1 minute), while the other reaction conditions were kept constant (Figure 5.6). Only the reaction using the 30 seconds-interval can synthesize aggregated nanoparticles as predominant products which are similar to the 10 seconds' results showed in Figure 5.5. In contrast, as introducing T7 and S7 at the same time (shorter interval) or sequentially introducing them with a longer interval (1 minute), mono-dispersed nanoparticles are dominant. For the reaction in the presence of both T7 and S7 in the beginning, it is possible that only one of them interacts with single nanoparticles and predominantly controls the crystal growth, inhibiting coalescence. In the case of a longer interval, one minute of reaction time has allowed the NCs to develop more complete tetrahedra which provide less reactive surfaces exposed on NCs, preventing T7 from driving oriented attachment. The concentrations of T7 and S7 which can approximately gauge their interaction with NC synthesis are critical as well to the purpose of oriented attachment. We conducted a series of experiments using different concentrations of T7 and S7 (ranging from 0 to 30  $\mu\text{g/ml}$ ) to observe the morphology of the resulting NCs. In both T7-S7 and S7-T7 controlled reactions, nanoparticle assemblies are dominant within a specific concentration window of T7 and S7 (Figure 5.7), indicating a fair interaction of both T7 and S7 on crystal surfaces are essential. Outside of the boundaries of the

window, the obtained NCs are dominated by single cubes or tetrahedra depending on the concentrations, suggesting that either T7 or S7 control the reaction. In addition, nanoparticle coalescence can be achieved in the presence of a lower concentration of S7 (than those of S7 in Figure 5.1) by strategically including a secondary facet-specific peptide (T7), indicating the development of another effective approach to switch the crystal growth pathways. Obviously, appropriate time interval and peptide concentrations are exceptionally important to allow both T7 and S7 to influence the synthesis while separately. The combinatory effect of T7 and S7 can efficiently arrest the initial truncated nanoparticles and contribute to the exposure of high energy surface, i.e., (110), driving crystal growth through oriented attachment along [110] directions.

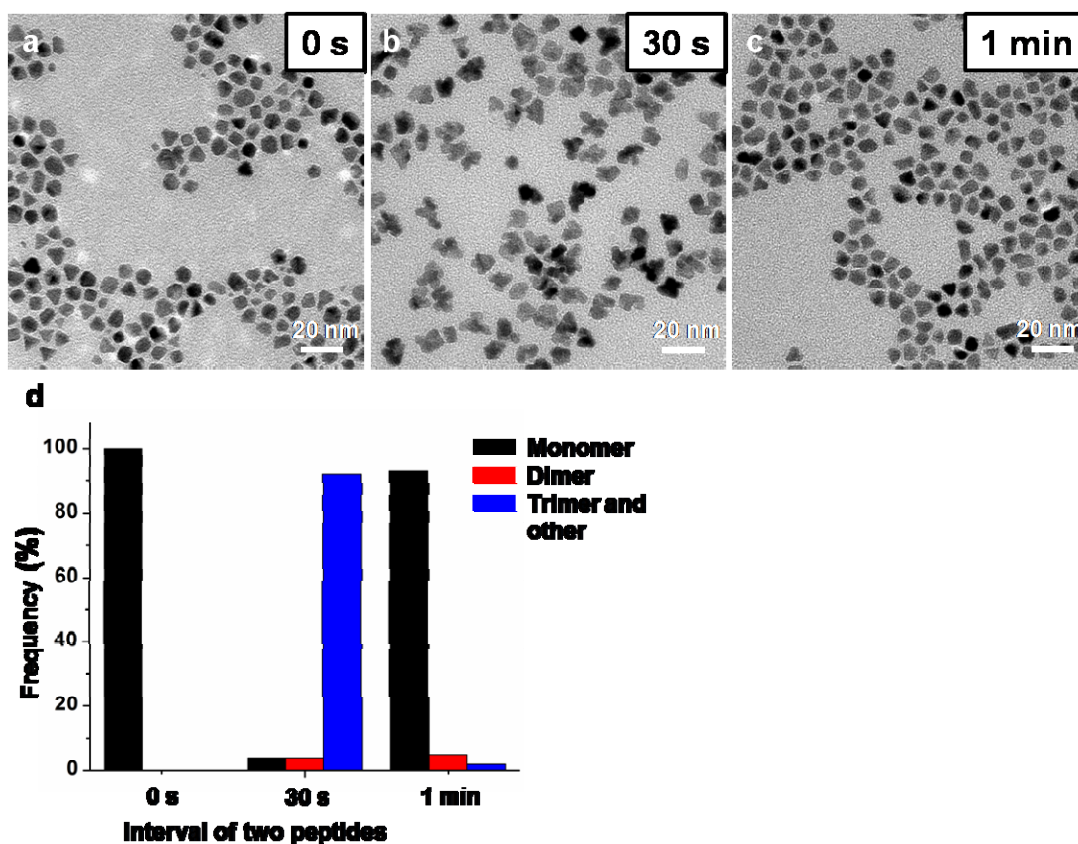


**Figure 5.6** The effect of the length of the interval between S7 and T7 introduced into reactions on the Pt NC synthesis. (a-c) TEM images of Pt NCs obtained from the reactions in the presence



of 19  $\mu\text{g/ml}$  of S7 after reacting for (a) 0 seconds, (b) 30 seconds and (c) 1 minute, 3  $\mu\text{g/ml}$  of T7 was introduced. (d) Statistics of number of nanoparticles in an aggregate as a function of the interval between S7 and T7.

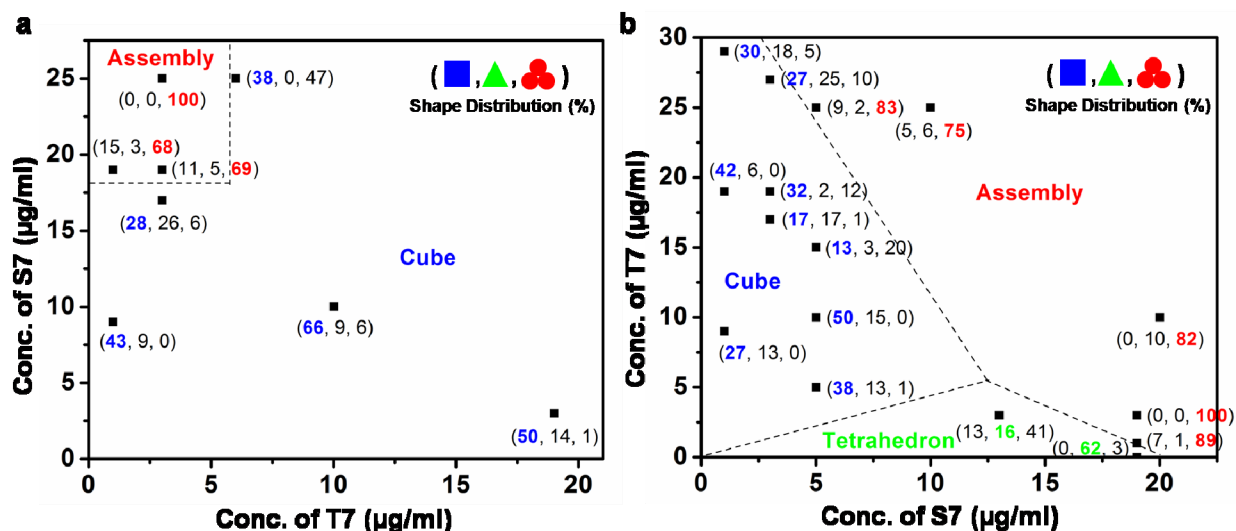


**Figure 5.7** (a) Shape distributions of T7-S7 peptide directed oriented attachment with different concentrations of T7 and S7. The numbers correspond to the frequency (%) of cube, tetrahedron and assembly of nanoparticles obtained using a particular concentration of S7 and T7. The assembly includes dimer, trimer and so on. The sum of the three numbers is not equal to 100 (%) since some monomers shaped as cuboctahedron or others are not included here. As the frequency of assembly is more than 50 %, the controlled experiment corresponding to a certain set of T7-S7 peptide concentration is grouped as Assembly (red). For the rest, the data are grouped into cube (blue) or tetrahedron (green) by comparing their frequencies. (b) Shape distribution of S7-T7 peptide directed oriented attachment with different concentrations of S7 and T7.

It is known in biological systems the cooperative interactions between biomolecules and inorganic ions are of importance to control the material formation.<sup>26-27</sup> In our studies, we think the interaction between peptides such as Van der Waals force, hydrogen bonding and  $\pi$ - $\pi$

interaction (e.g., phenyl ring within phenylalanine of S7) plays a role in the nanostructure synthesis, which can be supported by the fact that higher concentration of peptides favor nanoparticle coalescence.<sup>26,98-99</sup> Through improving the interaction between the organic coatings on metal surfaces, the particle-particle interaction is thus increased to benefit nanoparticle attachment.<sup>100-101</sup> However, further investigation is needed to elucidate the details and validate the relevance. Several works have reported that proteins can interact with salts such as sodium chloride and sodium phosphate and induce a so-called protein salting-out effect through affecting the solubility and stability of proteins, which can strengthen the hydrophobic interaction and trigger proteins aggregation.<sup>102-104</sup> In our synthesis system, Na<sup>+</sup> and Cl<sup>-</sup> can be released from the reactants, i.e., reducing agent (NaBH<sub>4</sub>) and precursor (H<sub>2</sub>PtCl<sub>6</sub>), and then possibly interact with peptides. To confirm the effect of these inorganic ions, we externally introduced NaCl into the reactions with peptides and observed the morphology of the resulting NCs. As shown in Figure 5.8a-b, in the presence of NaCl and 30 µg/ml of S7, Pt aggregates analogous to those from the 50 µg/ml S7 controlled reaction are obtained, (Figure 5.1), suggesting that peptides-ions interaction may aid nanoparticle attachment due to the improved S7 peptide-peptide interaction. This result may account for the observation of the Pt nanoparticles attaching on S7-recognized {111} facets with the formation of the twinned planes (111) in aggregates (Figure 5.1i and Figure 5.2g). More interestingly, it is found that the NC synthesis in the presence of T7 and NaCl can produce 1-D nanostructures (Figure 5.8c-d), which is resulted from the increased T7 peptide-peptide interaction through NaCl. Therefore, similar to biomimeralization the environmental chemicals participate in the molecular interactions and materials synthesis, suggesting an alternative strategy for controlling the production of complex nanostructures in synthetic conditions.

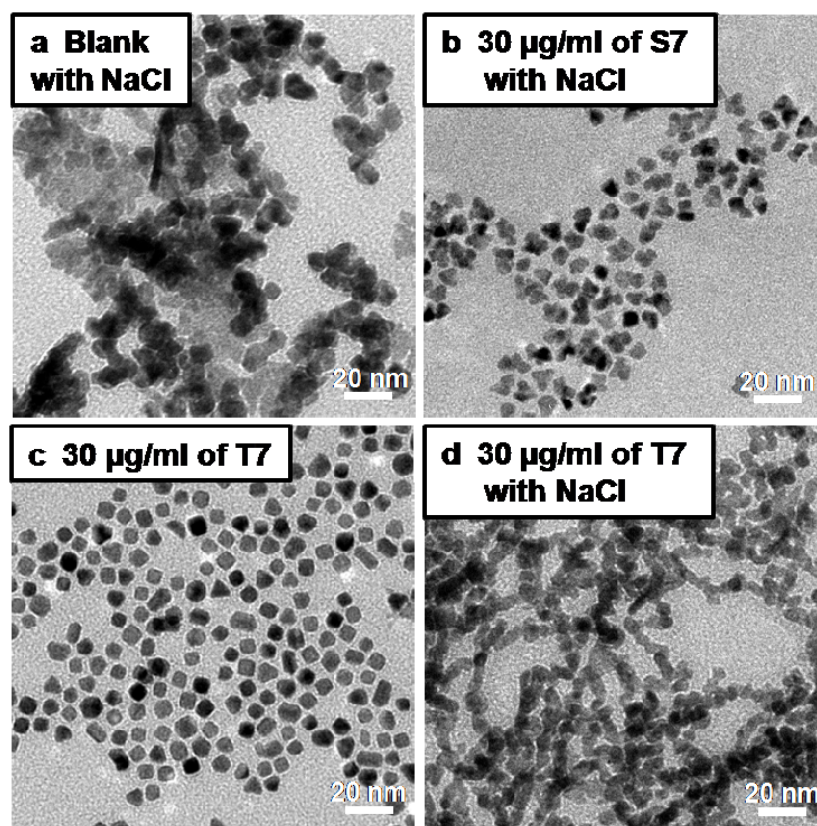


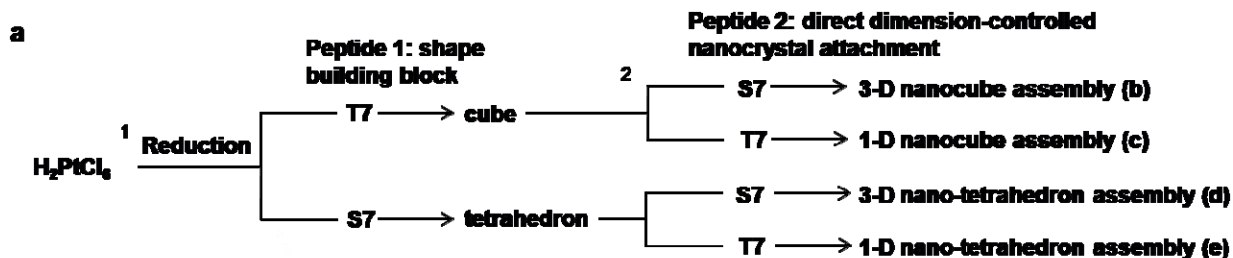
**Figure 5.8** Investigation of the effect of inorganic ions on the Pt NCs syntheses in the presence of peptides. All reactions share the same reduction conditions (0.8 mM NaBH<sub>4</sub>, 2 mM ascorbic acid and 1 mM H<sub>2</sub>PtCl<sub>6</sub>), except the peptide sequence (30 µg/ml) and externally added NaCl (24 mM): (a-d) TEM images of NCs obtained from the reactions in the presence of: (a) no peptide with NaCl, (b) S7 and NaCl, (c) T7 only and (d) T7 and NaCl. These concentrations are final concentration in the 5 ml solution.

### **One- and three- dimensional assembly of anisotropic nanoparticles**

We have shown a novel approach to control the crystal growth pathway and synthesize nanostructures through facet-specific peptides (Figure 5.4 and 5.5). Together with the discovery of the inorganic ion effect, we take the synthesis on step further by designing and producing nanostructures with control over their organization (1-D and 3-D) using nanocubes and nanotetrahedra as building blocks (Figure 5.9a). In a similar fashion, the peptides (T7 and S7) are

introduced into the reactions separately with a time interval of 10-30 seconds, while extra Pt (II) precursor ( $K_2PtCl_4$ ) is added together with the secondary peptide to increase crystal growth and generate larger nanostructures. We anticipate that the ions ( $Na^+$  and  $Cl^-$ ) released from the initial reduction can interact with the peptides introduced later, improving peptide-peptide interaction to achieve the assembly of NCs. Through introducing S7 and Pt (II) precursor into the T7 controlled reaction, 3-D nanostructures composed of multiple cubes can be achieved (Figure 5.9a-b). The zoom-in TEM image and its schematic model clearly show the structure organized with cubes sharing a common orientation (right panel of Figure 5.9b). If using the same shaping peptide T7 but switching the second peptide to T7, 1-D nanostructures dominated by edge-to-edge or corner-to-corner attached nanocubes are observed (Figure 5.9c). The right panels of Figure 5.9c show the TEM images and the corresponding schematic models of different orientations of the nanocube-chain. A truncated cube has twelve edges and eight corners, so the attachment of nanocubes on them should be 3-D preferential as S7 has achieved, indicating T7 exert important control (such as steric effect) on confining the attachment direction into 1-D. Replacing the shaping peptide to S7, 3-D and 1-D nanostructures composed of nano-tetrahedra can be produced by using S7 and T7 as the second peptide, respectively (Figure 5.9d and e). The zoom-in TEM image shown in Figure 5.9d indicates the tetrahedra are well-organized and assembled into a 3-D structure. A tetrahedron has six edge sides ( $\{100\}$  facet) while asymmetrical, suggesting that tetrahedra which prefer to attach on the edge sides may arrange along different directions as shown in Figure 5.9e. Nevertheless, the T7 peptide-peptide interaction predominantly drives the one-to-one nanoparticle attachment, achieving the production 1-D tetrahedron assembly. Overall, the faces of truncated cubes or tetrahedra are stabilized by the shaping peptide (the first peptide), so the particles favor attaching on the

relatively reactive surfaces (edges or corners), supported by the fact that face-to-face nanoparticle attachment is hardly observed (Figure 5.9). Nano-tetrahedra attach on corers ( $\{111\}$  facet) is seldom seen since the facets can be stabilized by S7 as well (Figure 5.9e). Obviously, T7 peptide and its interaction with ions play important roles in assisting the formation of the 1-D nanostructures. To confirm this, the controlled reactions including T7 concentration dependent experiments (Figure 5.10a-c), blank reaction (without peptide; Figure 5.10d) and one-step addition of T7 (Figure 5.10e) have been done. We concluded that reaching a critical concentration of T7 and introducing T7 after a period of reduction are indispensable to synthesize 1-D assemblies, suggesting that increasing T7 peptide-peptide interaction through concentration and ions effect can benefit 1-D nanostructure synthesis. Interestingly, decreasing the amount of  $K_2PtCl_4$  (from 250  $\mu$ l to 50  $\mu$ l) added in the second step to slow the crystal growth as well as the attachment process, micro-scale 1-D structure can be obtained, indicating the potential of our method to fabricate microstructures with well-organized building blocks (Figure 5.11a). The time-evolution images of the formation process for the 1-D nanostructure indicate the nanoparticles attach one by one and subsequently form a long chain (Figure 5.11b), proving the 1-D structures production is through particle attachment process instead of template synthesis. In particular, the complex structures shown in our studies exhibit characteristic outlines of their building blocks or interfaces among them, which usually are spontaneously eliminated by atom diffusion on surfaces and by recrystallization,<sup>92,105</sup> suggesting the specific binding effect of peptides on metal surfaces has modulated the surface energy and enabled the production of metastable nanostructures.



<sup>1</sup>Initiated by  $NaBH_4$ ; the released ions will interact with peptide 2.  
<sup>2</sup>After reacting for 10-30 seconds,  $K_2PtCl_6$  is introduced with peptide 2.

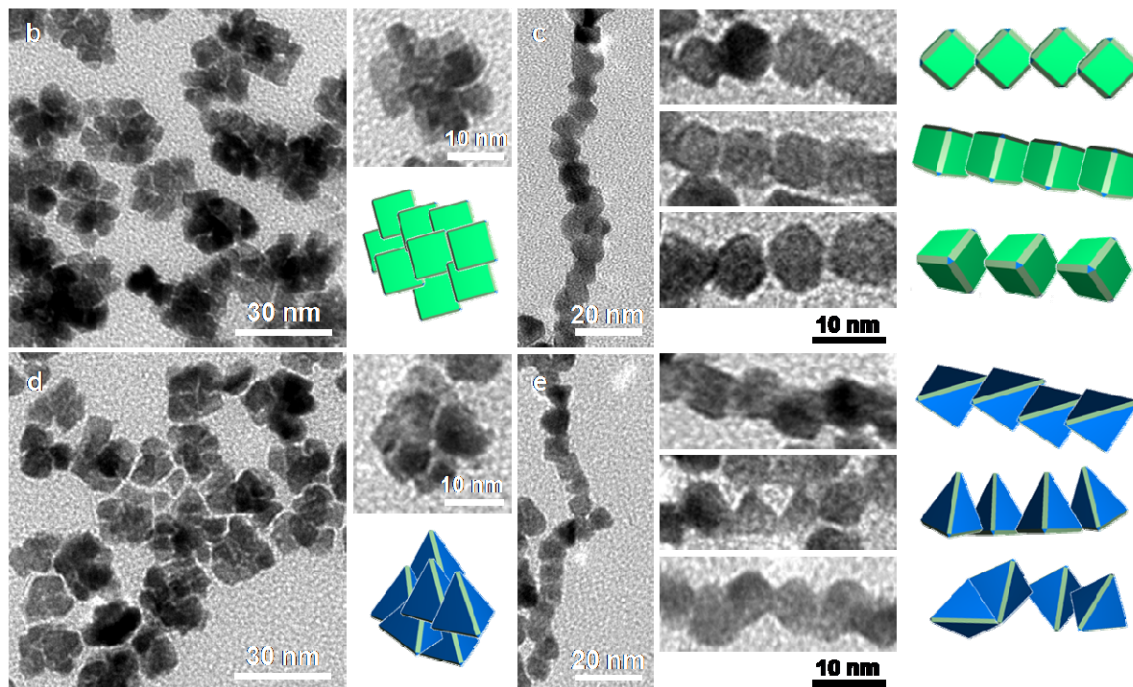


**Figure 5.9** Syntheses of 3-D and 1-D nanostructures through controlled molecular interaction and crystal growth. (a) Scheme depicting the strategy to build 3-D and 1-D nanostructures composed of anisotropic nanoparticles. First, the cubic and tetrahedral building blocks are controlled by the shaping peptide T7 and S7, respectively. Subsequently, the specific S7 and T7 peptide molecular interaction can direct 3-D and 1-D nanostructures, respectively. (b-e) showing TEM images and schematic models of the nanostructures obtained via the approaches described in (a): (b) 3-D nanocube assemblies, (c) 1-D nanocube assemblies, (d) 3-D nano-tetrahedron assemblies and (e) 1-D nano-tetrahedron assemblies.

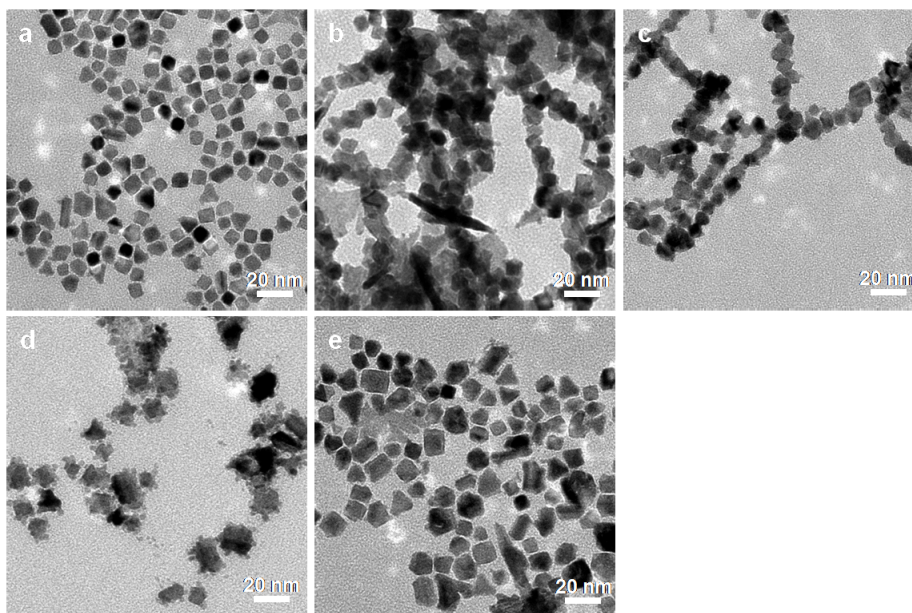


**Figure 5.10** TEM images of Pt NCs from control experiments. (a-c) The effect of the concentration of T7 peptides on 1-D nanocrystal assembly. 1 mM  $\text{H}_2\text{PtCl}_6$  and 2 mM ascorbic acid were pre-mixed with water in a vial, and 0.8 mM  $\text{NaBH}_4$  was injected in one shot; the final volume is 5 ml. After 10 seconds of reaction, different amount of T7: (a) 100  $\mu\text{l}$ , (b) 200  $\mu\text{l}$  and (c) 300  $\mu\text{l}$  was introduced together with  $\text{K}_2\text{PtCl}_4$ , respectively. (d) Blank control; Pt NCs obtained from the reaction using the same conditions as the assembly synthesis except in the absence of peptides. (e) Pt NCs obtained from the reaction similar to c, except T7 was added before the reduction, i.e., before the  $\text{Na}^+ \text{Cl}^-$  ions are released from the reactants.

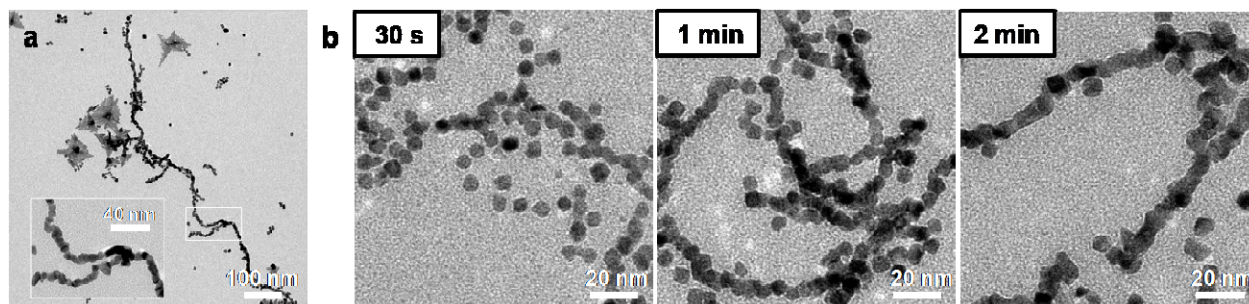


**Figure 5.11** (a) TEM image of micro-scale structure via 1-D NCs assembly. (b) TEM images of the evolution process of the structures with reaction time. The 1-D structures were assembled

from NC monomers controlled by T7 peptides. 1 mM  $\text{H}_2\text{PtCl}_6$ , 3  $\mu\text{g/ml}$  T7 and 2 mM ascorbic acid were pre-mixed with water in a vial, and 0.8 mM  $\text{NaBH}_4$  was injected in one shot. After 30 seconds of reaction, 250  $\mu\text{l}$  of T7 and 50  $\mu\text{l}$  of  $\text{K}_2\text{PtCl}_4$  (10 mM aqueous solution) were added; total reaction time is 1 hour.

In summary, it was shown that Pt face-specific peptides can direct the syntheses of anisotropic nanoparticles into 1-D and 3-D nanostructures through particle attachment. Specifically, a larger number of S7 in reaction promotes the production of high energy nanoparticles, driving coalescence. Combining with Pt {100} facet-specific peptide (T7), the syntheses of cubic and tetrahedral nanoparticles into 3-D nanostructures through oriented attachment along [110] directions have been demonstrated, respectively. We believe that these results are a consequence of the specific recognition properties of the peptides on metal surfaces and, hence, the presence of {110} reactive facets, which promote particles attach on them. Sequential introduction of S7 and T7 into reactions has been proposed an effective strategy to simultaneously express the binding effect of the two peptides on crystal surfaces, influencing the crystal growth mechanism. The specific peptide-peptide interaction also contributes to the crystal growth dominated by particle attachment. Through the interplay among T7, inorganic ions and metal surface, 1-D nanostructures composed of anisotropic nanoparticles have been produced, in which the building blocks are shaped as cube or tetrahedron depending on the shaping peptide. We strategically exploit the interfacial biomolecular recognition to construct organized nanostructures in synthetic conditions through nanoparticle attachment without supramolecular pre-organization.



## CONCLUSION

My initial studies on biomimetic synthesis have achieved the synthesis of Pd NCs with size control. I continued my study on demonstrating a rational biomimetic approach to select Pt {100} and {111} facet-specific peptides and their ability in binding the particular crystal surface and thus shaping NCs with predictable morphologies. This study demonstrates unambiguously the abilities of the facet selective binding peptides in determining the nanocrystal shapes, presenting a critical step forward in exploiting biomolecules for synthesis of nanostructures. We continued to study the fundamentals behind the synthesis, which led to the investigation of selective adsorption of small molecules, i.e., aromatic molecules, on noble metal surfaces. Starting from Pt, it was shown that the negative electrostatic potential on the aromatic ring is the prerequisite to display binding selectivity to Pt {111}, while positive to neutral one can lead to Pt {100}. The geometric matching between molecular binding sites and surface lattices plays a part as well in facet selectivity. Raman spectroscopy was used to probe the interaction between aromatic molecules and metal surfaces, providing direct evidence of their binding mechanisms. These discoveries are further exploited to design and identify Pd {111} and Pd {100} facet-specific surfactants. At last, we reported the three-dimensional oriented attachment of cubic or tetrahedral nanoparticles controlled by the shaping peptide. This is contributed from the cooperative effect of the Pt {111} and {100} facet-specific peptides, which alters the crystal growth pathway to prefer particle coalescence, and drives the particle attach on the {110} reactive facets. Furthermore, we demonstrated the synthesis of one-dimensional assembly of nanocubes and nano-tetrahedra, respectively, through the inorganic ions modified peptide-peptide interaction. These results represent a significant step forward to the development of complex structures with designed hierarchy through exploring the full potential of biomolecules.

## REFERENCES

- [1] Xia, Y., Xiong, Y. J., Lim, B., and Skrabalak, S. E., Shape-Controlled Synthesis of Metal Nanocrystals: Simple Chemistry Meets Complex Physics? *Angew. Chem. Int. Edit.* **48**, 60 (2009).
- [2] Alivisatos, A. P., Perspectives on the Physical Chemistry of Semiconductor Nanocrystals. *J. Phys. Chem.* **100**, 13226 (1996).
- [3] Bruchez, Marcel et al., Semiconductor Nanocrystals as Fluorescent Biological Labels. *Science* **281**, 2013 (1998).
- [4] El-Sayed, Mostafa A., Some Interesting Properties of Metals Confined in Time and Nanometer Space of Different Shapes. *Accounts Chem. Res.* **34**, 257 (2001).
- [5] Xia, Y. et al., One-Dimensional Nanostructures: Synthesis, Characterization, and Applications. *Adv. Mater.* **15**, 353 (2003).
- [6] Avouris, Phaedon, Chen, Zhihong, and Perebeinos, Vasili, Carbon-based electronics. *Nature Nanotech.* **2**, 605 (2007).
- [7] Hao, Rui et al., Synthesis, Functionalization, and Biomedical Applications of Multifunctional Magnetic Nanoparticles. *Adv. Mater.* **22**, 2729. (2010)
- [8] Tao, Andrea R., Habas, Susan, and Yang, Peidong, Shape Control of Colloidal Metal Nanocrystals. *Small* **4**, 310 (2008).
- [9] Klimov, V. I. et al., Optical Gain and Stimulated Emission in Nanocrystal Quantum Dots. *Science* **290**, 314 (2000).
- [10] Jin, Rongchao et al., Photoinduced Conversion of Silver Nanospheres to Nanoprisms. *Science* **294**, 1901 (2001).
- [11] Huang, Xiaoqing et al., Controlled Formation of Concave Tetrahedral/Trigonal Bipyramidal Palladium Nanocrystals. *J. Am. Chem. Soc.* **131**, 13916 (2009).

- [12] Kan, Shihai et al., Synthesis and Size-Dependent Properties of Zinc-Blende Semiconductor quantum rods. *Nature Mater.* **2**, 155 (2003).
- [13] Katherine A. Willets and Richard P. Van Duyne, Localized Surface Plasmon Resonance Spectroscopy and Sensing. *Annu. Rev. Phys. Chem.* **58**, 267 (2007).
- [14] Chen, Jingyi, Lim, Byungkwon, Lee, Eric P., and Xia, Younan, Shape-Controlled Synthesis of Platinum Nanocrystals for Catalytic and Electrocatalytic Applications. *Nano Today* **4**, 81 (2009).
- [15] Wang, Jia X. et al., Oxygen Reduction on Well-Defined Core-Shell Nanocatalysts: Particle Size, Facet, and Pt Shell Thickness Effects. *J. Am. Chem. Soc.* **131**, 17298 (2009).
- [16] Bratlie, Kaitlin M. et al., Platinum Nanoparticle Shape Effects on Benzene Hydrogenation Selectivity. *Nano Lett.* **7**, 3097 (2007).
- [17] Peng, Zhenmeng and Yang, Hong, Designer Platinum Nanoparticles: Control of Shape, Composition in Alloy, Nanostructure and Electrocatalytic property. *Nano Today* **4**, 143 (2009).
- [18] Tian, Na et al., Synthesis of Tetrahedral Platinum Nanocrystals with High-Index Facets and High Electro-Oxidation Activity. *Science* **316**, 732 (2007).
- [19] Wang, Xun, Zhuang, Jing, Peng, Qing and Li, Yadong, A General Strategy for Nanocrystal Synthesis. *Nature* **437**, 121 (2005).
- [20] Xia, Younan, Rogers, John A., Paul, Kateri E., and Whitesides, George M., Unconventional Methods for Fabricating and Patterning Nanostructures. *Chem. Rev.* **99**, 1823 (1999).
- [21] Yin, Yadong and Alivisatos, A. Paul, Colloidal Nanocrystal Synthesis and the Organic-Inorganic Interface. *Nature* **437**, 664 (2005).
- [22] Punter, Victor F., Krishnan, Kannan M., and Alivisatos, A. Paul, Colloidal Nanocrystal Shape and Size Control: the Case of Cobalt. *Science* **291**, 2115 (2001).

- [23] Manna, Liberato, Scher, Erik C., and Alivisatos, A. Paul, Synthesis of Soluble and Processable Rod-, Arrow-, Teardrop-, and Tetrapod-Shaped CdSe Nanocrystals. *J. Am. Chem. Soc.* **122**, 12700 (2000).
- [24] Brutchey, Richard L. and Morse, Daniel E., Silicatein and the Translation of its Molecular Mechanism of Biosilicification into Low Temperature Nanomaterial Synthesis. *Chem. Rev.* **108**, 4915 (2008).
- [25] Banfield, Jillian F. et al., Aggregation-Based Crystal Growth and Microstructure Development in Natural Iron Oxyhydroxide Biomineralization Products. *Science* **289**, 751 (2000).
- [26] Mann, Stephen, Molecular Tectonics in Biomineralization and Biomimetic Materials Chemistry. *Nature* **365**, 499 (1993).
- [27] Belcher, A. M. et al., Control of Crystal Phase Switching and Orientation by Soluble Mollusc-Shell Proteins. *Nature* **381**, 56 (1996).
- [28] Faivre, Damien and Schüler, Dirk, Magnetotactic Bacteria and Magnetosomes. *Chem. Rev.* **108**, 4875 (2008).
- [29] Amemiya, Yosuke et al., Controlled Formation of Magnetite Crystal by Partial Oxidation of Ferrous Hydroxide in the Presence of Recombinant Magnetotactic Bacterial Protein Mms6. *Biomaterials* **28**, 5381 (2007).
- [30] Cha, Jennifer N. et al., Silicatein Filaments and Subunits from a Marine Sponge Direct the Polymerization of Silica and Silicones in Vitro. *Proc. Natl. Acad. Sci.* **96**, 361 (1999).
- [31] Xie, Jianping, Lee, Jim Yang, Wang, Daniel I. C, and Ting, Yen Peng, Identification of Active Biomolecules in the High-Yield Synthesis of Single-Crystalline Gold Nanoplates in Algal Solutions. *Small* **3**, 672 (2007).

- [32] Naik, Rajesh R. et al., Biomimetic Synthesis and Patterning of Silver Nanoparticles. *Nature Mater.* **1**, 169 (2002).
- [33] Dickerson, Matthew B., Sandhage, Kenneth H., and Naik, Rajesh R., Protein- and Peptide-Directed Syntheses of Inorganic Materials. *Chem. Rev.* **108**, 4935 (2008).
- [34] Whaley, Sandra R. et al., Selection of Peptides with Semiconductor Binding Specificity for Directed Nanocrystal Assembly. *Nature* **405**, 665 (2000).
- [35] Sarikaya, M. et al., Molecular Biomimetics: Nanotechnology through Biology. *Nature Mater.* **2**, 577 (2003).
- [36] Miyaura, Norio and Suzuki, Akira, Palladium-Catalyzed Cross-Coupling Reactions of Organoboron Compounds. *Chem. Rev.* **95**, 2457 (1995).
- [37] Turkevich, John and Kim, Gwan, Palladium: Preparation and Catalytic Properties of Particles of Uniform Size. *Science* **169**, 873 (1970).
- [38] Li, Yin, Boone, Edna, and El-Sayed, Mostafa A., Size Effects of PVP-Pd Nanoparticles on the Catalytic Suzuki Reactions in Aqueous Solution. *Langmuir* **18**, 4921 (2002).
- [39] Nemamcha, Abderrafik, Rehspringer, Jean-Luc, and Khatmi, Djameledine, Synthesis of Palladium Nanoparticles by Sonochemical Reduction of Palladium(II) Nitrate in Aqueous Solution. *J. Phys. Chem. B* **110**, 383 (2005).
- [40] Chiu, Chin-Yi, Li, Yujing, and Huang, Yu, Size-Controlled Synthesis of Pd Nanocrystals Using a Specific Multifunctional Peptide. *Nanoscale* **2**, 927 (2010).
- [41] Si, Satyabrata and Mandal, Tarun K, Tryptophan-Based Peptides to Synthesize Gold and Silver Nanoparticles: A Mechanistic and Kinetic Study. *Chem. - Eur. J.* **13**, 3160 (2007).
- [42] Li, Yujing, Whyburn, Gordon P., and Huang, Yu, Specific Peptide Regulated Synthesis of Ultrasmall Platinum Nanocrystals. *J. Am. Chem. Soc.* **131**, 15998 (2009).

- [43] Li, Yujing and Huang, Yu, Morphology-Controlled Synthesis of Platinum Nanocrystals with Specific Peptides. *Adv. Mater.* **22**, 1921 (2010).
- [44] Chiu, Chin-Yi et al., Platinum Nanocrystals Selectively Shaped Using Facet-Specific Peptide Sequences. *Nature Chem.* **3**, 393 (2011).
- [45] Teng, X.W. and Yang, H. Synthesis of Platinum Multipods: an Induced Anisotropic Growth. *Nano Lett.* **5**, 885 (2005).
- [46] Song, H., Kim, F., Connor, S., Somorjai, G.A. and Yang, P. Pt Nanocrystals: Shape Control and Langmuir - Blodgett Monolayer Formation. *J. Phys. Chem. B* **109**, 188 (2004).
- [47] Ahmadi, T.S., Wang, Z.L., Green, T.C., Henglein, A. and El-Sayed, M.A. Shape-Controlled Synthesis of Colloidal Platinum Nanoparticles. *Science* **272**, 1924 (1996).
- [48] Wang, Z.L., Petroski, J.M., Green, T.C. and El-Sayed, M.A. Shape Transformation and Surface Melting of Cubic and Tetrahedral Platinum Nanocrystals. *J. Phys. Chem. B* **102**, 6145 (1998).
- [49] So, C.R. et al. Molecular Recognition and Supramolecular Self-Assembly of a Genetically Engineered Gold Binding Peptide on Au{111}. *ACS Nano* **3**, 1525(2009).
- [50] Ruan, Lingyan et al., Tailoring Molecular Specificity Toward a Crystal Facet: a Lesson From Biorecognition Toward Pt{111}. *Nano Lett.* **13**, 840 (2013).
- [51] Morin, C., Simon, D., and Sautet, P., Density-Functional Study of the Adsorption and Vibration Spectra of Benzene Molecules on Pt(111). *J. Phys. Chem. B* **107**, 2995 (2003).
- [52] Saeys, Mark, Reyniers, Marie-Francoise, Marin, Guy B., and Neurock, Matthew, Density Functional Study of Benzene Adsorption on Pt(111). *J. Phys. Chem. B* **106**, 7489 (2002).
- [53] Morin, C., Simon, D., and Sautet, P., Chemisorption of Benzene on Pt(111), Pd(111), and Rh(111) Metal Surfaces: A Structural and Vibrational Comparison from First Principles. *J.*

*Phys.Chem.B* **108**, 5653 (2004).

[54] Anderson, Alfred B., McDevitt, Michael R., and Urbach, F. L., Structure and Electronic Factors in Benzene Coordination to Cr(CO)<sub>3</sub> and to Cluster Models of Ni, Pt, and Ag (111) Surfaces. *Surf. Sci.* **146** (1), 80 (1984).

[55] Mecozzi, S., West, A. P., and Dougherty, D. A., Cation-Pi Interactions in Aromatics of Biological and Medicinal Interest: Electrostatic Potential Surfaces as a Useful Qualitative Guide. *Proc. Natl. Acad. Sci.* **93**, 10566 (1996).

[56] Politzer, Peter, Abrahmsen, Lars, and Sjoberg, Per, Effects of Amino and Nitro Substituents upon the Electrostatic Potential of an Aromatic Ring. *J. Am. Chem. Soc.* **106** (4), 855 (1984).

[57] Chiu, Chin-Yi et al., The Facet-Selective Adsorption on Noble Metal Crystals Guided by Electrostatic Potential Surfaces of Aromatic Molecules, *J. Am. Chem. Soc.*, 2013, in revision.

[58] Spartan '06, Wavefunction Inc. Irvine, CA

[59] Kresse, G. and Hafner, J., Ab Initio Molecular Dynamics for Liquid Metals. *Phys. Rev. B* **47**, 558 (1993).

[60] Perdew, John P., Burke, Kieron, and Ernzerhof, Matthias, Generalized Gradient Approximation Made Simple. *Phys. Rev. Lett.* **77**, 3865 (1996).

[61] Monkhorst, Hendrik J. and Pack, James D., Special points for Brillouin-zone integrations. *Phys. Rev. B* **13**, 5188 (1976).

[62] Koel, B. E., Crowell, J. E., Mate, C. M., and Somorjai, G. A., A High-Resolution Electron Energy Loss Spectroscopy Study of the Surface Structure of Benzene Adsorbed on the Rhodium(111) Crystal Face. *J. Phys. Chem.* **88**, 1988 (1984).

- [63] Queiroz, Auriekson N., Gomes, Bruno A. Q., Moraes Jr, Waldir M., and Borges, Rosivaldo S., A Theoretical Antioxidant Pharmacophore for Resveratrol. *Eur. J. Med. Chem.* **44**, 1644 (2009).
- [64] Derry, G. N. and Ji-Zhong, Zhang, Work Function of Pt(111). *Phys. Rev. B* **39**, 1940 (1989).
- [65] Nieuwenhuys, B. E. and Sachtler, W. M. H., Crystal Face Specificity of Nitrogen Adsorption on a Platinum Field Emission Tip. *Surf. Sci.* **34**, 317 (1973).
- [66] Lin, Daohui and Xing, Baoshan, Adsorption of Phenolic Compounds by Carbon Nanotubes: Role of Aromaticity and Substitution of Hydroxyl Groups. *Environ. Sci. Tech.* **42**, 7254 (2008).
- [67] Brown, H.C. et al., in Braude, E.A. and F.C. Nachod *Determination of Organic Structures by Physical Methods*, Academic Press, New York (1955)
- [68] Anderson, N. J., Bolto, B. A., Eldridge, R. J., and Jackson, M. B., Polyampholytes for Water Treatment with Magnetic Particles. *React. Polym.* **19**, 87 (1993).
- [69] Wang, Shu Fang, Chen, Xing Guo, Hu, Zhi De, and Ju, Yong, Analysis of Three Effective Components in Fructus corni and its Preparations by Micellar Electrokinetic Capillary Chromatography. *Biomed. Chromatogr.* **17**, 306 (2003).
- [70] Ragnar, Martin, Lindgren, Christofer T., and Nilvebrant, Nils-Olof, pKa-Values of Guaiacyl and Syringyl Phenols Related to Lignin. *J. Wood Chem. Technol.* **20**, 277 (2000)
- [71] Myers, A. K. and Benziger, Jay B., Effect of Substituent Groups on the Interaction of Benzene with Nickel(111). *Langmuir* **5**, 1270 (1989).
- [72] Soriaga, Manuel P. and Hubbard, Arthur T., Determination of the Orientation of Adsorbed Molecules at Solid-Liquid Interfaces by Thin-Layer Electrochemistry: Aromatic Compounds at Platinum Electrodes. *J Am. Chem. Soc.* **104**, 2735 (1982).



- [73] Lien, Eric J., Ren, Shijun, Bui, Huynh-Hoa, and Wang, Rubin, Quantitative Structure-Activity Relationship Analysis of Phenolic Antioxidants. *Free Radic.l Biol. Med.* **26**, 285 (1999).
- [74] Guibal, Eric et al., Oxidation of Hydroquinone to p-Benzoquinone Catalyzed by Cu(II) Supported on Chitosan Flakes. *J. Appl. Polym. Sci.* **100**, 3034 (2006).
- [75] Stern, Donald A. et al., Studies of L-DOPA and Related Compounds Adsorbed from Aqueous Solutions at Platinum(100) and Platinum(111): Electron Energy-Loss Spectroscopy, Auger Spectroscopy, and Electrochemistry. *Langmuir* **4**, 711 (1988).
- [76] Kubinyi, M., Billes, F., Grofcsik, A., and Keresztury, G., Vibrational Spectra and Normal Coordinate Analysis of Phenol and Hydroquinone. *J. Mol. Struc.* **266**, 339 (1992).
- [77] Gao, Ping and Weaver, Michael J., Surface-Enhanced Raman Spectroscopy as a Probe of Adsorbate-Surface Bonding: Benzene and Monosubstituted Benzenes Adsorbed at Gold Electrodes. *J. Phys. Chem.* **89**, 5040 (1985).
- [78] Liu, Guo-Kun et al., Effect of Intrinsic Properties of Metals on the Adsorption Behavior of Molecules: Benzene Adsorption on Pt Group Metals. *J. Phys. Chem. B* **110**, 17498 (2006).
- [79] Borodko, Yuri et al., Probing the Interaction of Poly(vinylpyrrolidone) with Platinum Nanocrystals by UV-Raman and FTIR. *J. Phys. Chem. B* **110**, 23052 (2006).
- [80] Sun, Q., Tripathi, G. N. R., and Schuler, R. H., Time-Resolved Resonance Raman Spectroscopy of p-Aminophenol Radical Cation in Aqueous Solution. *J. Phys. Chem.* **94**, 6273 (1990).
- [81] Tanaka, Takeyuki et al., Surface-Enhanced Raman Scattering of Pyridine and p-Nitrophenol Studied by Density Functional Theory Calculations. *Vib. Spectrosc.* **34**, 157 (2004).
- [82] Cohen, Sidney and Cohen, Saul G., Preparation and Reactions of Derivatives of Squaric Acid. Alkoxy-, Hydroxy-, and Aminocyclobutenediones1. *J. Am. Chem. Soc.* **88**, 1533 (1966).

- [83] Habas, Susan E. et al., Shaping Binary Metal Nanocrystals through Epitaxial Seeded Growth. *Nature Mater.* **6**, 692 (2007).
- [84] Steenken, S. and Neta, P., Electron Transfer Rates and Equilibriums between Substituted Phenoxide Ions and Phenoxy Radicals. *J. Phys. Chem.* **83**, 1134 (1979).
- [85] Michaelson, Herbert B., The Work Function of the Elements and its Periodicity. *J. Appl Phys.* **48**, 4729 (1977).
- [86] Methfessel, M., Hennig, D., and Scheffler, M., Trends of the Surface Relaxations, Surface Energies, and Work Functions of the 4d Transition Metals. *Phys. Rev. B* **46**, 4816 (1992).
- [87] Ruan, Lingyan, Chiu, Chin-Yi, Li, Yujing, and Huang, Yu, Synthesis of Platinum Single-Twinned Right Bipyramid and {111}-Bipyramid through Targeted Control over Both Nucleation and Growth Using Specific Peptides. *Nano Lett.* **11**, 3040 (2011).
- [88] Shevchenko, Elena V., Talapin, Dmitri V., Kotov, Nicholas A., O'Brien, Stephen and Murray, Christopher B. Structural Diversity in Binary Nanoparticle Superlattices. *Nature* **439**, 55 (2006).
- [89] Miszta, Karol et al., Hierarchical Self-Assembly of Suspended Branched Colloidal Nanocrystals into Superlattice Structures. *Nature Mater.* **10**, 872 (2011).
- [91] Glotzer, Sharon C. and Solomon, Michael J., Anisotropy of Building Blocks and their Assembly into Complex Structures. *Nature Mater.* **6**, 557 (2007).
- [92] Li, Dongsheng et al., Direction-Specific Interactions Control Crystal Growth by Oriented Attachment. *Science* **336**, 1014 (2012).
- [93] Liao, Hong-Gang, Cui, Likun, Whitlam, Stephen, and Zheng, Haimei, Real-Time Imaging of Pt<sub>3</sub>Fe Nanorod Growth in Solution. *Science* **336**, 1011 (2012).

- [94] Zheng, Haimei et al., Observation of Single Colloidal Platinum Nanocrystal Growth Trajectories. *Science* **324**, 1309 (2009).
- [95] Ribeiro, Caue, Lee, Eduardo J. H., Longo, Elson, and Leite, Edson R., A Kinetic Model to Describe Nanocrystal Growth by the Oriented Attachment Mechanism. *ChemPhysChem* **6**, 690 (2005).
- [96] LaMer, Victor K. and Dinegar, Robert H., Theory, Production and Mechanism of Formation of Monodispersed Hydrosols. *J. Am. Chem. Soc.* **72**, 4847 (1950).
- [97] Tang, Y. and Ouyang, M. Tailoring Properties and Functionalities of Metal Nanoparticles through Crystallinity Engineering. *Nature Mater.* **6**, 754 (2007).
- [98] Aravinda, Subrayashastry et al., Aromatic-Aromatic Interactions in Crystal Structures of Helical Peptide Scaffolds Containing Projecting Phenylalanine Residues. *J. Am. Chem. Soc.* **125**, 5308 (2003).
- [99] Zhang, S. Fabrication of Novel Biomaterials through Molecular Self-Assembly. *Nature Biotech.* **21**, 1171 (2003).
- [100] Schliehe, Constanze et al., Ultrathin PbS Sheets by Two-Dimensional Oriented Attachment. *Science* **329**, 550 (2010).
- [101] Zhu, Cun et al., Facile Synthesis of Gold Wavy Nanowires and Investigation of Their Growth Mechanism. *J. Am. Chem. Soc.* **134**, 20234. (2012).
- [102] Hagn, F. et al., A Conserved Spider Silk Domain Acts as a Molecular Switch that Controls Fibre Assembly *Nature* **465**, 239-242 (2010).
- [103] Jelesarov, Ilian, Dürr, Eberhard, Thomas, Richard M., and Bosshard, Hans Rudolf, Salt Effects on Hydrophobic Interaction and Charge Screening in the Folding of a Negatively Charged Peptide to a Coiled Coil (Leucine Zipper). *Biochemistry* **37**, 7539 (1998).

[104] Arakawa, Tsutomu and Timasheff, Serge N., Mechanism of Protein Salting in and Salting out by Divalent Cation Salts: Balance between Hydration and Salt Binding. *Biochemistry* **23**, 5912 (1984).

[105] Penn, R. Lee and Banfield, Jillian F., Imperfect Oriented Attachment: Dislocation Generation in Defect-Free Nanocrystals. *Science* **281**, 969 (1998).